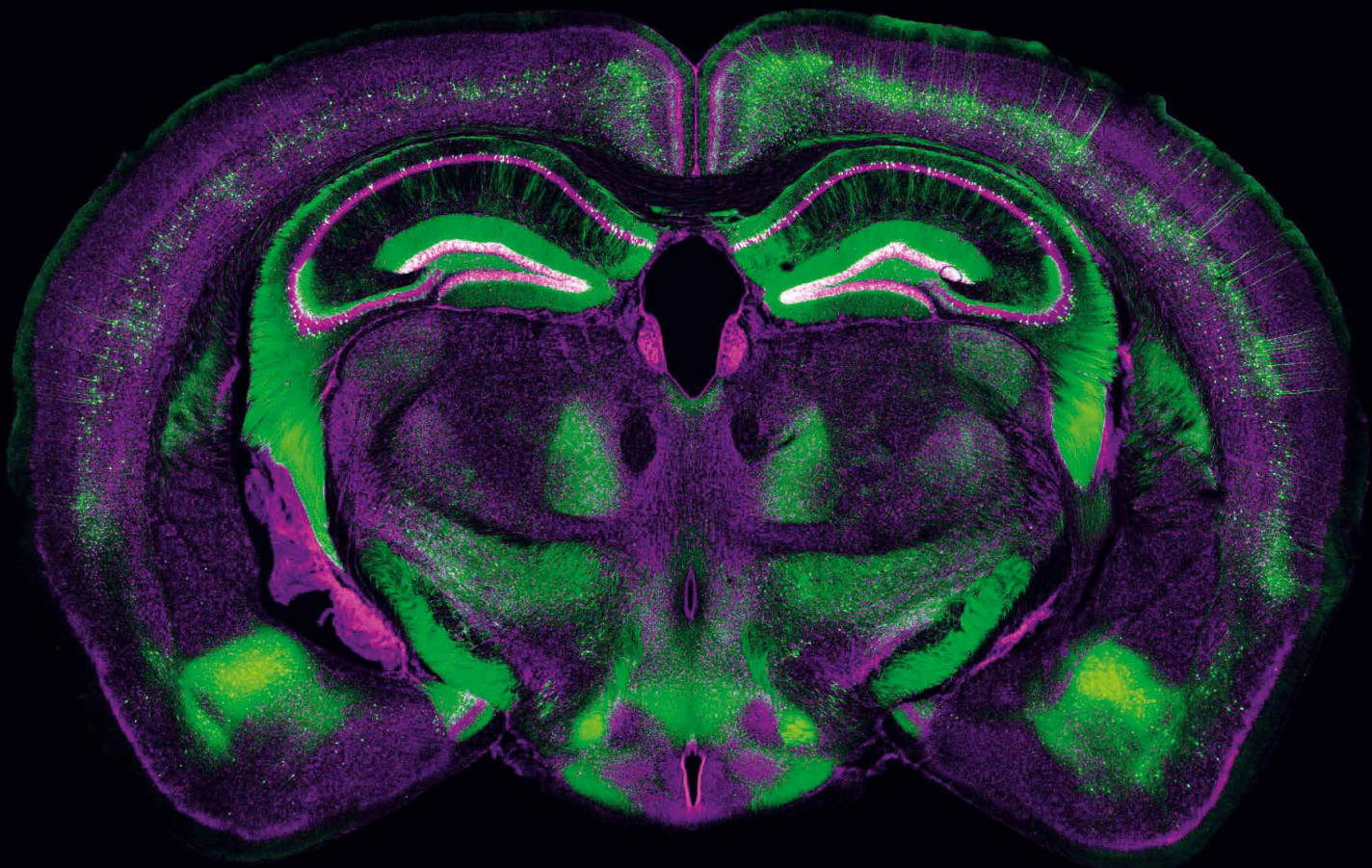


Microscopy Techniques for NEUROSCIENCE



Seeing beyond

WILEY

Imprint

© Wiley-VCH Verlag GmbH
& Co. KGaA
Boschstr. 12, 69469 Weinheim,
Germany
Email: info@wiley-vch.de

Carl Zeiss Microscopy GmbH
Carl-Zeiss-Promenade 10,
07745 Jena,
Germany
www.zeiss.com/microscopy

Editor-in-Chief:
Dr. Christina Poggel

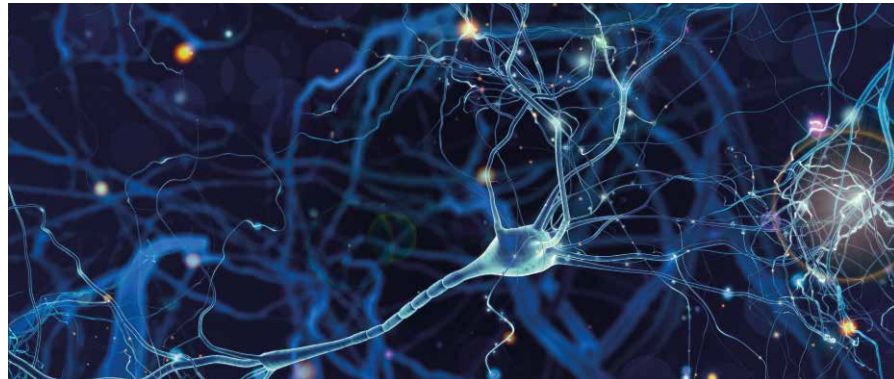
Editor:
Dr. Martin Friedrich

Ad Sales:
Dr. Stefanie Krauth

Printer:
AC medienhaus GmbH,
Wiesbaden, Germany

Editorial

©whitehoune/Shutterstock



What makes us human? How do our brains enable us to recognize faces – not least our own – and identify smells, sounds or places? How does it let us store that information for years, even decades, and then recall it in milliseconds? The goal of modern neuroscience is to enlighten such processes, often using research in animal models to gain a better understanding of brain function.

Work by scientists such as Schwann, Schleiden, Golgi and Ramón y Cajal gave us our first basic understanding of neurons and neural circuits. These researchers also challenged microscope manufacturers such as Carl Zeiss to strive for continual innovation. And that is true to this day: the ever-growing field of neuroscience constantly calls on us to develop new microscopy techniques to help you answer crucial scientific questions.

This booklet aims to give you an overview of recent achievements in the field of neuroscience. A brief introduction details some advanced microscopy techniques from ZEISS and their specific benefits for your research. This is followed by a selection of peer-reviewed articles from various WILEY journals, condensed into a digestible format with links to the original article DOIs.

In a concluding interview, Professor Thomas Misgeld from the Munich Center for Neurosciences shares his views on current challenges and future developments in microscopy applications for neuroscience.

Enjoy reading – and we are looking forward to your feedback.

Jan Birkenbeil Eric Hummel Bernhard Zimmermann

Business Sector Life Sciences
Carl Zeiss Microscopy GmbH
Carl-Zeiss-Promenade 10, 07745 Jena, Germany
Contact us at: microscopy@zeiss.com

Contents

- 3** Editorial
- 5** Introduction
- 8** In vivo Ca²⁺ imaging of astrocytic microdomains reveals a critical role of the amyloid precursor protein for mitochondria
Montagna E, Crux S, Luckner M, et al.
- 12** Blood–brain barrier disruption and angiogenesis in a rat model for neurocysticercosis
Carmen-Orozco R P, Dávila-Villacorta D G, Cauna Y, et al.
- 16** Cone synapses in mammalian retinal rod bipolar cells
Pang J-J, Yang Z, Jacoby RA, Wu SM
- 20** Regional differences in Purkinje cell morphology in the cerebellar vermis of male mice
Nedelescu H, Abdelhack M, Pritchard AT
- 25** Characterization of perinatally born glutamatergic neurons of the mouse olfactory bulb based on NeuroD6 expression reveals their resistance to sensory deprivation
Angelova A, Platel J-C, Béclin C, et al.
- 30** Quantification of collagen fiber structure using second harmonic generation imaging and two-dimensional discrete Fourier transform analysis: Application to the human optic nerve head
Pijanka JK, Markov PP, Midgett D, et al.
- 34** Lipopolysaccharide-induced alteration of mitochondrial morphology induces a metabolic shift in microglia modulating the inflammatory response in vitro and in vivo
Nair S, Sobotka K S, Joshi P, et al.
- 39** Pbx loss in cranial neural crest, unlike in epithelium, results in cleft palate only and a broader midface
Welsh IC, Hart J, Brown JM, et al.
- 44** Interview:
Neuroscience Research Needs Networking

Introduction

“As long as our brain is a mystery, the universe, the reflection of the structure of the brain will also be a mystery.”

In his famous quote, Nobel Laureate Santiago Ramón y Cajal captures both the fascination that neuroscience evokes and the challenges neuroscientists have been facing for more than a century.

So what do we actually know about the human brain?

Present day research suggests that the brain consists of about 86 billion neurons—at least 30 times more than the base pairs in our genome—with 125 trillion synapses in the brain cortices alone, and that’s at least a thousand times more synapses than there are thought to be stars in our galaxy. The brain is by far the most complex organ in the human body and one of the most complex machines we have ever known, typically consuming somewhere around 70% of the total energy a body generates. Over 7,000,000,000 of these machines, or we might call them human computers, are currently populating this planet.

Still, we remain largely ignorant of how the brain coordinates all of its activities and develops language, thought and self-consciousness, to name just a few examples, thus demonstrating that we are still far from a truly holistic understanding of the brain’s inner workings. A multidisciplinary approach is essential if we wish to prove a connection between behavioral or even personal traits and the molecular workings at cell and circuit level.

Since the days of Ramón y Cajal and his fellow laureate Camillo Golgi, microscopy has proven to be an extremely powerful approach to tackling the challenges that are imposed on us by the sheer complexity of the brain. Starting with the first light microscopy-based studies in the 19th century, neuroscience has helped push a tremendous evolution of imaging tech-

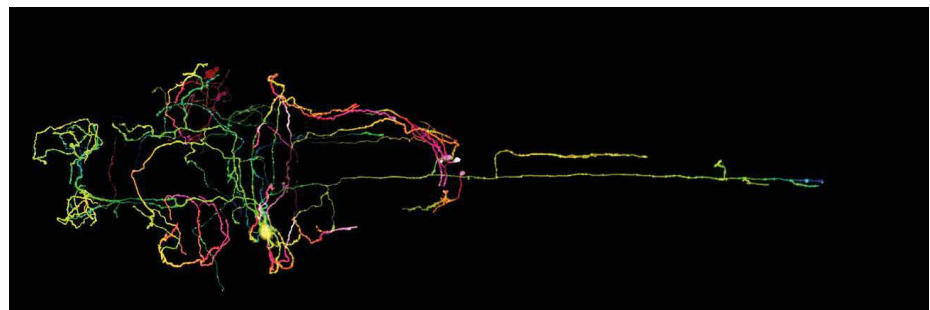


Figure 1.: A single neuron labeled with mCherry in a 4 dpf Zebrafish. Acquired with ZEISS LSM 880. Courtesy of T. Xiao and B. Carroll, Isacoff Labs, University of California, Berkeley, USA.

nologies that today range from non-invasive large-scale methods such as MRI and CT to tissue- and cell-based methods such as electron, X-ray and highly sophisticated light microscopy technologies. Microscopy systems with cutting-edge digital technology enable the structural investigation of 3D volumes as well as live-cell imaging at unprecedented resolution and speed.

The Challenge for Microscopy

Since the human brain is a large organ but its organization makes use of very tiny connections, one of the biggest challenges we face in microscopy for neuroscience is scale. Additionally, it is not always possible to extract structural and functional information at the same time, which means that often there is no “ideal” imaging system. Thus, complementary microscopy techniques frequently need to be combined with and supported by methods from, for example, cell biology or biochemistry.

Microscopy in Neuroscience

From Ernst Abbe’s invention of oil immersion in 1878 up to today’s phase contrast, DIC, confocal and superresolution microscopy, ZEISS has always been driving scientific discoveries through innovative microscopy techniques. The 21st century is widely recognized as the age of digitization. Powerful new computer technology and algorithms can now process vast amounts of raw data and lead to scientific discoveries. Automated widefield imaging systems allow for high-throughput multi-channel fluorescence screening of cell cultures, small organisms and histology samples, including data processing and archiving. Widefield microscopy today is both cost-efficient and easy to use with established protocols for a broad range of neuroscience applications. However, thick samples such as developing organisms, brain tissue or organoids can pose challenges as a result of the digital camera collecting additional light from above and below the focal plane. This is where modern point scanning confocal microscopes come into play,

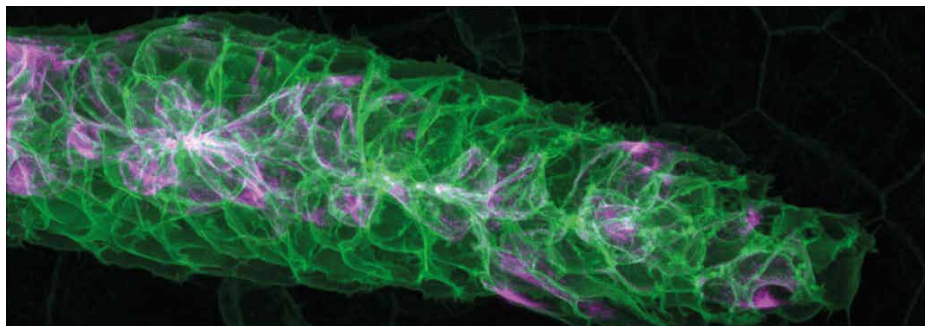


Figure 2.: Lateral line primordium migration and deposition of immature neuromasts in a Zebrafish embryo. Acquired with ZEISS Celldiscoverer 7 and LSM 900. Courtesy of J. Hartmann and D. Gilmour, EMBL, Heidelberg, Germany.

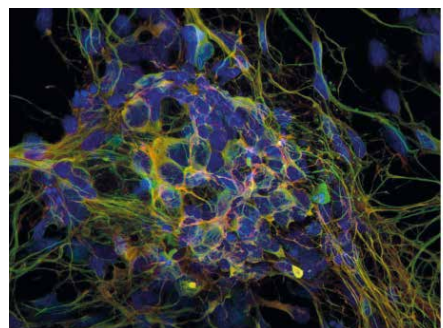


Figure 3.: Maximum intensity projection of neurosphere, multi-color label with DAPI (blue), Tubulin-Cy2 (green), DCX-Cy5 (red). Acquired with ZEISS LSM 980 and Airyscan 2 in Multiplex mode. Sample courtesy of H. Braun, LSM Bioanalytik GmbH, Magdeburg, Germany.

delivering high-contrast 3D imaging and advanced spectral imaging capabilities for methods such as Brainbow.

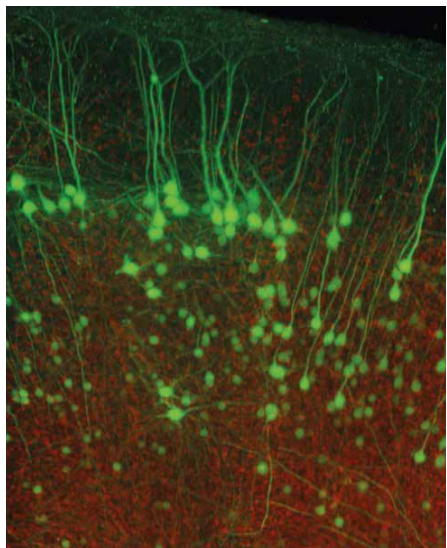
Figure 2 & 3: The development of new detector technologies such as ZEISS Airyscan extends the capabilities of confocal microscopy systems by introducing much greater light efficiency, resulting in gentle superresolution imaging with high sensitivity. This also addresses the inherent issues of photobleaching and phototoxicity. When deep tissue penetration is a must—for example, in intravital brain imaging or very thick cleared ex vivo brain sections—the confocal microscope can be upgraded for multiphoton excitation imaging with a pulsed tunable laser and non-descanned detectors. This allows optical sections of

deep tissue layers to be acquired without the scattering effects that usually occur, while still involving photobleaching from high light intensities.

Figure 4 & 5: Here, illumination light is introduced to the focal plane with a thin sheet of light formed by the excitation optics. Lightsheet fluorescence microscopy (LSFM)—also known as Selective Plane Illumination Microscopy/SPIM—is a conceptually new technology that virtually eliminates photo-damaging effects to the sample. The image is recorded perpendicularly by a high-speed digital camera through the detection optics, resulting in a very fast and sensitive optical sectioning technique. LSFM is ideally suited to recording the neuronal development of living organisms such

as zebrafish and to volume rendering of optically-cleared brain tissues. It can even visualize brain activity in 3D at single-cell level, using zebrafish calcium indicator dyes at maximum temporal resolution. When it comes down to the finest details of neurons at the subcellular level, single molecule localization microscopy (SMLM)—including PALM/dSTORM/PAINT—takes neuroscience beyond the diffraction limit of conventional microscopy techniques, enabling the researcher to gather information at the molecular scale—for example, ultra-fast synaptic processes such as vesicle trafficking in real-time with Lattice SIM.

Figure 6–8: For even higher structural resolution, scientists need to employ electron microscopy techniques. However, while



◀ **Figure 4.**: Thy1-EGFP M-line mouse whole mount, optically cleared in LUMOS clearing agent, co-stained with propidium iodide. Acquired with ZEISS Lightsheet Z.1 modified for imaging optically cleared specimen.
Imaging parameters: ZEISS 20x/1.0 immersion lens for RI=1.45 (WD= 5.6 mm), voxel size: (x:y:z) 330 x 330 x 500 nm, volume size: 2.9 x 0.9 x 3.25 mm (8950 x 2755 pixel and 6500 z-sections), data processing and 3D rendering in arivis vision 4D software (www.arivis.com)

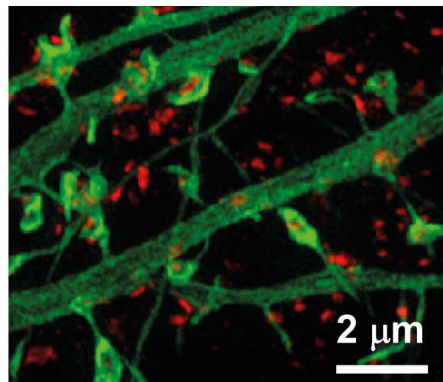


Figure 5.: Mouse brain. Cultured primary hippocampal neurons. Acquired with ZEISS Elyra in SIM mode. Sample courtesy of M. Schell, Uniformed Services University, Bethesda, USA.

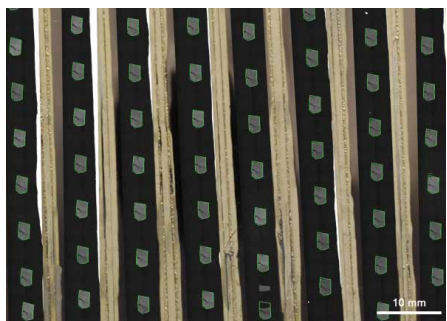


Figure 6.: Mouse brain. Serial sections on a silicon wafer prepared for imaging with ZEISS Atlas 5 Array Tomography. Courtesy of J. Lichtman, Harvard, USA.

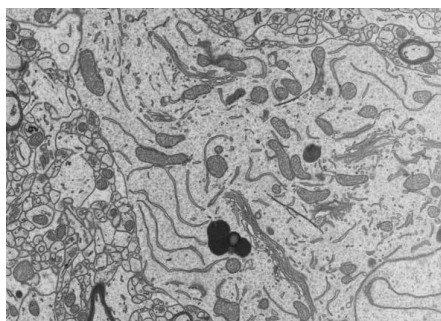


Figure 7.: Mouse brain. OTO stained. Acquired with ZEISS Crossbeam 540. Sample courtesy of C. Genoud, FMI, Basel, Switzerland.

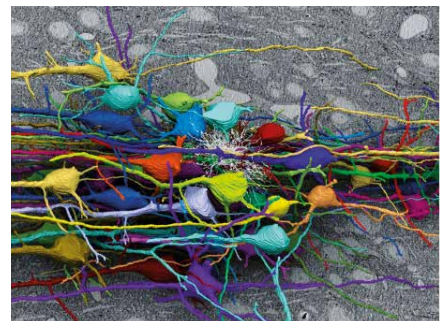


Figure 8.: Mouse brain. 3D reconstruction of single neurons from serial sections. Courtesy of D. Berger, Department of Brain and Cognitive Sciences, MIT; and J. Lichtman, Harvard, USA.

brain organization is naturally three dimensional, these electron techniques are inherently limited to fixed sample tissues and 2D surface imaging. To overcome the latter limitation, various technologies have emerged over the past few years. These include automated array tomography workflows with integrated sample preparation and large-area imaging as well as 3D volume reconstruction (ATUMtome from RMC Boeckeler with ZEISS Atlas 5), enabling ultra-high-resolution datasets of whole brain sections while preserving the samples for further investigation and archiving. On the other hand, if sample preservation and large areas are not your research focus, you can achieve even higher resolved 3D reconstruction of your most demanding samples by using serial block-face SEM (SBF-SEM) imaging with

Gatan 3View® integrated microtome and Focal Charge Compensation. The next step in 3D imaging of ultra-high resolved details is focused ion beam milling (FIB-SEM), which enables selective removal of sections down to 3 nm and continuous imaging for the highest demands in 3D volume reconstruction at the nanometer level.

Figure 9 & 10: But that still doesn't provide large-area imaging with the highest efficiency at nanometer resolution. To that end ZEISS has developed MultiSEM to provide up to 91 parallel electron beams covering a huge sample area. Designed for continuous, reliable 24/7 operation, the labs at Lichtman (Harvard) and Denk (Munich) are among the first to use this nanometer-resolving imaging machine, aiming to unravel the last secrets

of the brain by generating terabytes of data to help form a better understanding of the nervous system. And finally, there is X-ray microscopy, which unifies CT and synchrotron architectures, combining two magnification steps to provide the three-dimensional density distribution within cells and brain tissues without staining and slicing.

In all these ways we see that the future is multi-modal, with many imaging techniques being developed to take on new challenges as they arise. At ZEISS we are striving to unify your scientific data with ZEN Connect, making sure your data will overlay and be organized correctly with multimodal data from any source.

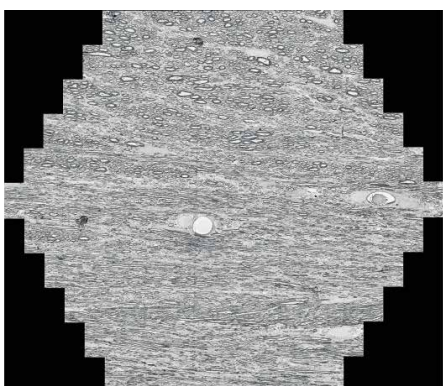


Figure 9.: Mouse brain. 50 nm thick section. Acquired with ZEISS MultiSEM 506, covering a hexagonal field of view of 165 µm x 143 µm at 4 nm pixel size. Sample courtesy of J. Lichtman, Harvard, USA.



Figure 10.: Zebrafish embryo. Acquired with ZEISS Xradia Versa. Virtual cross-section of showing eye and nerve bundle distribution with cellular resolution.

In vivo Ca^{2+} imaging of astrocytic microdomains reveals a critical role of the amyloid precursor protein for mitochondria

Montagna E, Crux S, Luckner M, et al.

The investigation of amyloid precursor protein (APP) has been mainly confined to its neuronal functions, whereas very little is known about its physiological role in astrocytes. Astrocytes exhibit a particular morphology with slender extensions protruding from somata and primary branches. Along these fine extensions, spontaneous calcium transients occur in spatially restricted microdomains. Within these microdomains mitochondria are responsible for local energy supply and Ca^{2+} buffering. Using two-photon in vivo Ca^{2+} imaging, the authors report a significant decrease in the density of active microdomains, frequency of spontaneous Ca^{2+} transients and slower Ca^{2+} kinetics in mice lacking APP. Mechanistically, these changes could be potentially linked to mitochondrial malfunction as in vivo and in vitro data revealed severe, APP-dependent structural mitochondrial fragmentation in astrocytes. Functionally, such mitochondria exhibited prolonged kinetics and morphology dependent signal size of ATP-induced Ca^{2+} transients. These results highlight a prominent role of APP in the modulation of Ca^{2+} activity in astrocytic microdomains whose precise functioning is crucial for the reinforcement and modulation of synaptic function. Furthermore, this study provides novel insights in APP physiological functions which are important for the understanding of the effects of drugs validated in Alzheimer's disease treatment that affect the function of APP.

Nowadays the active role of astrocytes in regulating brain networks, refining synapses, shaping the extracellular space and modulating the metabolic trafficking of neuro- and gliotransmitters is widely accepted. Therefore, the authors focused in their study on the role of APP in astrocytes, as active partners in synaptic function. Namely, astrocytes exhibit intracellular Ca^{2+} transients that drive gliotransmitter release important for the modulation of neuronal function. Montagna et al. considered the effects of APP depletion on spontaneous in vivo Ca^{2+} dynamics within microdomains of astrocytic fine processes known to be closely associated with synapses. It is of importance to understand the local function of these microdomains in order to decode the contribution of APP to the communication between astrocytes and neurons.

APP controls the density of microdomains

The in vivo two-photon imaging results clearly demonstrate that lack of APP affects the density of microdomains, with a significant loss of small active domains compared with control animals. Moreover, frequency and kinetics of Astrocytic Spontaneous Calcium Transients (ASCaTs) along the astrocytic fine processes were reduced as well, without any substantial change in amplitude. Since a mouse model of constitutive APP knockout (APP-KO) was used, a secondary effect from neurons on astrocytic activity cannot be excluded. Although basal neuronal activity was reported to be unchanged in APP-KO animals, the interaction between neurons and astrocytes in APP-KO should be investigated more closely in future studies. Given that Ca^{2+} transients along the fine processes of astrocytes are regulated by mitochondria-mediated ion homeostasis, possible mitochondria dysfunctions were hypothesized and investigated. To monitor ex vivo the network of astrocytic mitochondria in APP-KO mice, an immunohistological analysis of mitochondria

cluster associated with Glial fibrillary acidic protein (GFAP)-positive astrocytic branches was performed by mean of confocal imaging. These observations revealed that conventional confocal imaging has limited resolution in identifying mitochondria within astrocytic microdomains, and sampling is limited to GFAP-positive cell that represent only reactive astrocytes. Although further in vivo studies are required, the analysis gave a hint of a significant increase of fragmentation of mitochondria network, potentially detrimental, associated with big branches of GFAP-positive APP-KO astrocytes. To overcome to this limitation, the authors focused on isolated astrocytic cultures.

Mitochondria fragmentation and altered Ca^{2+} kinetics

Consistent with the hypothesis, APP-KO cultured astrocytes exhibited mitochondrial network fragmentation which could be rescued by reintroduction of APP (Fig. 1). As a result of the mitochondria fragmentation observed by focused ion beam (FIB)/scanning electron microscopy (SEM) analysis with

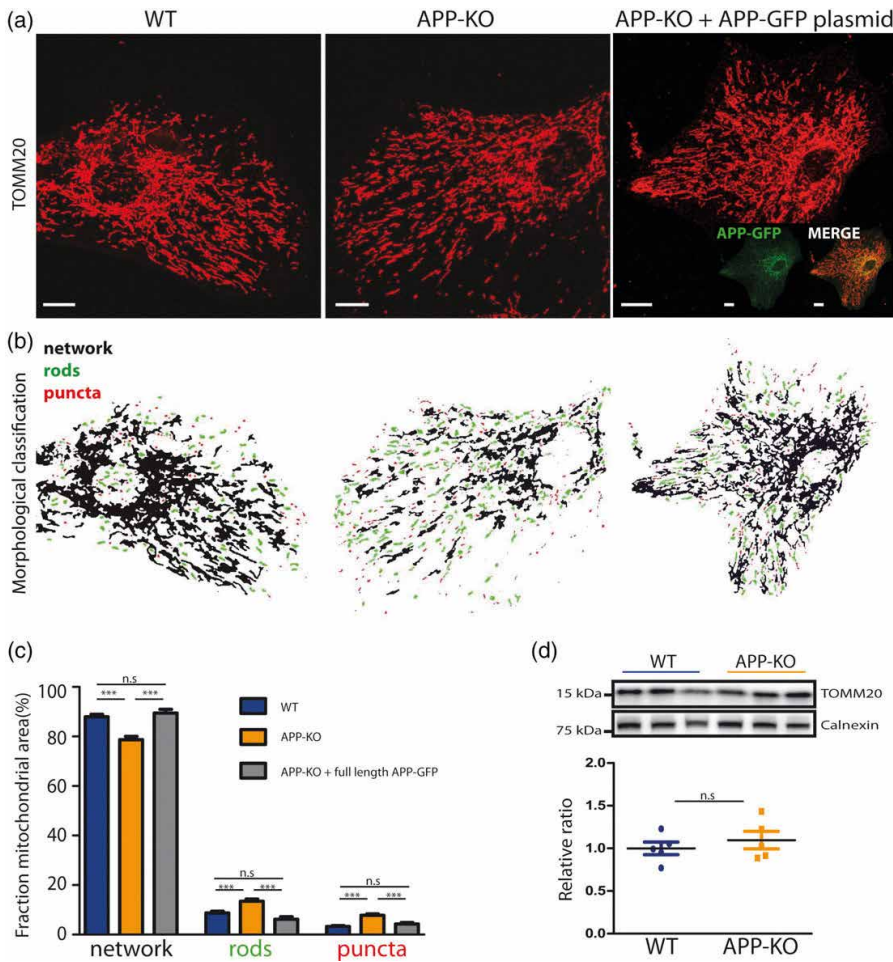


Fig. 1.: Amyloid precursor protein (APP)-knockout (KO) astrocytic mitochondria have more fragmented morphology than wild type (WT) which can be restored by reintroduction of full-length APP. (a) Confocal microscopy images of TOMM20-positive astrocytic mitochondria (in red) from WT, APP-KO, and APP-KO + full length APP-green fluorescent protein (GFP; in inset). Scale bars = 10 μm. (b) Representative reconstructions of mitochondrial morphology based on TOMM20 staining. Morphology classes: "Network" (black), "rods" (green) and "puncta" (red). (c) Quantification of mitochondria morphology. Mitochondria of APP-KO astrocytes were more fragmented compared with WT controls. The reintroduction of full length APP restored physiological composition of mitochondria network in astrocytes. (one-way ANOVA for puncta: $F(2,87) = 21.14, p < .001$; rods: $F(2,87) = 18.38, p < .001$; networks $F(2,87) = 19.78, p < .001$). (d) Western blot of TOMM20 and calnexin, (house-keeping protein) and their quantification. TOMM20/calnexin-ratio revealed no difference between WT and APP-KO astrocytes. Bonferroni's post hoc test: * $p < .001$**

Zeiss Crossbeam 340 (Fig. 2), microdomains may get deprived of their main energetic sources and cannot sufficiently support surrounding neuronal activity. Therefore, the authors hypothesize that the distal, highly ramified protrusions of astrocytes, where microdomains are located, are not fully functional in APP-KO mice, thus explaining the impairments in synaptic plasticity and gliotransmitter release observed in APP-KO animals as published before. Furthermore, fragmented mitochondria of APP-KO astrocytes displayed prolonged kinetics of Ca^{2+} uptake during extracellular stimulation with ATP suggesting decelerated Ca^{2+} signaling (Fig. 3). The prolonged kinetics in mitochondria of astrocytes show striking parallels to the ASCaTs in vivo. It is important to note that Astrocytes in culture have different morphological properties in comparison to astrocytes in the intact brain. Nevertheless, cell culture-based assays offer an advantage to study and genetically manipulate isolated astrocytes.

It is known that APP harbors a mitochondrial targeting signal and forms complexes with the translocase of the outer mitochondrial membrane 40 (TOMM40) and the translocase of inner mitochondrial membrane 23 (TIMM23), regulating the translocation of nuclear-encoded proteins into the mitochondria. Therefore, it has been reasoned that depletion of APP may compromise mitochondrial protein translocation affecting mitochondrial functions and leading to imbalanced intracellular Ca^{2+} homeostasis. In fact, the mitochondria-associated membranes (MAMs) are sites where the APP cleavage product C99 accumulates and interferes with the mitochondrial respiratory chain. Hence, it can be speculated that full-length APP or any of its cleavage products at physiological levels have a function in ensuring ER-mitochondria proximity and thus permitting adequate mitochondria integrity.

The altered mitochondrial Ca^{2+} signals during ATP stimulation might result from changed release of Ca^{2+} from the ER or mod-

ified interaction of ER and mitochondria in the absence of APP. Dysregulation of the ER and mitochondria contact sites might also be a reason for prolonged kinetics of the ASCaTs in vivo. The changed kinetics might also result from altered Ca^{2+} buffering capacities due to a smaller and fragmented mitochondrial volume. The study of Montagna et al. show mitochondria fragmentation in APP-KO primary astrocyte cultures and suggests that this is resulting from a missing localization of APP to mitochondria where it plays a physiological role. This is in line with a study observing altered mitochondrial morphology (increased proportion of cells exhibiting fragmented mitochondria) and impaired mitochondrial function in HeLa cells that express engineered KPI-APP variants with decreased mitochondrial localization. Also, an increased level of reactive oxygen species (ROS) in the absence of KPI-domain in HeLa cell line has been reported before. Thereby, the increased ROS levels are conflicting to decreased number

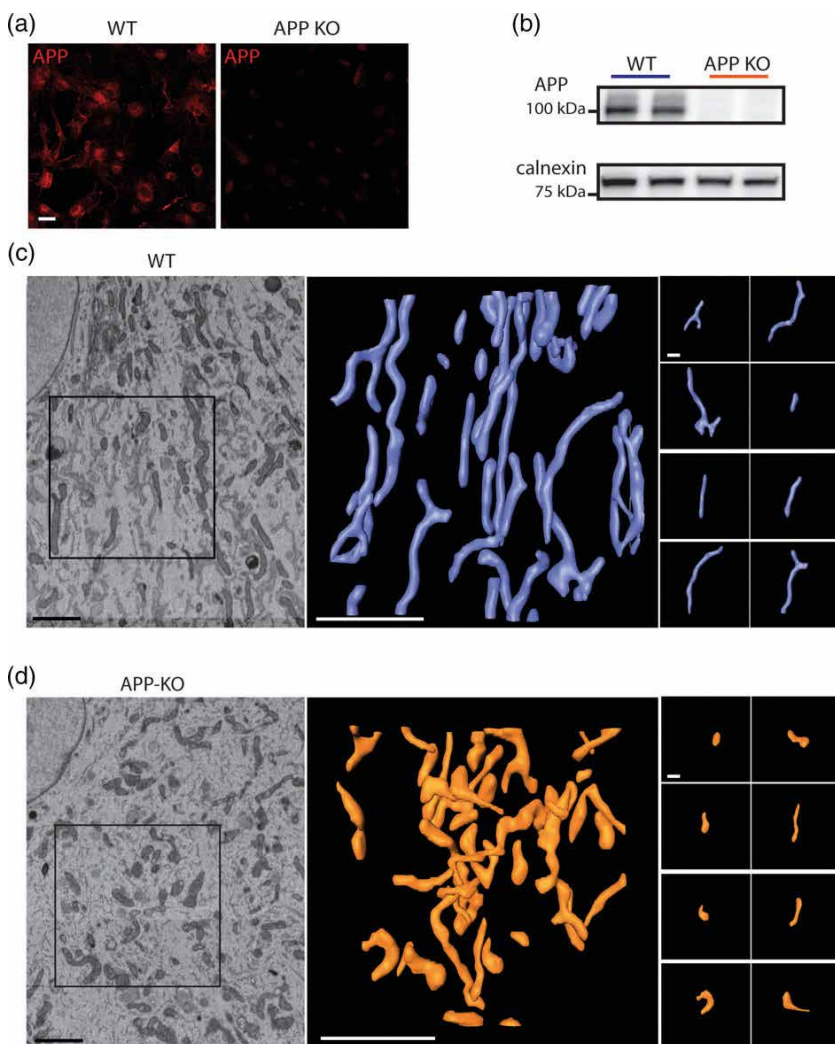


Fig. 2.: Primary cultured astrocytes lacking APP display fragmented mitochondrial morphology. (a) Immuno-histochemical analysis with C-terminus targeted APP antibody on wild type (WT; left) and APP-knockout (KO; right) primary astrocytes shows exclusive expression of APP in WT. Scale bar = 40 μ m. **(b)** Western blot analysis of primary astrocyte lysates confirms the absence of APP in APP-KO astrocytes with C-terminus targeted APP antibody. Representative focused ion beam (FIB)/scanning electron microscopy (SEM) of WT (c) and APP-KO (d) cultured astrocytes with detailed images of 3D-reconstructions (right) illustrate the fragmentation of mitochondria in APP-KO astrocytes. Original FIB/SEM image, scale bar = 2 μ m; overview reconstruction (middle), scale bar = 2.5 μ m, single mitochondria fragments, scale bar = 1 μ m.

of microdomain Ca^{2+} events that is reported in this study in astrocytes *in vivo*. However, the enlargement of microdomains in APP-KO astrocytes indicates a spatial extension of Ca^{2+} elevations in the cell. Besides the differences between *in vitro* and *in vivo* approaches, the truncation of Kunitz protease inhibitor (KPI)-APP alone has potentially different effects than full APP-KO resulting in distinct compensatory mechanisms. As KPI-containing APP isoforms are primarily expressed in astrocytes, it is to presume that the mitochondrial fragmentation and the consequent ASCaTs alteration in APP-KO mice are mainly an astrocyte-specific feature. Previous *in vivo* studies on anaesthetized AD mouse models overexpressing mutated APP reported hyperactivity of Ca^{2+} signaling detected by a somatic Ca^{2+} indicator. Thereby, the purinergic receptors P2Y1 was shown to be crucially involved in Ca^{2+} hyperactivity in reactive astrocytes close to plaques. The Ca^{2+} hyperactivity of astrocytes

in Alzheimer's disease (AD) models in contrast to reduced ASCaTs in APP-KO animals further suggests a physiological role of APP in astrocytic function that critically depends on levels of APP expression.

Summary

This is the first *in vivo* study to investigate the role of APP in astrocytes. It could be demonstrated that the lack of APP influences Ca^{2+} dynamics in astrocytes and that this effect could be mechanistically linked to the altered mitochondrial function, breaking ground for further investigations on APP function in astrocytes that has been neglected for too long. It has also been shown that mitochondrial network fragmentation can be observed both *in vivo* and *ex vivo*, suggesting that lack of APP causes unbalanced intracellular Ca^{2+} homeostasis causing mitochondrial dysfunction. Here it

should be mentioned that correlative workflows connecting multiple imaging modalities become increasingly important for the understanding of brain functions.

Digest
of Montagna E, Crux S, Luckner M, et al.;
In vivo Ca^{2+} imaging of astrocytic microdomains reveals a critical role of the amyloid precursor protein for mitochondria;
Glia 2019;1–14.
© 2019 Wiley Periodicals, Inc.
<https://doi.org/10.1002/glia.23584>

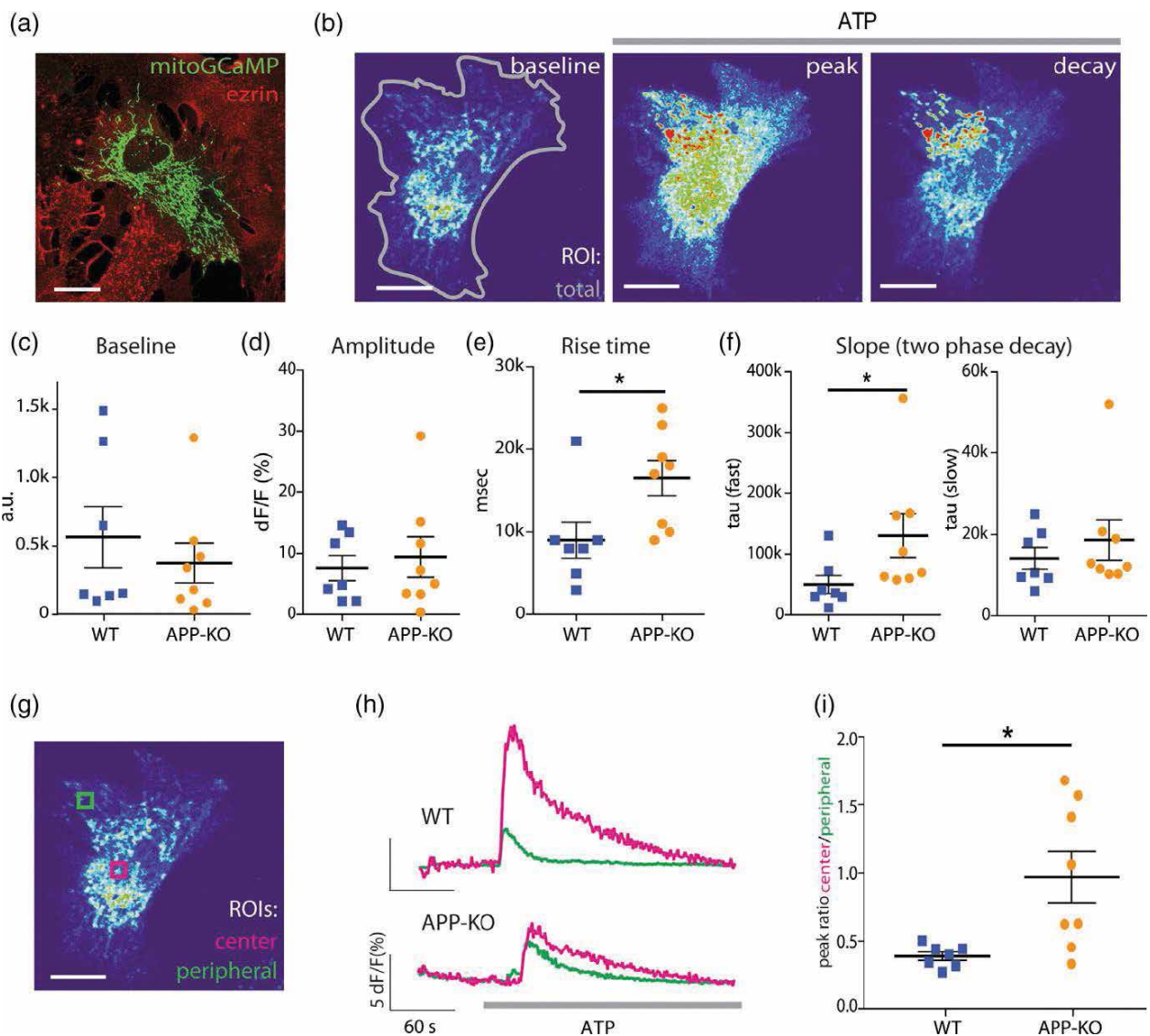


Fig. 3.: Mitochondria of APP-KO display altered kinetics and spatial differences of Ca^{2+} uptake after ATP stimulation.

(a) Confocal image of an astrocyte transfected with mitochondria-targeted GCaMP (green, mitoGCaMP). Astrocytic cytoskeleton protein ezrin (red) confirms the cell identity. Scale bar = 20 μ m.

(b) Illustration of the mitochondrial Ca^{2+} signal before and during ATP stimulation. Region of interest (ROI) encircling total mitochondrial Ca^{2+} signal (gray border). Left: Baseline before the presence of ATP; center: Peak, highest mitochondrial Ca^{2+} signal in presence of ATP; right: Decay phase when ATP is still in the bath.

(c) Baseline fluorescence before peak (Mann–Whitney: $U = 23$, test $p > .5$).

(d) Amplitude $\Delta F/F$ ($U = 26$, $p > .5$).

(e) Rise time of Ca^{2+} signal is longer in APP-KO astrocytes ($U = 7$, $p < .05$).

(f) The decay of the Ca^{2+} signal displayed two phases: Tau fast component lasts longer in APP-KO ($U = 9$, $p < .05$) while tau slow component displayed no differences ($p > .05$, $U = 20$, $n = 7–8$) between APP-KO and WT.

(g-i) Analysis of $\Delta F/F$ center/peripheral.

(g) Illustration of ROI position in center (magenta) and peripheral (green) in the mitochondrial signal.

(h) Example traces of center and peripheral traces of WT (top) and APP-KO

Blood–brain barrier disruption and angiogenesis in a rat model for neurocysticercosis

Carmen-Orozco R P, Dávila-Villacorta D G, Cauna Y, et al.

Neurocysticercosis (NCC) is a helminth infection affecting the central nervous system caused by the larval stage (cysticercus) of *Taenia solium*. Since vascular alteration and blood–brain barrier (BBB) disruption contribute to NCC pathology, it is postulated that angiogenesis could contribute to the pathology of this disease. This study used a rat model for NCC and evaluated the expression of two angiogenic factors called vascular endothelial growth factor (VEGF-A) and fibroblast growth factor (FGF2). Also, two markers for BBB disruption, the endothelial barrier antigen and immunoglobulin G, were evaluated using immunohistochemical and immunofluorescence techniques. Brain vasculature changes, BBB disruption, and overexpression of angiogenesis markers surrounding viable cysts were observed. Both VEGF-A and FGF2 were overexpressed in the tissue surrounding the cysticerci, and VEGF-A was overexpressed in astrocytes. Vessels showed decreased immunoreactivity to endothelial barrier antigen marker and an extensive staining for IgG was found in the tissues surrounding the cysts. Additionally, an endothelial cell tube formation assay using human umbilical vein endothelial cells showed that excretory and secretory antigens of *T. solium* cysticerci induce the formation of these tubes. This in vitro model supports the hypothesis that angiogenesis in NCC might be caused by the parasite itself, as opposed to the host inflammatory responses alone.

For this study, mounted brain slices of 30 µm were observed with Zeiss LSM 880 Airy-scan confocal microscope and 30 µm cryostat sections for immunofluorescence analysis. Immunohistochemistry was performed with an AxioCam ERc5 camera coupled to a Zeiss Axio Lab.A1 microscope.

The authors showed that brain vasculature changes, BBB disruption, and overexpression of angiogenesis markers surrounding viable cysts in intracranially inoculated rats. Changes in brain vasculature showed fibrosis and possible dysfunction in vessels surrounding the cysts (Fig. 1). VEGF-A and FGF2, used for angiogenesis evaluation, were overexpressed in the tissue surrounding *T. solium* cysticerci, and their expression varied depending on the location of the parasite (Fig. 2). Moreover, VEGF-A overexpression was associated with astrocytes, reflecting the possible importance of this cell's role in NCC pathology (Fig. 3). In vitro assays also revealed that cysticercus antigens were able to induce angiogenesis. BBB evaluation showed that most of the cysticerci were associated with some degree of BBB alteration. Since only viable cysts were evaluated, this study indicates that BBB disruption begins even before a viable cyst starts degenerating, which potentially contributes to NCC pathogenesis.

Potential influence of VEGF-A and FGF2 on NCC

VEGF-A was overexpressed in host tissue adjacent to parenchymal cysts and corticomeningeal cysts, whereas ventricular cysts had a non-significant increase in expression of VEGF-A (Fig. 2a). Such overexpression reflects major changes in cysts that are in close contact with the brain tissue. VEGF-A overexpression in astrocytes is associated with BBB disruption. While these results showed VEGF-A overexpression in astroglia (Fig. 3), this phenomenon was not seen in microglial cells, suggesting that a possible interaction exists between VEGF-A and BBB disruption in NCC pathology. VEGF-A is a mitogenic factor and in vitro studies have shown that it increases the proliferation and mobility of astrocytes. VEGF-A is also the principal protein which induces angiogenesis and its overexpression has been associated with many neuropathologies. However, the contribution of this protein to the pathology of NCC has not yet been studied. Studies in temporal lobe epilepsy have shown that angiogenesis is associated with BBB disruption, so studying this association in NCC patients with epilepsy could be important.

FGF2 is a potent neurotrophic and angiogenic factor. It is expressed in many cell types within the brain, including astrocytes, capillary endothelial cells, pericytes, and neurons. In addition, FGF2 is a potent mitogenic factor and regulates proliferation of astrocytes. Its overexpression found around the cysticerci could explain the marked presence of gliosis, fibrogenesis, and angiogenesis in NCC. FGF2 overexpression has been reported before in cerebral vessels in NCC patients with granulomas. The present study found FGF2 overexpression in fibrotic tissue and areas of gliosis (Fig. 2b). Research on brain tissue of epilepsy patients showed FGF2 overexpression, which increases the excitability and hence susceptibility to seizures, and which also helps to prevent cell death. Therefore, the FGF2 changes demonstrated in this study could promote future studies into the contribution of FGF2 to epileptogenesis in NCC.

Induced angiogenesis

In inflammatory processes, angiogenesis is initiated by different cell populations, such as macrophages, mast cells, fibroblasts, and endothelial cells. These cells produce angiogenic factors such as VEGF, FGF, plate-

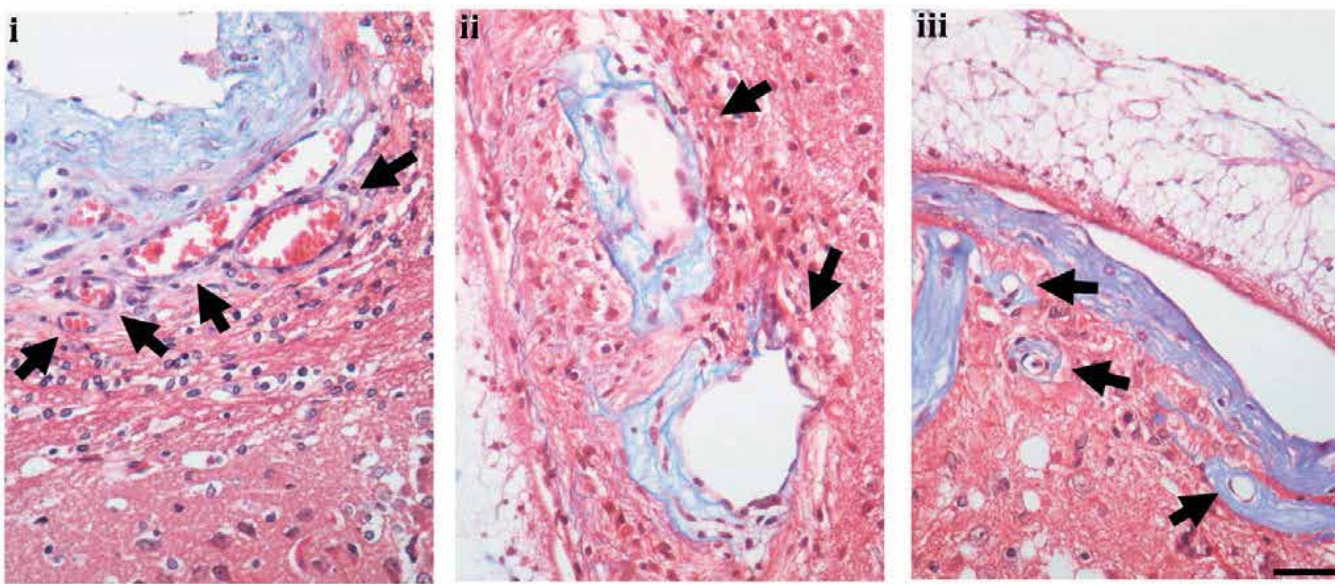


Fig. 1.: Fibrosis and fibrotic vessels surround cysticercus in NCC model. Thirteen of the 18 inoculated rats (8 males and 5 females) developed cysts (72.2% rate of infection). All of the cysts showed intact teguments and angiogenic vessels and were considered viable. It was previ-

ously reported by the authors the presence of angiogenic vessels, but here they were able to demonstrate the three different types of vessel alterations. (i) dilated vessels without fibrotic tissue (arrow), (ii) dilated vessels with fibrotic tissue (arrow) and (iii) sclerotic vessels (arrow)

shown by Trichrome Masson staining. Scale bar 50 μ m. The cysts were classified according to their location. 11 cysts were considered parenchymal, 8 were considered corticomeningeal, and 8 were considered ventricular. Vessel alterations were present in all cyst locations.

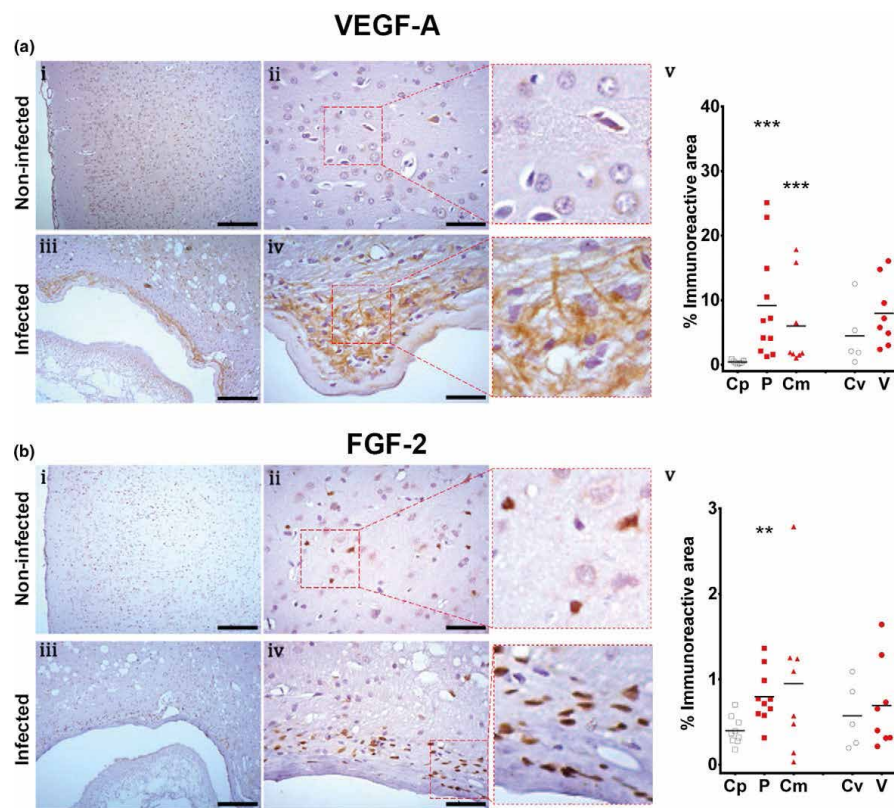


Fig. 2.: Expression of angiogenic factors in NCC model shown by immunohistochemistry. Panel a, VEGF expression, Control region (C_p , $n = 7$), parenchymal cyst (P , $n = 11$), corticomeningeal cyst (C_m , $n = 8$), control region of the ventricle (C_v , $n = 5$), ventricular cyst (V , $n = 8$). Panel b, FGF2 expression. Control region (C_p , $n = 9$), parenchymal cyst (P , $n = 10$), corticomeningeal cyst (C_m , $n = 8$), control region of the ventricle (C_v , $n = 5$), ventricular cyst (V , $n = 8$). Control brains (i), (ii) and infected brains (iii), (iv). (i), (ii) scale bar 200 μ m. (iii), (iv) scale bar 50 μ m. (v) comparison of the immunoreactive area by cyst location. Mann–Whitney U, * $p < 0.05$, ** $p < 0.001$, *** $p < 0.0001$.

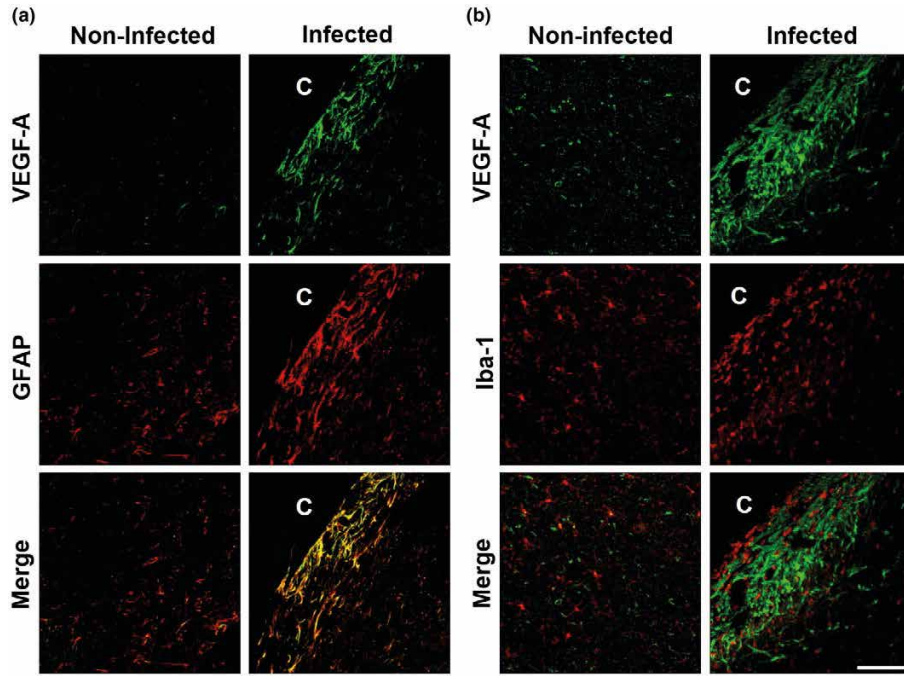


Fig. 3.: VEGF-A and glial cells double staining. C shows cysticercus location. Panel a, GFAP and VEGF-A double labeling. Control regions show colocalization between VEGF-A and GFAP and some Iba-1 positive cells colocalize with VEGF-A. Infected regions show most VEGF-A overexpression colocalizing with GFAP. Panel b, Iba-1 and VEGF-A double labeling. In control regions

some microglial cells colocalized with VEGF-A (yellow). Non-colocalization is observed between Iba-1 and VEGF-A in infected brains. Scale bar 100 μ m. GFAP and Iba-1 immunofluorescence reacted strongly in cells surrounding the parasite. Astrocytes positive to GFAP exhibited a gliotic network shape, and phagocytes positive to Iba-1 showed a widespread reaction close to the parasite. Double staining of

VEGF-A and glial cells (GFAP or Iba-1 positives) in non-infected brain showed most cells colocalizing with GFAP, while a few colocalized to Iba-1. While infected brains showed a strong reaction between GFAP and VEGF-A, no colocalizing between Iba-1 and VEGF-A was detected, suggesting that most VEGF-A overexpression is produced by astrogliosis.

let derived growth factor, and tumor necrosis factor alpha, among others. Therefore, it is necessary to establish whether there is an association between the inflammation found in NCC and the expression of the angiogenic markers reported in this study. NCC is a chronic disease and recent reports indicate that angiogenesis accompanied by chronic inflammation tends to intensify and prolong the immune response. Inflammation in NCC could contribute to the production of angiogenic factors, however, in this study, only viable cysts, which tend to have a scarce inflammatory reaction, were evaluated. In this article, in vitro results were presented that cysticercus antigens are able to induce angiogenesis in the absence of inflammation, leading to hypothesize that inflammation is not the only cause of angiogenic responses.

BBB disruption in NCC model

The Authors have previously reported diffuse IgG staining surrounding cysticerci. Here they have demonstrated cellular staining, likely representing macrophages or plasma cells. This suggests that IgG diffusion could be a result of the inflammatory response, instead of being caused only BBB leakage. However, the present observations from EBA, reinforce the idea that BBB dysfunction is observed even when cysts are viable. These results are not compatible with previous reports in pigs, where most of viable cysts do not exhibit BBB disruption detected by macroscopic evaluation of Evans blue extravasation (Fig. 4). Nonetheless, Carmen-Orozco et al. findings used the IHC staining approach and indicate BBB dysfunction rather than protein extravasation. Even though EBA staining results showed alteration in most of the evaluated cysticerci and Evans blue showed alteration in only a few, it is known that both methods are able to detect different levels of BBB dysfunction. Evans blue staining demonstrates

protein extravasation, whereas EBA is a group of different proteins with an unclear role in BBB maintenance. EBA proteins down regulation has been correlated with BBB dysfunction in different models and diseases. Even though the authors tested fibrinogen extravasation here (Fig 4b), its staining indicates that it is sparsely present in the fibrotic tissue, possibly because there is not enough BBB dysfunction at this level of the disease to allow large proteins such as fibrinogen (340 kDa) to move across the BBB and into the brain parenchyma.

BBB of Parenchymal, corticomeningeal and ventricular cysts

In parenchymal and corticomeningeal cysts, the investigations of the authors showed a stronger expression of angiogenic markers (VEGF-A and FGF2) in comparison to the control regions (Fig. 2), as well as increases in IgG abundance and number of vessels that are not immunoreactive to EBA. These

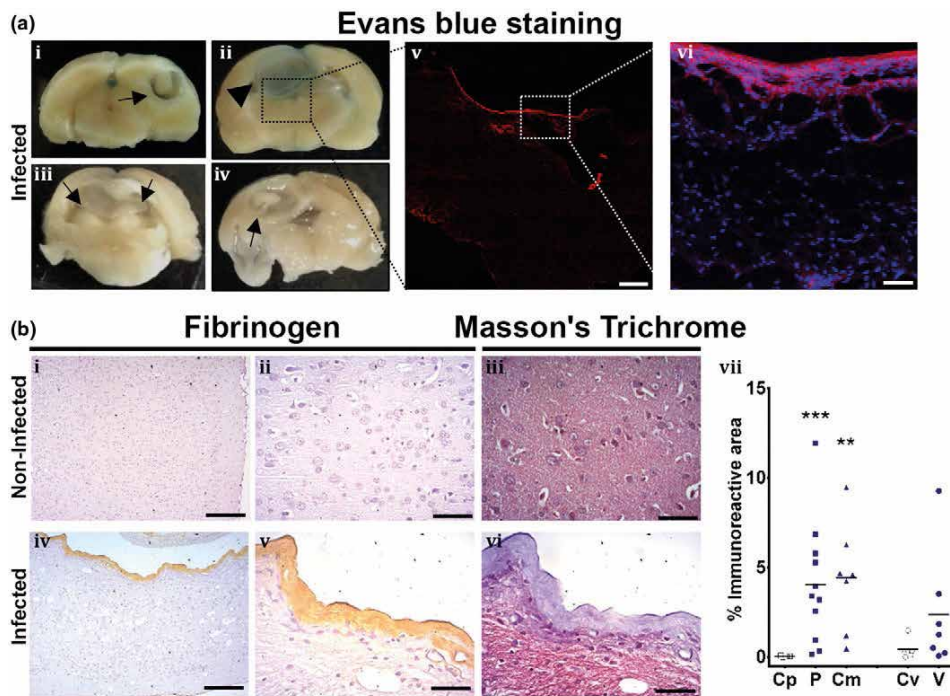


Fig. 4.: Evans blue extravasation and fibrinogen. Panel a, Evans. Blue staining. (i)–(iv) show the brain of 4 infected rats, arrows show cysts, arrowhead shows blue staining surrounding the cyst. (v) magnification of iii, shows red fluorescence in the border of the cyst (scale bar, 1 mm). (vi) magnification image shows Evans blue extravasation

in the parenchymal tissue (evans blue in red, DAPI in blue, scale bar 50 μ m). Panel b, Fibrinogen presented in fibrosis. (i)–(iii) represent non-infected brain, no evidence of fibrogen or fibrosis is observed. (iv)–(vi) shows infected brain, fibrinogen is observed in the fibrotic tissue, confirmed by Masson's trichrome staining. Images at low magnification (i) and (iv), scale bar 200 μ m.

High magnification images, scale bar 50 μ m. (vii) shows fibrinogen inmunoreactive area by different cyst location. Control region (Cp, [n = 6]), parenchymal cyst (P, [n = 11]), corticomeningeal cyst (Cm, [n = 7]), control region of the ventricle (Cv, [n = 5]), ventricular cyst (V, [n = 7]). Mann-Whitney U, * $p < 0.05$, ** $p < 0.001$, *** $p < 0.0001$.

findings suggest that parenchymal and corticomeningeal cysts have a more intense cellular response compared to ventricular cysts. This may be due to the close contact between the parasite and brain tissue, where cells are more susceptible to tissue injury. The BBB of ventricular cysts was less compromised in comparison to parenchymal and corticomeningeal cysts, possibly due to the fact that ependymal cells protect the subventricular zone as part of the cerebroventricular barrier. Additionally, the presence of cerebrospinal fluid could cause parasite antigens to be diluted, which, in turn, could prevent an immune response from being elicited around the ventricles. Lastly, host-parasite physical contact could mediate injuries in corticomeningeal and parenchymal cysts, but not in ventricular cysts.

Parasites use different pathways to promote their survival and to evade host responses. Helminth antigens have been identified as molecules that promote angiogenesis. For example, beta-thymosin that is present in *Trichinella spiralis* and various anti-

gens found in the eggs of *Schistosoma mansoni* have been observed to induce angiogenesis. It is hypothesized that helminths can promote angiogenesis via two possible mechanisms: by acting directly in vessels, or, by mediating a proangiogenic response in tissues. In this study, novel findings are reported which show that cysticerci can induce tube formation in endothelial cells in vitro. This suggests that the cysticercus can directly affect brain vasculature by inducing angiogenesis, as opposed to only activating proangiogenic mechanisms in tissue.

Summary

This study is focused on understanding the blood-brain barrier (BBB) alteration which occurs in Neurocysticercosis, the main cause of acquired epilepsy worldwide. Carmen-Orozco et al. reported a novel finding in the *T. solium* rat model of NCC the over-expression of angiogenic factors VEGF-A and FGF2 and BBB disruption surrounding

the cyst. Furthermore, this report shows that cysticerci excretory-secretory processes alone can induce angiogenesis by endothelial cell tube formation in vitro assay. Due to the large roles played by VEGF-A and FGF2 in the processes of cell survival, proliferation, and inflammation, and because of their association with different pathologies of the central nervous system, such as epilepsy, studies of these growth factors could be used to understand the pathology and symptoms found in human NCC. The combination of widefield and histological methods with high end LSM immunostaining brought further insights into the functional pathology of *T. solium* induced cyterosis.

Digest of

Carmen-Orozco RP, Dávila-Villacorta DG, Cauna Y, et al.;
Blood-brain barrier disruption and angiogenesis in a rat model for neurocysticercosis; *Journal of Neuroscience Research* 2019; 97:137–148.

© 2019 Wiley Periodicals, Inc.
<https://doi.org/10.1002/jnr.24335>

Cone synapses in mammalian retinal rod bipolar cells

Pang J-J, Yang Z, Jacoby RA, Wu SM

Some mammalian rod bipolar cells (RBCs) can receive excitatory chemical synaptic inputs from both rods and cones (DBCR2), but anatomical evidence for mammalian cone-RBC contacts has been sparse. The authors examined anatomical cone-RBC contacts using neurobiotin (NB) to visualize individual mouse cones and standard immuno-markers to identify RBCs, cone pedicles and synapses in mouse and baboon retinas. Peanut agglutinin (PNA) stained the basal membrane of all cone pedicles, and mouse cones were positive for red/green (R/G)-opsin, whereas baboon cones were positive for calbindin D-28k. All synapses in the outer plexiform layer were labeled for synaptic vesicle protein 2 (SV2) and PSD (postsynaptic density)-95, and those that coincided with PNA resided closest to bipolar cell somas. Cone-RBC synaptic contacts were identified by: (a) RBC dendrites deeply invaginating into the center of cone pedicles (invaginating synapses), (b) RBC dendritic spines intruding into the surface of cone pedicles (superficial synapses), and (c) PKC α immunoreactivity coinciding with synaptic marker SV2, PSD-95, mGluR6, G protein beta 5 or PNA at cone pedicles. 20.7% and 38.9% of mouse RBCs contacted cones in the peripheral and central retina ($p < .05$, $n = 14$ samples), respectively, while 34.4% (peripheral) and 48.5% (central) of cones contacted RBCs ($p > .05$). In baboon retinas ($n = 4$ samples), cone-RBC contacts involved 12.2% of RBCs ($n = 416$ cells) and 22.5% of cones ($n = 225$ cells). This suggests that rod and cone signals in the ON pathway are integrated in some RBCs before reaching All amacrine cells.

Zeiss LSM 510 and LSM 800 confocal microscopes were used for immunocytochemical analysis to examine cone-RBC synapses (Fig. 1–3). Putative cone-RBC contacts in confocal optical sections crossing entire cone pedicles were examined with a vertical resolution of 0.4–1.0 μm under regular line-scan and frame-scan modes. Potential synaptic contacts were also studied in 1–2- μm -thick blocks using LSM 800 | Airyscan and software with a resolution of 30 nm per pixel. These Airyscan images were displayed by the 3D surface profile reconstructed from a series of optical sections obtained with a step of 150–180 nm.

Cone-RBC synaptic contacts

This study observed cone-RBC synapses in the mouse and primate retina (Fig. 1–3), providing anatomical evidence for previously revealed cone chemical synaptic inputs in mouse RBCs. The present data also revealed that mouse RBCs received cone contacts more frequently than primate RBCs, indicating these RBCs are functionally more important for nocturnal animals. Additionally, mouse RBCs were found to contact cones more frequently in the central retina than in the peripheral retina, consistent with the cone distribution peak in the central retina.

The results showed that cone-RBC synaptic contacts involved about 10% of RBCs and 20% of cones in baboon retinas and nearly 30% of RBCs and 40% of cones in the mouse retina. One RBC could form 0–1 invaginating and 1–3 superficial contacts with cones, while one cone could contact 1–3 RBCs. These data are well in line with the report from the mouse retina, though the RBC population contacting cones of the mouse retina in this report is smaller than in that recent study. The difference is possibly related to the difficulty in identifying RBCs and synapses. Immunocytochemistry and confocal microscopy generally have a lower resolution than electron microscopy for identifying synapses and can possibly cause an underestimation of the synapses. On the other hand, the former allows better identification of RBCs by their PKC α -immunoreactivity. Additionally, in this study all retinal preparations were never dehydrated, preventing examiners from mistaking physical contacts induced by artificial tissue deformation as synaptic contacts. Nevertheless, these data demonstrate that mammalian RBCs can integrate rod and cone signals.

Entire cone morphology and the boundary of cone pedicles

In recent decades, confocal microscopy and immuno-markers have been widely used for

studying rod and cone synapses. RBCs are often identified by a classic marker PKC α antibody, and cone pedicles are often identifiable by other immuno-markers, such as PNA, GluR5, and glycogen phosphorylase. Similar approaches were used in this study (Fig. 2 and 4), in conjunction with synaptic markers SV2, PSD-95, mGluR6, and GNB5. In addition, Pang et al. were able to visualize the entire cone morphology and the boundary of cone pedicles by neurobiotin labeling, as well as the staining for red/green (R/G) opsin. Anti-R/G-opsin antibody was used to label all mouse cones, because mouse cones all express M-opsin ($\lambda_{\text{max}} = 508$ nm).

In mammals, up to 13 morphological subtypes of cone bipolar cells have been identified, however, all RBCs belong to a single anatomical subtype. Previous data supporting this concept were obtained from light and electron microscopic studies in the cat, rabbit and primate retinas. RBCs across species show a similar morphology, as has been well described from Golgi-impregnated retinas. The synaptic connections of RBCs in the inner plexiform layer (IPL) of the cat, rabbit and primate appear to have the same general organization. Although in electron microscopic studies PKC α -positive RBC dendrites have been observed to invaginate into cone pedicles in primate and rabbit retinas, they were not statistically studied owing to their low frequency. Here, the present data show that cone-RBC

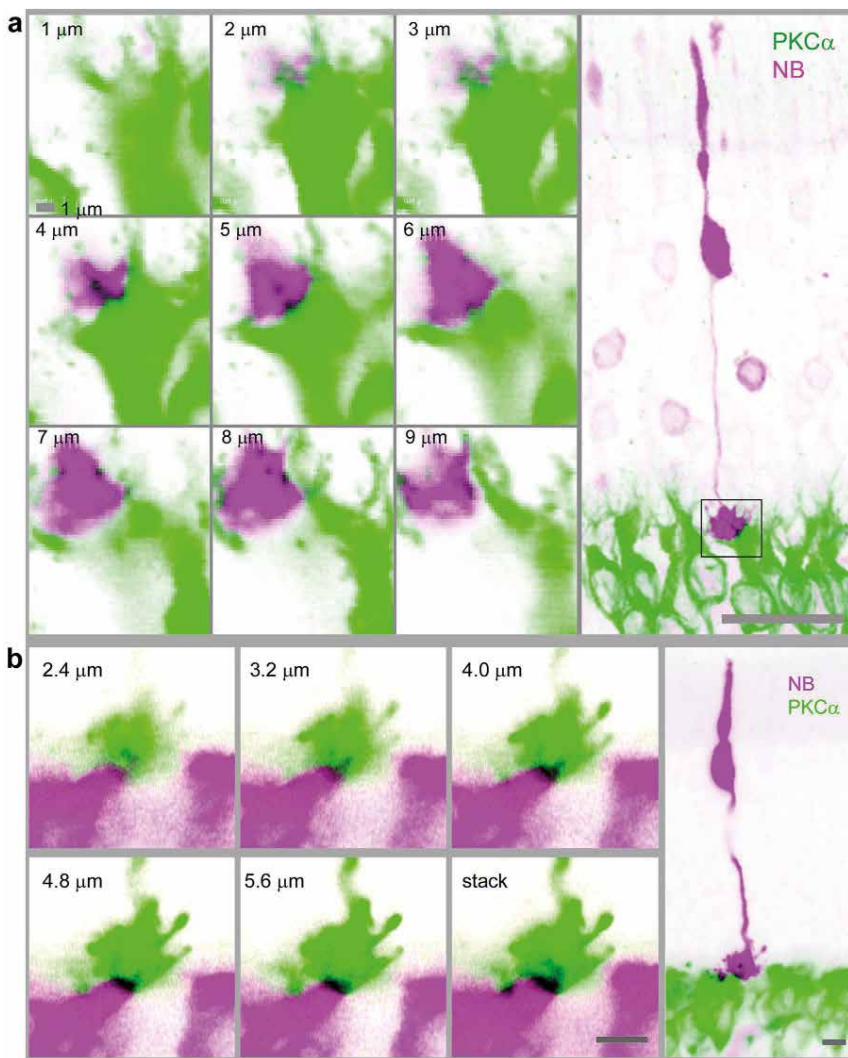


Fig. 1.: Cone-RBC synapses in the mouse retina. Cones were filled with NB (pink) in living retinas and further stained for PKC α (green). Cones possess a triangular shaped pedicle and a large soma close to its thicker inner segment (right panels). Confocal optical sections crossing cone pedicles (square region in right images) are depicted in left panels, which reveal a RBC dendrite invaginating into the center of cone pedicles (in black, in 4–5 μm (a) and 2.4–4.8 μm (b) focal planes). Consecutive confocal optical sections reveal one invaginating (a, b) and a few superficial contacts (a, in 6–8 μm focal planes) (in black) between a cone pedicle and RBCs. Scale bars are 20 μm in a (left) and 5 μm in (b).

contacts are present in 30% of mouse RBCs and in nearly 10% of primate RBCs. Such RBCs could make 0–1 invaginating contact with cones. The single RBC invaginating contact in cones was comparable with that in rods revealed in both this study (Fig. 2 and 3) and others' reports. In addition, the authors results show that RBCs primarily make superficial contacts with cones. Based on cone signals recorded from DBCR2 in the mouse retina and cone-RBC contacts revealed in this and other studies, Pang et al. speculate that cone-RBC synapses have physiological impact in mammalian retinas.

In the primate retina, here it has been observed that some PKC α -positive bipolar cells received both rod and cone synapses, demonstrating the presence of RBC-cone contacts. Although DB4 cells are positive for PKC α , they are known not to receive rod inputs. RBCs are intensively PKC α -positive, while DB4 cells are weakly PKC α -positive, especially the soma and dendrites. Meanwhile, many DB4 cells, or all of them in some

experimental conditions, are not stained for PKC α . This study chose retinas without the PKC α -band in the center of the IPL. And the authors encountered more superficial contacts between PKC α -positive dendrites and cones, while a great majority of DB4 cells makes invaginating synapses with cones. Therefore, Pang et al. believe that RBC-cone contacts that we identified are not DB4-cone contacts.

Retinal second-order neurons can receive rod-cone mixed inputs

Primate retinas possess a higher cone : rod ratio, while nocturnal animals like mice have a lower cone : rod ratio. And rabbit retinas show a higher cone bipolar cell : RBC ratio (3–4 : 1), but the ratio is lower in the mouse retina (2.6 : 1). Whether the relatively large RBC pool in the mouse retina has more complex functions is still unclear. OFF bipolar cells in the mammalian retina

had been previously understood as typical cone bipolar cells because only RBCs were known to be driven by rods. However, in the recent two decades, both anatomical and physiological evidence has emerged, confirming rod inputs to OFF bipolar cells. In mouse retinas, nearly four anatomical subtypes (type 1, 2, 3a, 3b, and 4) and three physiological subtypes (HBCR/MC, HBCM/C, HBCM/SC) of OFF BCs have been identified, based on their axon terminal morphology, immunoreactivity, and location in the IPL, and waveform and sensitivity of their light responses. Both type 3a and 3b OFF BCs form flat contacts at cone pedicles and rod spherules. And some calsenilin-positive dendrites from type 4 OFF BCs contact rods, as well. Dendrites of DB3b OFF BCs made contact with both rods and cones at the photoreceptor basal surface in the macaque retina. The current finding, along with previous anatomical and physiological data together, consistently indicate that mammalian retinal second-order neurons can receive rod-

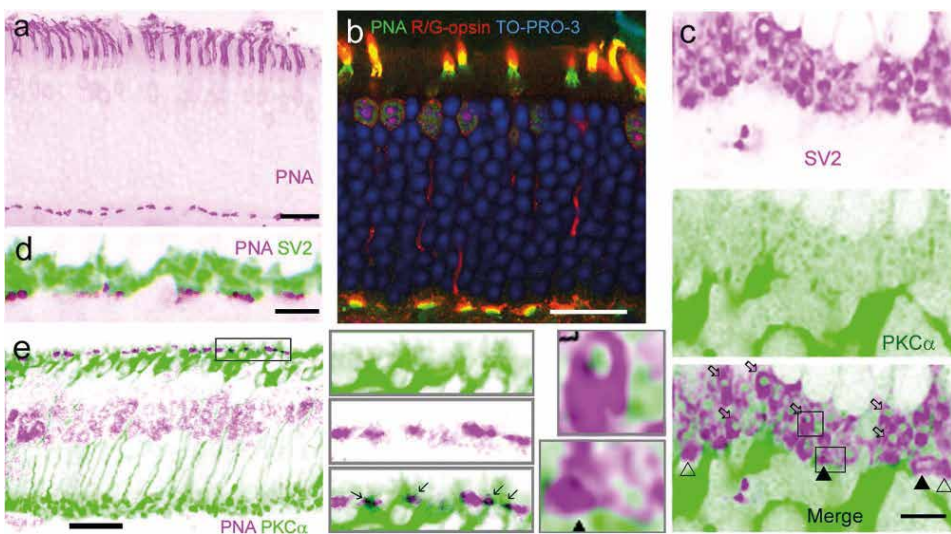


Fig. 2.: Identification of mouse cone-RBC synapses. PNA brightly labels the inner segment (a, b) and the basal membrane of cone pedicles, and cones are labeled for R/G-opsin (b). Nuclei in the outer nuclear layer (ONL) are labeled by nuclear dye TO-PRO-3 (b). Cone somas are mostly located in the first row of somas in the ONL. Cone synapses at the basal membrane, where PNA (b) and

SV2 (c, d) coincide, are closer to RBC layer than all other synapses identified by SV2 in the OPL. Some PKC α -labeled RBC dendrites are colocalized with PNA in cone basal membranes (in black, in e and insets). In retinas labeled for SV2 (c and insets), rod spherules are identifiable by their strong SV2- immunoreactivity, smaller size, oval shape and more distal location (open arrows), while cone pedi-

cles are recognizable by their triangular shape, larger size and more proximal location (triangles). Many Rod-RBC contacts are formed by a solitary RBC dendrite invaginating to the center of each rod spherule, appearing like pomegranate arils (c, bottom). Some cone pedicles receive RBC invaginating contacts (closed triangles) and some don't (open triangles) (c). Scale bars are 20 μ m.

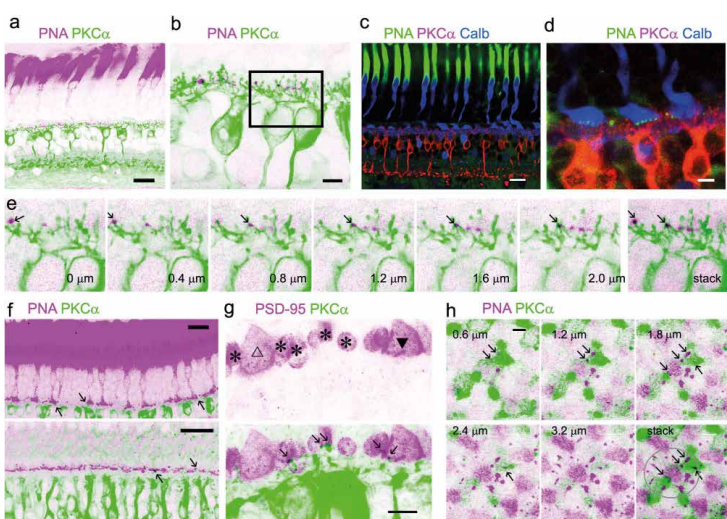


Fig. 3.: Baboon cone-RBC synapses. Retina preparations are triple- (a to d) or double-labeled. Cone somas and pedicles are brightly labeled for calbindin D-28k (Calb) (c, d). PNA intensively labels cone inner segments (a, c, e) and reveals clusters of puncta in the basal membrane of cone pedicles (d). Each cluster of PNA-positive puncta belongs to a cone pedicle (d). Consecutive confocal optical sections of a cone pedicle and its

a rectangular region in b show that some PKC α -labeled RBC dendrites colocalize with PNA (e). Some RBC dendrites coincide with PNA in cone pedicles (see arrows) in retinal slices (f, upper-peripheral retina, lower-para-central retina) and cone telodendrites in the flat-mount retina (h). Panel (h) displays overexposed images of consecutive horizontal confocal optical sections of a cone pedicle and its

telodendrites (in the circle). In retinal slices (g) large triangular cone pedicles are positively labeled for PSD95 (triangle) and distinguishable from small oval-shaped rod spherules (asterisks). RBC dendrites contact rod spherules and one cone pedicle (closed triangle) but do not contact the other cone pedicle (open triangle). Scale bars are 20 μ m in (a), (c), and (f) and 5 μ m in the rest images.

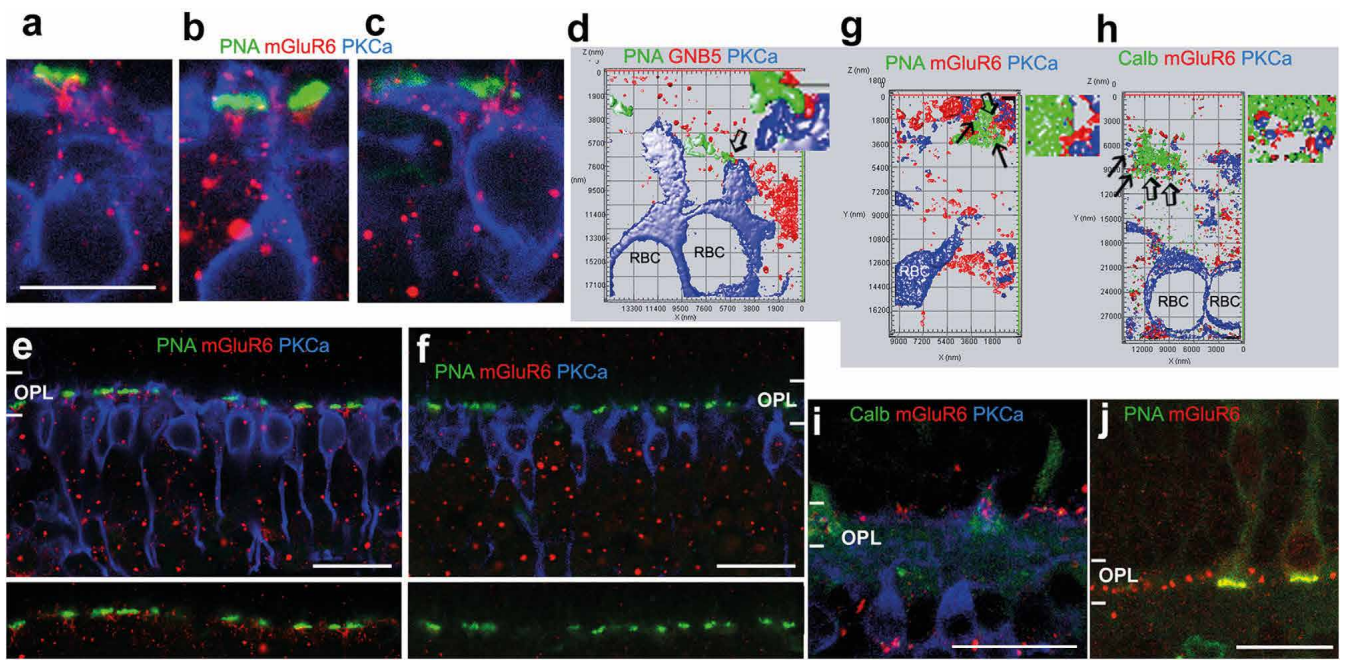


Fig. 4.: GNB5 and mGluR6 expressed in the contacts between cones and RBCs. Mouse (a–f) and baboon (g–j) retinal slices were double- or tripled-labeled. Synaptic contacts were studied in 1–2- μ m-thick blocks with a resolution of 30 nm per pixel (d, g, and h) and in series of optical sections 1 μ m-thick (a–c, e, and f). Panels (d), (g), and (h) display the 3D surface profile reconstructed

from a series of optical sections with a step of 150–180 nm. GNB5 and mGluR6 (red) are present in contacts (arrow) formed by PKCa-labeled RBC dendrites (blue) and PNA or calbin-din (Calb)-labeled cone pedicles (green) (a–d, g, and h). Goat anti-mGluR6 (g, h, and i) and rabbit anti-mGluR6 (the rest images) label primarily the outer plexiform layer (OPL) in the monkey retina (g to j). In the mouse retina, they label the

OPL and inner nuclear layer (e), but the immunoreactivity in the OPL is absent in the mGluR6 knockout mouse (f). The distribution of GNB5 immunoreactivity in the OPL is like mGluR6 immunoreactivity (d). Small regions pointed by open arrows in (d), (g), and (h) are amplified and depicted to the right. GNB5-G protein beta 5. The scale bar is 10 μ m for (a–c) and 20 μ m for (e), (f), (i), and (j).

cone mixed inputs. Therefore, mammalian retinal second-order neurons may pass both segregated rod and cone signals and integrated rod and cone signals to retinal third order neurons.

In mesopic conditions, rods become saturated and cones are barely activated. Since rod/cone-driven RBCs integrate rod and cone inputs, they appear to be able to mediate mammalian mesopic vision, enabling smooth mode-shifting between night vision and photopic vision. In the mammalian retina, ON ganglion cells receive rod signals mainly from the primary rod pathway via cone bipolar cell chemical synapses, because mammalian RBCs do not directly contact ON ganglion cells. Only recently were some mammalian cone ON bipolar cells found to receive mixed rod-cone inputs. All amacrine cells have been identified as a critical mediator for the primary rod pathway. These cells form electric contacts with cone bipolar cells and receive chemical synapses from RBCs at the same time, integrating cone and rod signals before they reach ON gan-

glion cells. In this article, our data suggest that, like all amacrine cells, some RBCs could integrate rod and cone signals, sharing the duty of shaping rod and cone inputs in ON ganglion cells.

Summary

In this study, Pang et al. identified mammalian rod bipolar cells (RBCs), rod and cone photoreceptors and photoreceptor synapses. It was found that RBCs received both superficial and invaginating synapses from cone pedicles. Up to half of the RBCs and cones contacted each other in the retina of mice. Studies of the baboon retina also showed a participation of nearly 10% of RBCs and 20% of cones in cone RBC contacts. Finally, it was shown that mGluR6 and the G protein subunit beta 5 (GNB5) are expressed at the contact sites between cone pedicles and PKC α -labeled RBC dendrites (Fig. 4).

Digest of

Pang J-J, Yang Z, Jacoby RA, Wu SM; Cone synapses in mammalian retinal rod bipolar cells; *The Journal of Comparative Neurology* 2018; 00:1–14.
© 2018 Wiley Periodicals, Inc.
<https://doi.org/10.1002/cne.24456>

Regional differences in Purkinje cell morphology in the cerebellar vermis of male mice

Nedelescu H, Abdelhack M, Pritchard AT

Regional differences in dendritic architecture can influence connectivity and dendritic signal integration, with possible consequences for neuronal computation. In the cerebellum, analyses of Purkinje cells (PCs), which are functionally critical as they provide the sole output of the cerebellar cortex, have suggested that the cerebellar cortex is not uniform in structure as traditionally assumed. However, the limitations of traditional staining methods and microscopy capabilities have presented difficulties in investigating possible local variations in PC morphology. To answer this question, male mice that selectively express green fluorescent protein in PCs were used in this study. Using Neurolucida 360 with confocal image stacks, the authors reconstructed dendritic arbors of PCs residing in lobule V (anterior) and lobule IX (posterior) of the vermis. Subsequently, the morphologies of the individual arbors and the structure of the assembled “jungle” were analyzed and these features were compared across anatomical positions and age groups. Strikingly, here it was found that in lobule IX, half of the reconstructed PCs had two primary dendrites emanating from their soma, whereas fewer than a quarter showed this characteristic in lobule V. Furthermore, PCs in lobule V showed more efficient spatial occupancy compared to lobule IX, as well as greater packing density and increased arbor overlap in the adult. When analyzing complete ensembles of PC arbors, it was also observed “hot spots” of increased dendritic density in lobule V, whereas lobule IX showed a more homogeneous spread of dendrites. These differences suggest that input patterns and/or physiology of PCs could likewise differ along the vermis, with possible implications for cerebellar function.

Using a Zeiss LSM 880 Airyscan, 40x objective, NA 1.4, two different locations in the cerebellar cortex: the bank region (the straight portion of the sagittally sectioned lobule) of lobule V (anterior) and lobule IX (posterior) could be imaged. The entire 80- μm thickness of the sagittally sectioned tissue was captured at a 0.25- μm step size in the z-direction, which ensured unambiguous resolution of neighboring dendrites (Fig. 1). In order to image multiple neighboring PCs and capture their wide (100–200 μm) dendritic arbors, it was necessary to acquire multiple adjacent “tiles” at each location (Fig. 1a). The x, y dimensions of each tile were 225 μm x 225 μm , and adjacent tiles overlapped by 10%. This 10% overlap was chosen because it was found to be the minimum amount of overlap necessary for proper alignment and stitching of the resulting adjacent images. This acquisition protocol enabled Nedelescu et al. to obtain the complete morphology of approximately 3–4 adjacent PC arbors in the sagittal direction and 3–4 adjacent arbors in the medio-lateral direction (Figure 1b).

Lobule-dependent growth of Purkinje cell arbors

Sholl analysis indicated that the number of dendritic branch points increased between “young” (P12–15) and “adult” stages (P30–60), consistent with previous investigations. However, significant change only occurred in lobule V, not lobule IX (Fig. 2), perhaps because lobule IX PCs had already attained their mature morphology by P12–15. This is consistent with evidence that different cerebellar lobules follow different developmental time-courses. In one study in rat, the first PCs to grow primary dendrites were in lobule IX, whereas lobule V PCs developed their primary dendrites later; furthermore, climbing fiber inputs to PCs develop earlier in lobule IXa-b compared to lobule V.

Despite these lobular differences in the development of PC arbors, there were no significant differences in the mean number of Sholl intersections between lobule V and lobule IX within either of the two age groups, when considered separately. This suggests that although lobule IX matures earlier than lobule V, PCs in these two lobules have a similar branching complexity once both lobules have reached maturity.

Two morphologically distinct Purkinje cell subtypes

Although the Sholl analysis suggested that PCs had a similar degree of complexity in lobules V and IX, the authors did observe qualitative differences in dendritic branching patterns between these two locations. They do not consider this contradictory, since the Sholl analysis only considers the number of dendritic branching points; in principle, two arbors could have the same number of branch points, but very different geometric shapes. In the presented data, such differences were sufficiently striking that they warranted classification of PCs into subtypes (Fig. 3). Type 1 PCs conformed to the classic model of a PC, with a single primary dendrite and fairly homogeneous density of branches throughout the thickness of the molecular layer. Conversely, Type 2 PCs had two primary dendrites, and relatively little branching in the lower portion of their arbors. These distinct arbor descriptions were first observed in 1967 and later quantified, revealing that Type 1 PCs were predominantly located in the apex of the lobule, while Type 2 were generally found in the sulcus between lobules. Interestingly,

the sulcus develops prior to the apex, just as lobule IX develops prior to lobule V. This could indicate a relationship between maturation time and resulting PC morphology, whereby early maturation would increase the likelihood of Type 2 morphology.

Dendritic branch points can have important consequences for the propagation of signals within a neuron; differences in dendritic arbor morphology could therefore influence how PCs integrate synaptic input. In particular, dendritic branches act to compartmentalize the cell by limiting signal propagation between dendritic sectors; the presence of two primary dendrites could therefore influence the integration of parallel fiber input within PCs. Given that 67% of lobule IX PCs had two primary dendrites in the present study, this could in turn affect the neuronal computations occurring in this region.

Arbor overlap and spatial occupancy

When Nedelec et al. quantified the overlap of adjacent pairs of PC arbors, they found significantly greater overlap in lobule V compared with lobule IX. However, this increased overlap was only apparent in adult mice, which is consistent with the comparatively late development of PCs in lobule V (supported by the Sholl analysis). Furthermore, the hull/convex hull ratio analysis revealed that arbors in lobule V occupied their surrounding space more efficiently than those in lobule IX, which may have been due to a greater overall surface area of lobule V arbors in the adult (hull) without a corresponding increase in occupied space (convex hull).

Both phenomena may be a direct result of arbor geometry, and specifically the prevalence of Type 1 arbors in lobule V. Increased overlap and spatial efficiency could also relate to the higher density of PCs in lobule V compared with lobule IX of adult mice, which the authors observed when counting Type 1 and Type 2 PCs directly in the confocal image stacks: within the 300 µm sampled span within the sagittal plane, they counted 143 PCs in lobule V of adult mice (in total, across three animals) versus 89 PCs in adult lobule IX. Previous investigations have also noted regional differences in PC packing density, which included a higher density of somata in the anterior lobe of rats compared with the posterior lobe. These studies add to these findings, by examining the consequences of anatomical location for the spatial relationships of adjacent arbors. However, it is notable that despite lower packing density in lobule IX, no evidence has been found that arbors in lobule IX had a

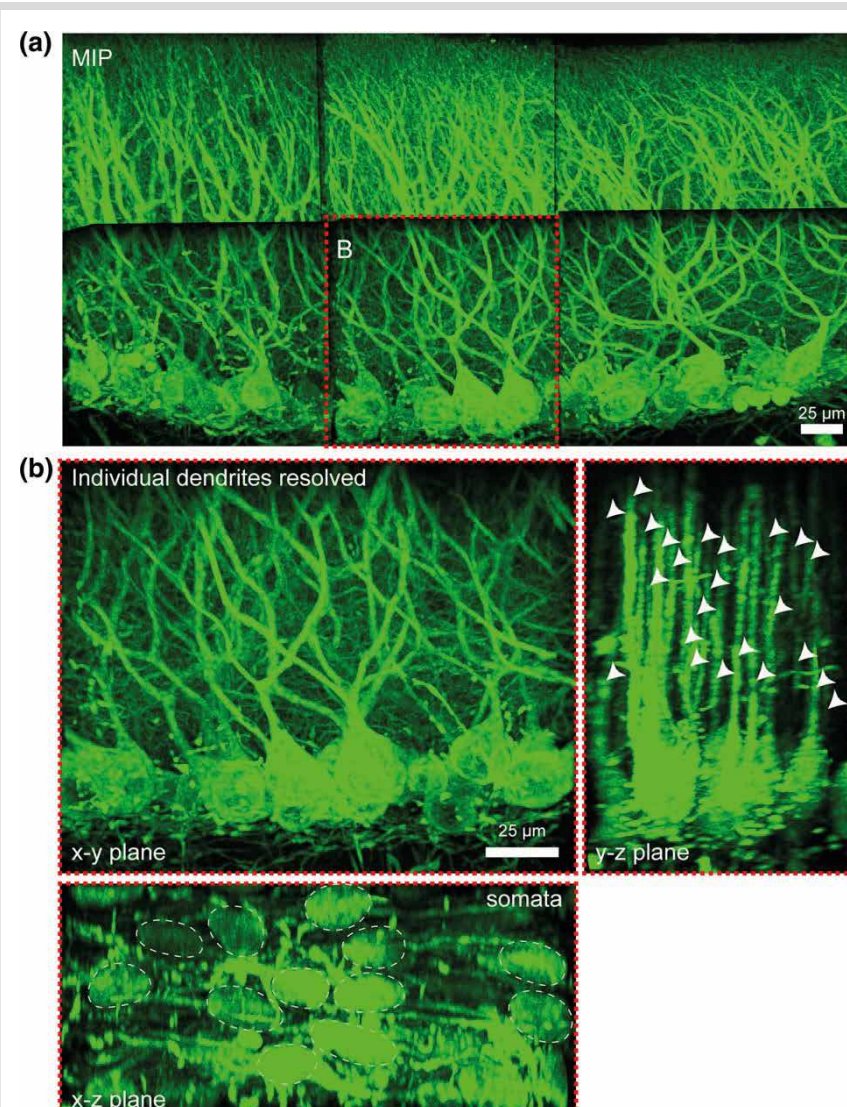


Fig. 1.: High-resolution images resolves individual neighboring dendrites and somata. Panel A sagittal view of a representative sample acquired in tiles showing the intricate PC dendritic “jungle.” **Panel B** is a larger view of the inset in

Panel A showing the following planes: x-y, y-z with neighboring individual dendrites resolved (arrow heads) and x-z with neighboring individual somata resolved (dotted contours) in three-dimensional space of the imaged stack.

greater surface area (hull) or even occupied a greater volume of space (convex hull) in lobule IX relative to lobule V. Indeed, lobule V arbors had a greater mean hull relative to lobule IX in adult mice.

The extent to which arbor geometry influences dendritic overlap could be investigated by comparing adjacent pairs of PCs, according to the cell sub-types of which they are composed. However, such comparisons among cell types could be valuable in future research, to quantify the impact of single-cell morphology on the structure of local PC ensembles.

As a consequence of arbor overlap, it is possible that adjacent PCs could share

parallel fiber input. If this is the case, then neighboring PCs in lobule V could have more closely related computational roles than those in lobule IX. However, this would depend on other features of the local neuronal network in which PCs are embedded. For example, would neighboring, overlapping PCs share input from the same parallel fibers? Or alternatively, if overlap is a functionally neutral side effect of higher packing density, do parallel fibers compensate for this feature by only contacting some PCs and ‘missing’ their immediate neighbors? These scenarios could be investigated by comparing parallel fiber terminals across lobules.

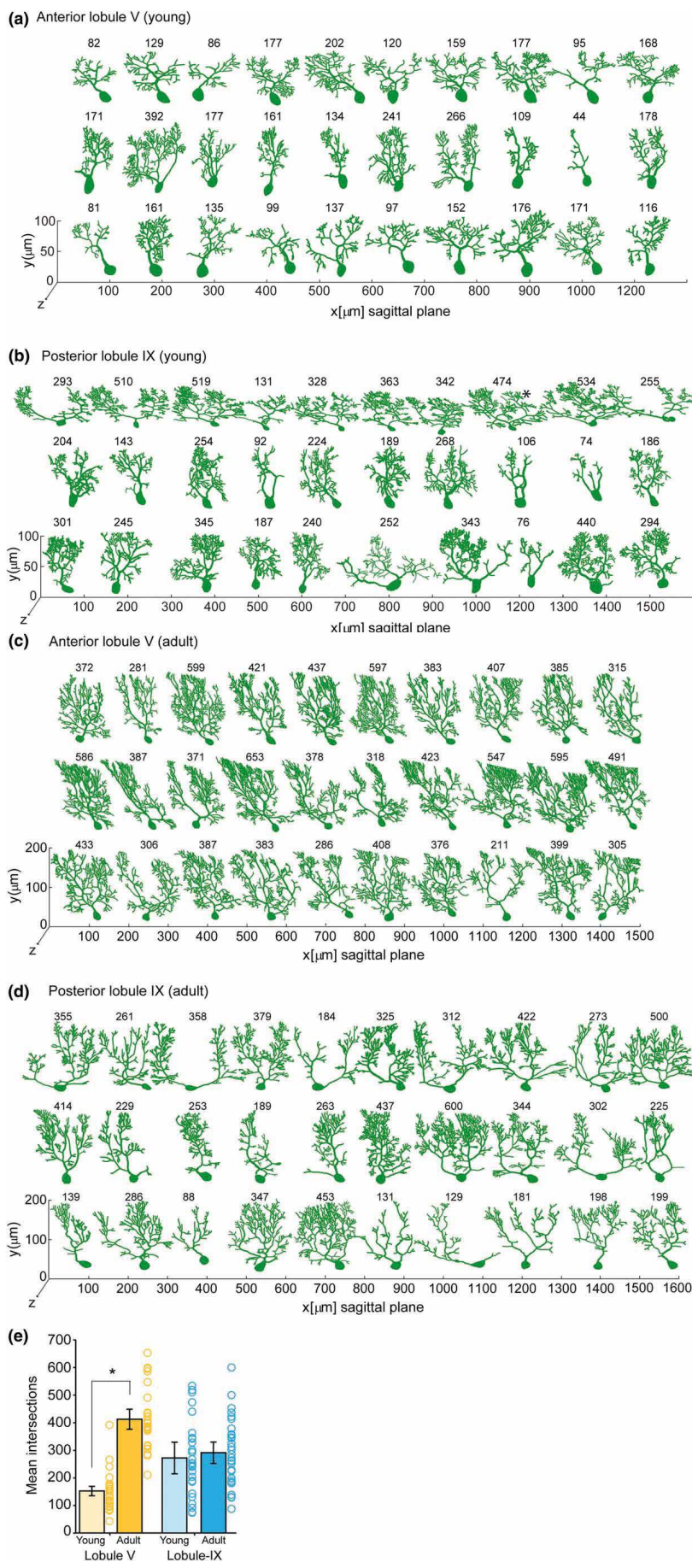


Fig. 2.: Reconstructed dendritic arbors of neighboring Purkinje cells. Panels A, B show morphologies of neighboring PC dendritic arbors reconstructed in lobule V (Panel A) and lobule IX (Panel B) of young mice. Panels C, D show corresponding reconstructions of adult arbors. Each Purkinje cell row depicts reconstructions of ten neighboring cells from one mouse, giving a total of thirty Purkinje cells for each age and anatomical region. The y-axis provides a scale for arbor height and the x-axis provides a scale for arbor width in micrometers. Arbors are viewed in the parasagittal plane. The number above each cell indicates the number of intersections from the Sholl analysis, which is counted as the number of times that dendritic processes intersect the concentric circles of the Sholl method. Panel E summarizes the mean number of intersections from each animal group, highlighting the statistical difference (asterisks) in average intersections between young and adult PCs located in the anterior lobe. N = 3 adult animals and n = 30 reconstructed PCs per anatomical region (n = 10 cells per animal for a total of 60 reconstructed young morphologies).

"Hot spots" of increased dendritic density

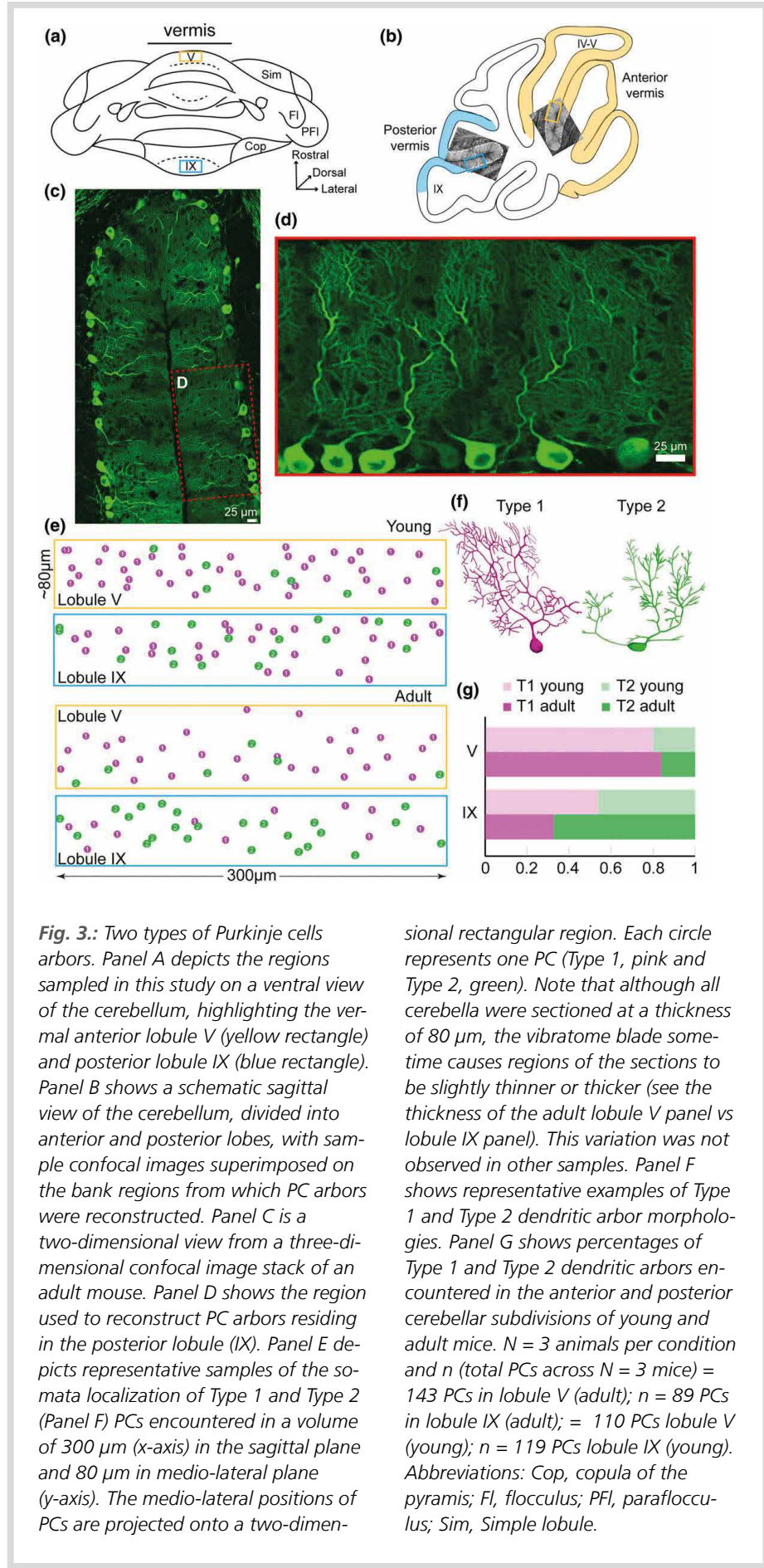
As well as studying PC dendrites on an individual basis and as neighboring cell pairs, the authors created heat maps of dendritic overlap covering the entire reconstructed subset of the PC populations in lobules V and IX. This local population-level view was consistent with their finding that PC arbors overlap with their neighbors in lobule V more than in lobule IX, particularly in the adult (Fig. 4c,e). To their surprise, they also noticed regions of increased dendritic density or "hot spots" in lobule V of adult mice, whereas the dendritic network pattern in lobule IX was more homogeneous (Fig. 4d,e).

These hot spots may result from the greater prevalence of Type 1 morphology in lobule V, compared with lobule IX. The geometry of Type 1 arbors, with their homogeneous density of dendrites, could directly lead to a more heterogeneous multicellular environment featuring not only greater general overlap, but also hot spots. Conversely, the more widely spread-out dendritic compartments of Type 2 arbors could result in a more homogeneous molecular layer with less overlap.

Since PC dendritic branches are studded with spines, the observed hot spots in lobule V are likely local clusters of dendrites, which receive parallel fiber input. Local spatial variability in input could have major effects on PC signal processing: two-photon imaging *in vivo* has revealed clustered firing of neighboring parallel fibers in mice in response to sensory processing. Interestingly, such parallel fiber clusters did not necessarily arise from the same locations in the granule cell layer, suggesting that PC arbors receive a powerful overview of distributed mossy fiber input.

Summary

In two regions of the murine vermis, each with different connectivity and maturation times, Nedelec et al. identified differences in arbor morphology and in the structure of the assembled Purkinje cell "jungle." Their investigation focused on one anterior and one posterior site in the vermis. However, one should be cautious about generalizing their findings to the entire anterior or posterior lobe. Although the division into lobes by the primary fissure is a conspicuous anatomical feature, the vermis can be subdivided in several ways, and so factors other than the anterior/posterior distinction—such as maturation time, mossy fiber input, climbing fiber input, or zebrin expression—may be



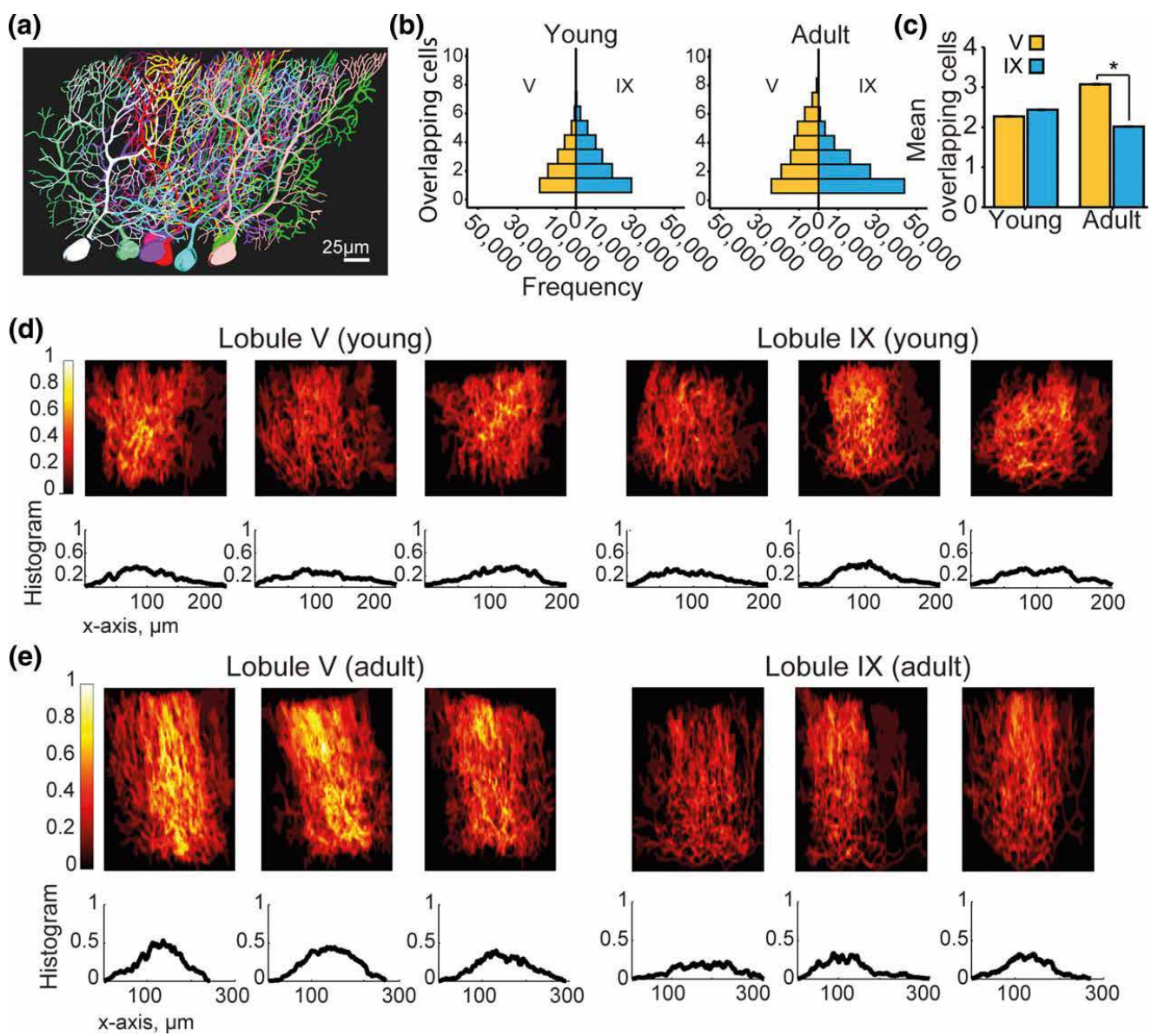


Fig. 4.: Local ensembles of Purkinje arbors reveal dendritic hot spots in the anterior lobe. Panel A shows a sample of ten reconstructed neighboring PCs used for local dendritic network analysis. Panel B histograms showing the frequency with which PC arbors overlapped with one or more neighboring cells (y-axis) in each anatomical region for young and adult. Panel C is a sum-

mary of the mean dendritic overlap in each sample of ten PCs. Panels D and E, heat maps for each reconstructed dendritic network spatially revealing regions of increased dendritic density. The trace in the histograms in Panels D, E shows how dendritic density increases and decreases sharply, which corresponds to regions of high and low arbor overlap within each dendritic network above. Note the ampli-

tude of the histogram is most pronounced in lobule V of adult mice. The x-axis is distance in micrometers for each neuronal ensemble and the y-axis is intensity of overlap. Each animal is represented by a heat map. $N = 3$ animals per condition and $n = 10$ PCs per animal. Abbreviations: V, vermis lobule V; IX 5 vermis lobule IX.

relevant. Another open question concerns the borders between different longitudinal or genoarchitectural regions, and the possible functional implications of PC dendritic overlap in such locations. Finally, it remains to be seen how PC morphology in the cerebellar hemispheres compares with the present findings in the vermis.

Digest of
Nedelescu H, Abdelhack M, Pritchard AT;
Regional differences in Purkinje cell morphology
in the cerebellar vermis of male mice;
Journal of Neuroscience Research 2018;
96:1476–1489
© 2018 Wiley Periodicals, Inc.
<https://doi.org/10.1002/jnr.24206>

Characterization of perinatally born glutamatergic neurons of the mouse olfactory bulb based on NeuroD6 expression reveals their resistance to sensory deprivation

Angelova A, Platel J-C, Béclin C, et al.

During postnatal olfactory bulb (OB) neurogenesis, predetermined stem cells residing in the ventricular–subventricular zone (V-SVZ) continuously generate progenitors that migrate in the rostral migratory stream (RMS) and integrate into the OB. Although the vast majority of these postnatally generated interneurons are inhibitory, a sub-fraction represents glutamatergic neurons that integrate into the superficial glomerular layer (GL). It has been demonstrated that the bHLH transcription factor NeuroD6 is specifically and transiently expressed in the dorsal neurogenic lineage that generates glutamatergic juxtaglomerular cells (JGCs) for the OB. Using lineage tracing combined with whole brain clearing, the authors provide new insight into timing of generation, morphology, and connectivity of glutamatergic JGCs. Specifically, it has been shown that all glutamatergic JGCs send complex axons with varying projection patterns into different layers of the OB. Moreover, Angelova et al. announced that, contrary to GABAergic OB interneurons, glutamatergic JGCs survive under sensory deprivation, indicating that inhibitory and excitatory populations are differentially susceptible to environmental stimulation.

The bHLH transcription factor NeuroD6 represents a novel and reliable marker for glutamatergic neurons in the OB. We therefore exploited ND6Cre and ND6CreERT2 mice as genetic tools to study this elusive cell population. It has been found that ND6 expression in the V-SVZ-RMS-OB system is transient and confined to immature progenitors. Induction of ND6CreERT2 labels therefore a well-defined and timed cohort (Fig. 1). The authors demonstrated that glutamatergic JGCs are not only heterogeneous in dendritic arborization (Fig. 2) but also in axonal projection patterns (Fig. 3). Finally, it could be shown that other than inhibitory JGCs, glutamatergic JGCs resist sensory deprivation.

Whole tissue 3-D images were obtained using the Zeiss Lightsheet Z.1 microscope. Immunohistochemistry Analysis was performed with Zeiss LSM 780 and LSM 880 laser scanning confocal microscopy and *in vivo* and cleared brain studies were observed with the Zeiss 7MP two-photon microscope.

ND6 expression is transient and confined to glutamatergic OB progenitors

ND6 expression has been described for a multitude of brain areas including the neocortex, hippocampus, as well as some mid- and hindbrain structures. Interestingly, although studies that have investigated ND6 expression in detail agree upon the fact that promoter activity starts at the level of post-mitotic progenitors, expression maintenance varies greatly according to brain area and possibly protein function. Using a battery of markers in the V-SVZ Angelova et al. found no co-localization of tdTom with the stem cell marker Pax6, rare co-localization with intermediate progenitor marker Ki67, and full overlap with post-mitotic marker Tbr1. This indicates that also in the postnatal V-SVZ, ND6 is expressed in post-mitotic progenitors. These results are further corroborated by the observations from lineage tracing experiments with ND6CreERT2/tdTom mice in which a defined cohort of recombinant neurons was obtained after tamoxifen (TAM) induction (Fig. 1). Moreover, the lack of recombined cells within the VZ with radial glia-like or ependymal cell morphol-

ogy argues against the possibility that ND6 is expressed in retinal ganglion cells (RGCs) at their last round of division before becoming ependymal cells. Finally, the absence of fluorescent neurons within the GL at 1 day post induction (dpi) (Fig. 1b) indicates that ND6 promoter is not active once neuroblasts reached their target layer. Altogether, these data show that ND6 is transiently expressed starting from post-mitotic progenitors and stopping before final neuronal integration.

Glutamatergic JGCs are morphologically heterogeneous and project axons across the OB

The OB is dominated by inhibitory transmission, with the vast majority of neurons being GABAergic. However, locally connecting excitatory OB neurons like short axon cells and external tufted (ETCs) and bi-tufted cells constitute an important part of the OB circuitry. With the emergence of lineage tracing in mouse mutants, previous studies have shown that these JGCs are also produced postnatally and to a lesser extent even in adult. In agreement, the authors showed that external tufted, bi-tufted cells and to

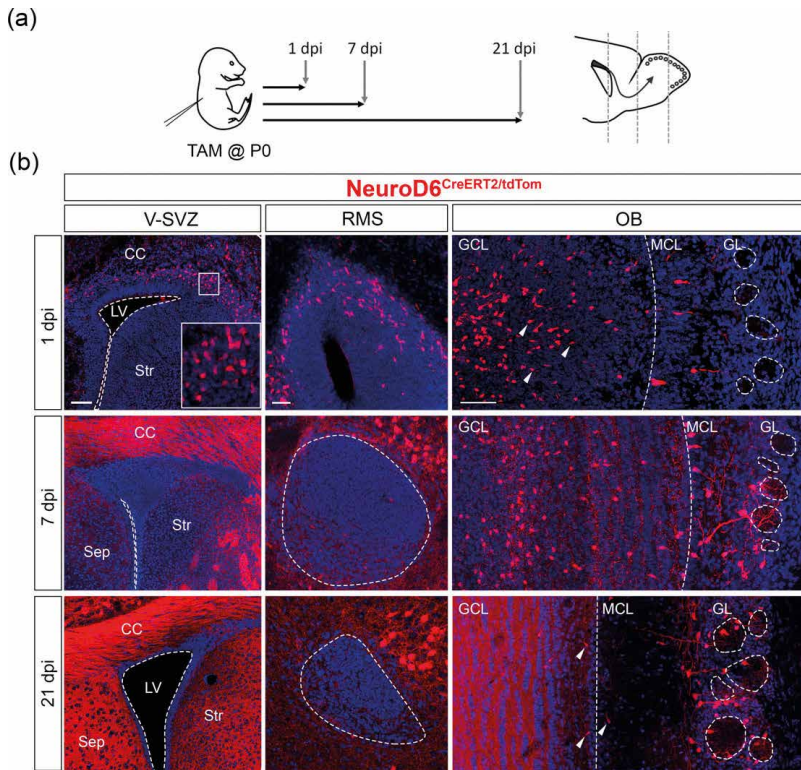


Fig. 1.: TAM induction in neonatal ND-6^{CreERT2} mice recombines neuronal progenitors along the V-SVZ-RMS-OB axis. (a) Schematic representation of TAM-induced pulse-chase experiments. Pups were induced at P0 and brains were harvested 1, 7, and 21 days post induction (dpi), respectively. Dotted lines on sagittal representation indicate the level of slice analysis from V-SVZ to OB. (b) The presence of recombined red cells along the V-SVZ-RMS-OB axis at different time points after TAM induction. At 1 dpi, neuronal progenitors are found in the dorsal V-SVZ, in the RMS and in the deeper OB layers. Most cells display a migratory morphology (arrow head). At 7 dpi, recombined cells are found mainly within the OB. Cells with more complex morphology start to appear in the GL. At 21 dpi, cells are found almost exclusively within the GL and have acquired a mature neuronal morphology. Some cells are found close to the mitral cell layer (MCL, arrow head). RMS, rostral migratory stream. Scale bars: left to right: 100 μ m, 40 μ m, 100 μ m.

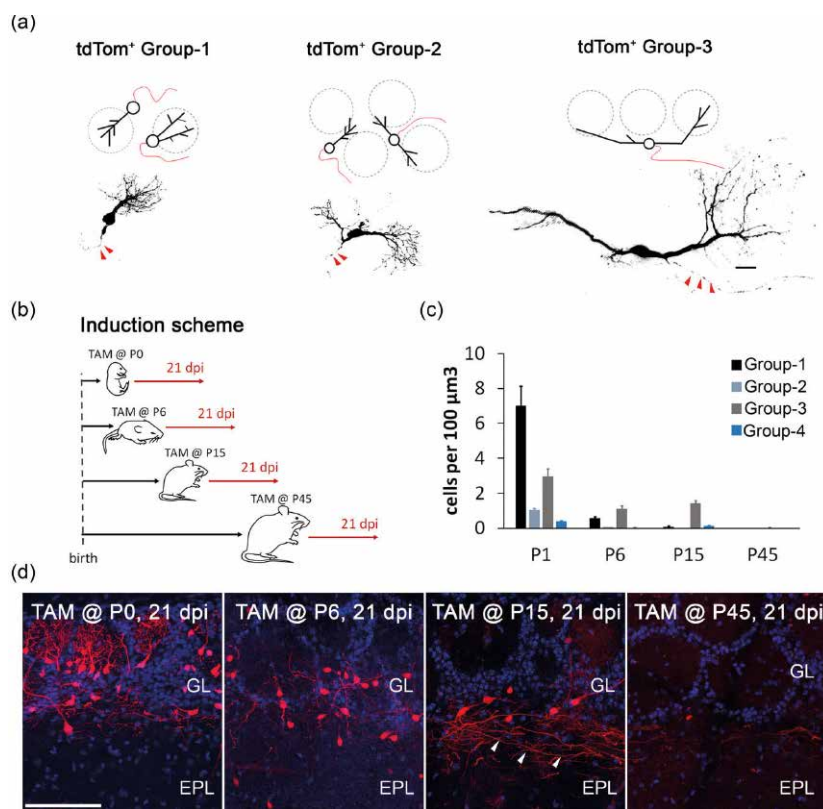


Fig. 2.: Glutamatergic juxtaglomerular cells (JGCs) are morphologically heterogeneous and can be classified into three main groups. (a) Schematic representation (above) and real examples (below) of three main neuron groups based on their dendritic branching pattern into one glomerulus (Group-1), more than one glomerulus (Group-2) or the presence of an additional secondary dendrite extending into the EPL (Group-3). All categories display a fine protrusion, resembling an axon (indicated in red on scheme and with red arrows on real cells). (b) Schematic representation of induction protocol used in (c) and (d). ND6^{CreERT2}/tdTom mice are induced with TAM at P0, P6, P15, and P45, respectively, and brains collected 21 dpi. (c) Quantification of categories of recombined glutamatergic JGCs when induction is performed at different time points. Note that a fourth group, short axon cells (SAC), is also detected. However, given that this cell type is seldom observed and that dendritic morphology does not correspond to the classical description, we did not further quantify these cells. (d) Representative confocal images of animals induced at different time points showing enlarged view of the GL and EPL. The amount of recombined red cells declines progressively as induction is performed in older animals. Scale bars: (a) 20 μ m, (d) 100 μ m.

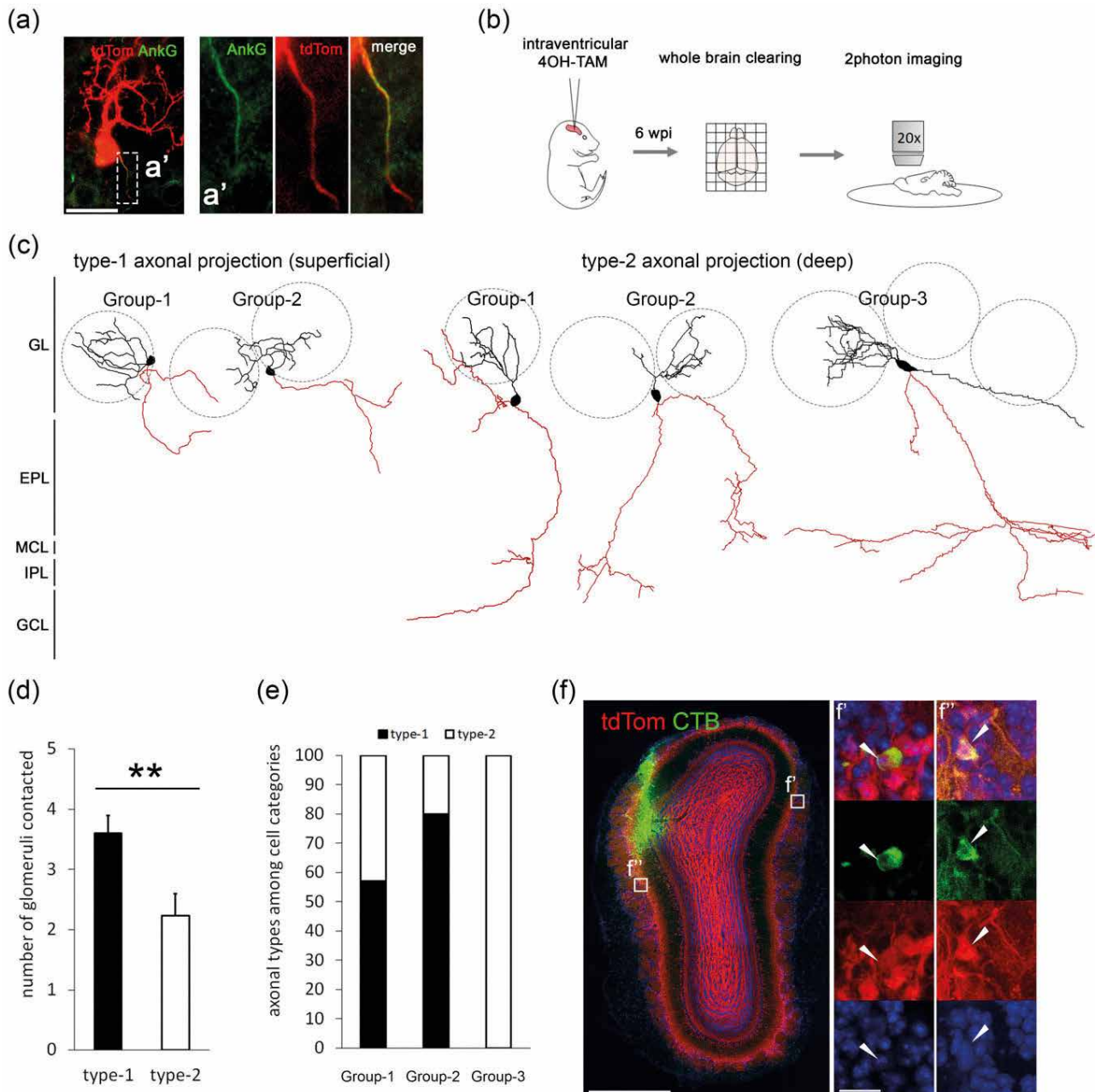


Fig. 3.: Glutamatergic JGCs project axons across all layers of the olfactory bulb.
(a) *tdTom*+ cells display thin protrusions which are immunoreactive for axonal initial segment marker Ankyrin G (*AnkG*). Detail of co-localization shown in (a0).
(b) Schematic representation of experimental setup to induce sparse labeling and follow axonal projections. Intraventricular hydroxytamoxifen (4OH-TAM) injection in neonatal *ND6CreERT2/tdTom* mice. Six weeks post injection (wpi) brains are harvested and cleared using the Cubic protocol. To obtain as complete axonal reconstructions as possible, entire transparent brains were imaged

using two-photon microscopy. **(c)** Partial axonal reconstructions of the different postnatal generated glutamatergic JGCs. Axonal projections (red) either remain within the glomerular layer (type-1 superficial axons) or dive into the GCL (type-2 deep axons) where they cannot be traced anymore due to high density of projections. Deep axons are frequently observed to specifically branch within the inner plexiform layer (IPL). **(d)** Type-1 axons contact significantly more glomeruli than type-2 axons ($p = 0.0098$, $**p < 0.01$, two-tailed Mann Whitney U test, $n(\text{superficial}/\text{deep}) = 25/17$ cells, three animals). **(e)** Relative occurrence of axo-

nal types on glutamatergic JGC categories. Type-1 and type-2 axons appear on external tufted cells (Group-1 and 2). All traced superficial tufted cells (Group-3) displayed type-2 axons ($n(\text{Group-1/2/3}) = 28/10/4$ cells, three animals). **(f)** Retrograde labeling of *tdTom*+ cells (medial) after localized CTB injection (lateral) suggests that type-2 axons connect to the opposite side within the same OB. **(f0)** Double-labeled CTB+ *tdTom*+ cells are systematically found on OB side opposite to the injection site (59 cells, three animals) but also adjacent (**f00**) to the injection site. Scale bars: (a) 20 μ m; (f), 1 mm; (f0) 20 μ m. Error bars indicate SEM.

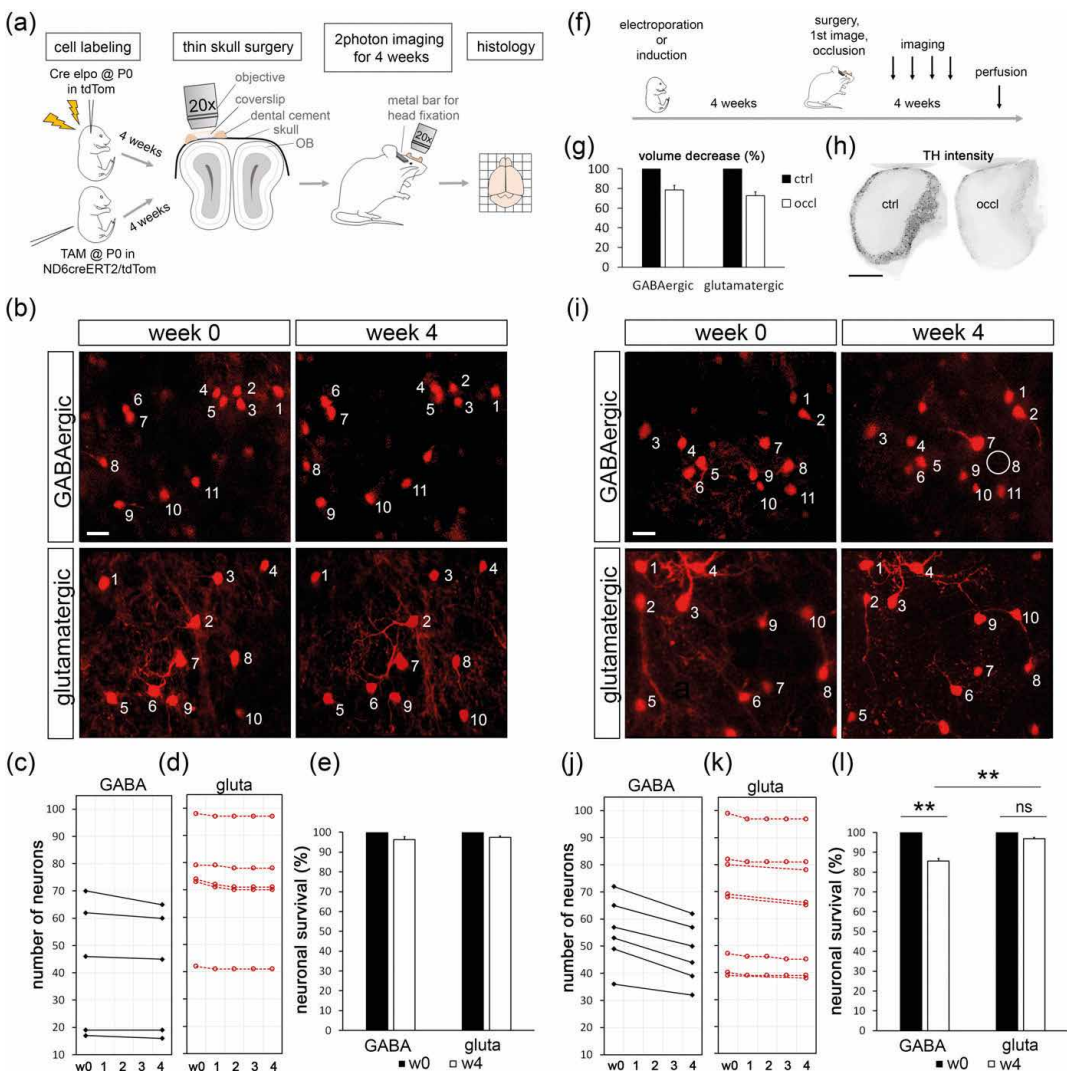


Fig. 4.: Glutamatergic JGCs are resistant to sensory deprivation. (a) Schematic representation of experimental procedure carried out to study *in vivo* survival of glutamatergic and GABAergic cells. To mark GABAergic JGCs, Cre recombinase plasmid was electroporated (*elpo*) into *P0* *tdTom* reporter mice. To mark glutamatergic JGCs *ND6creERT2/tdTom* was induced at *P0*. Four weeks after *elpo* or induction, thin-skull surgery was performed. Mice were imaged for 4 weeks using a two-photon microscope. Their brains were subsequently fixed and processed for histological analysis. (b) Image of the same region for GABAergic cells (above) and glutamatergic JGCs (below), short after *tdTom* recombination (week 0) and 4 weeks later (week 4). Each cell is numbered and identified based on their relative position to other cells and distinctive dendritic branching pattern (whenever possible). (c) Number of GABAergic

JGCs followed in individual animals (black lines) in the course of 4 weeks. (d) Number of glutamatergic neurons followed in individual animals (red lines) in the course of 4 weeks. (e) Percentage of GABA- and glutamatergic JGCs that survived under control condition in the course of 4 weeks as compared to week 0. (f) Schematic representation of experimental setup conducted for sensory deprivation using unilateral naris occlusion. The scheme recapitulates essentially the protocol depicted in (a) with the difference that in a group of animals, unilateral naris occlusion was additionally performed at the moment of the surgery. (g) Loss of approximately 30% of OB volume in occluded (occl) OB as compared to control OB (ctrl). (h) Strong decrease in TH immunoreactivity further confirms successful occlusion. (i) Image before (week 0) and 4 weeks after (week 4) occlusion of the same region for GABAergic cells

(above) and glutamatergic JGCs (below). Note that under occlusion, a fraction of GABAergic cells disappears (circle). (j) Number of GABAergic JGCs followed in individual animals (black lines) during 4 weeks of occlusion. (k) Number of glutamatergic neurons followed in individual animals (red lines) during 4 weeks of occlusion. (l) Percentage of GABA- and glutamatergic JGCs that survived under occlusion in the course of 4 weeks as compared to week 0. Although a significant decrease in GABAergic cell number is observed ($p = 0.00804$ for GABA_{ctrl} vs GABA_{occl}, $p = 0.0018$ for GABA_{occl} vs gluta_{occl}, ** $p < 0.01$, two-tailed Mann Whitney U test, $n_{GABA}(\text{ctrl}/\text{occl}) = 214/279$ cells, 5/6 animals, respectively), glutamatergic cell number remains stable ($n_{Gluta}(\text{ctrl}/\text{occl}) = 365/403$ cells, 5/9 animals, respectively). Scale bars: (b) 20 μ m; (h) 1 mm; (i) 20 μ m. Error bars indicate SEM.

a lesser extend superficial tufted cells are indeed generated at perinatal stages (Fig. 2a). Moreover, laser scanning confocal imaging revealed that the majority of glutamatergic perinatally born JGCs are ETCs and that the overall neuron production drops drastically and rapidly after birth (Fig. 2d).

Using a two-photon-setup after brain clearing (Fig. 3b), evidence of existence has been found of two types of axonal projections in perinatally born JGCs; type-1 projections that remain within the glomerular layer and type-2 projections that contact less glomeruli and dive deep into the core of the OB (Fig. 3c-e). Moreover, retrograde tracing shows that some glutamatergic JGCs project even across the medio-lateral aspects of the OB (Fig. 3f). This finding suggests that type-2 projections belong to the intrabulbar associated system or mirror-symmetric iso-functional odor columns. This intrabulbar circuit typically connects two glomeruli that express the same odorant receptor in a medio-lateral manner and is mediated by ETCs that project through the GCL and synapse with GCs situated just underneath its associated glomerulus on the other side of the OB. However, although there is no experimental evidence for extrabulbar projection, it is likely that part of the type-2 superficial TCs project outside the bulb, particularly in the pars externa of the anterior olfactory nucleus.

Perinatally born glutamatergic JGCs resist sensory deprivation

To investigate the effects of environmental information on glutamatergic JGCs within the OB brain circuit, sensory deprivation by unilateral naris occlusion was applied. There is a well-established body of literature that

shows how olfactory sensory deprivation causes cell death throughout all OB layers thereby emphasizing the importance of sensory input for survival of OB inhibitory interneurons. Here a chronic *in vivo* imaging approach using two-photon Microscopy was performed to directly monitor the survival of a to-date unexplored OB neuron population, glutamatergic JGCs (Fig. 4). In the first imaging session, an individual fluorescently labeled GABAergic and glutamatergic neurons were identified and observed over time in control situation and under occlusion. It was demonstrated that although a significant fraction of GABAergic JGCs disappear, the vast majority of glutamatergic JGCs remain in place under unilateral naris occlusion. Many studies have revealed that a fraction of GABAergic cells undergo cell death under occlusion. But why does this apparently general phenomenon not apply to glutamatergic JGCs? The most obvious difference between these two cell types clearly is reflected in their neurotransmitter phenotype and thus their function in the OB as either excitatory or inhibitory circuit elements. It is intriguing to view the OB system as an intricate homeostatic balance between excitation and inhibition, finely tuned by the environmental challenges imposed to the system. In this scenario, the decreased environmental excitation has to be compensated by an overall decrease in bulbar inhibition, allowing the system to still confer information to higher order brain areas. Because adult neurogenesis provides the OB continuously with inhibitory interneurons, directed apoptosis could be a feasible mechanism to fine-tune inhibitory elements of the OB system. In the meantime, excitatory elements have to adjust their excitability, too. However, given that adult neurogenesis does not supply the OB with a significant num-

ber of glutamatergic neurons at later ages, it seems unlikely that apoptosis could be a regulative mechanism for adjustment of excitation.

Further experiments will be needed to elucidate why cell death occurs selectively to some elements of the OB circuit and not to others. However, these results represent a first step toward a more differentiated view of the OB network where both, local excitation and as well as inhibition are provided and adjusted by the interplay of an intricately complex network with its environment.

Summary

In their characterization of perinatally born glutamatergic neurons of the mouse olfactory bulb (OB) Angelova et al. observed that the basic helix-loop-helix transcription factor NeuronD6 expression is transient and limited to glutamatergic OB precursors. The heterogeneous morphology of glutamatergic JGCs classified in three main groups and their ability to project axons via OB have been described as well as resistance to sensory deprivation of perinatally born glutamatergic JGCs.

Digest of
Angelova A, Platel J-C, Béclin C, Cremer H,
Coré N;
Characterization of perinatally born glutamatergic neurons of the mouse olfactory bulb based on NeuroD6 expression reveals their resistance to sensory deprivation;
Journal of Comparative Neurology 2019;
527:1245–1260.
© 2018 Wiley Periodicals, Inc.
<https://doi.org/10.1002/cne.24621>

Quantification of collagen fiber structure using second harmonic generation imaging and two-dimensional discrete Fourier transform analysis: Application to the human optic nerve head

Pijanka JK, Markov PP, Midgett D, et al.

Second harmonic generation (SHG) microscopy is widely used to image collagen fiber microarchitecture due to its high spatial resolution, optical sectioning capabilities and relatively nondestructive sample preparation. Quantification of SHG images requires sensitive methods to capture fiber alignment. This article presents a two-dimensional discrete Fourier transform (DFT)-based method for collagen fiber structure analysis from SHG images. The method includes integrated periodicity plus smooth image decomposition for correction of DFT edge discontinuity artefact, avoiding the loss of peripheral image data encountered with more commonly used windowing methods. Outputted parameters are as follows: the collagen fiber orientation distribution, aligned collagen content and the degree of collagen fiber dispersion along the principal orientation. The authors demonstrate its application to determine collagen microstructure in the human optic nerve head, showing its capability to accurately capture characteristic structural features including radial fiber alignment in the innermost layers of the bounding sclera and a circumferential collagen ring in the mid-stromal tissue. Higher spatial resolution rendering of individual lamina cribrosa beams within the nerve head is also demonstrated. Validation of the method is provided in the form of correlative results from wide-angle X-ray scattering and application of the presented method to other fibrous tissues.

SHG is a coherent, nonlinear scattering process where the combined energy of two photons, made to arrive virtually simultaneously at an appropriate molecular structure, is scattered as a single photon at exactly half the wavelength of the incident photons. SHG is only exhibited by non-centrosymmetric molecules such as fibrillar collagen, myosin and tubulin, and the process only occurs at the focal plane of the laser beam, allowing fine and deep-penetrating optical sectioning, even in turbid samples. Moreover, due to the intrinsic nature of SHG emission, no tissue labelling or sectioning is required. Nonlinear laser scanning multiphoton microscopy was performed using a Zeiss LSM 880 META NLO microscope. SHG signals from fibrous collagen were generated using an ultrafast titanium-sapphire tunable infrared (680–1080 nm) laser.

Fiber orientation Analysis

In this article Pijanka et al. describe an automated image analysis method based on tile partitioning of an SHG image and calculation of the fiber structure within each tile using 2D DFT (Fig. 1). The angular distribution of the integrated DFT power spectrum is then extracted and used to calculate and map the preferred orientation of the collagen fibers, the aligned fiber content and the degree of fiber recruitment around the main direction. The method also features an in-built correction for tile edge artefact that adopts the periodicity plus smooth image decomposition (PPSID) algorithm, avoiding the significant loss of peripheral image information encountered with commonly used alternative windowing correction methods, and resulting in comparatively minimal distortion of the resulting calculated fiber distribution (Fig. 2). The latter issue has been largely overlooked in previous studies that utilize DFT to quantify fiber organization from SHG images.

The analysis of SHG images recorded from the human optic nerve head (ONH) using the authors' algorithm was able to quantify main collagen fiber structural features that corresponded well to previously published literature employing alternative scattering and imaging methods (Fig. 3). Specifically, innermost layers of the peripapillary sclera presented strong radial alignment, whereas the mid-sclera exhibited strong circumferential orientation of collagen fibers around the scleral canal. Pijanka et al. were also able to demonstrate the applicability of the technique to image other collagen tissues by characterizing the highly organized uniaxial alignment of rat tail tendon collagen (Fig. 4) and the fixed/rotated orthogonal lamellar structure of the avian cornea (Fig. 5). Moreover, the potential for Fourier quantification of other fiber networks imaged through different imaging modalities was demonstrated by applying the presented method to fluorescence confocal images of cytoskeletal actin fiber networks in cultured fibroblasts (see original article).

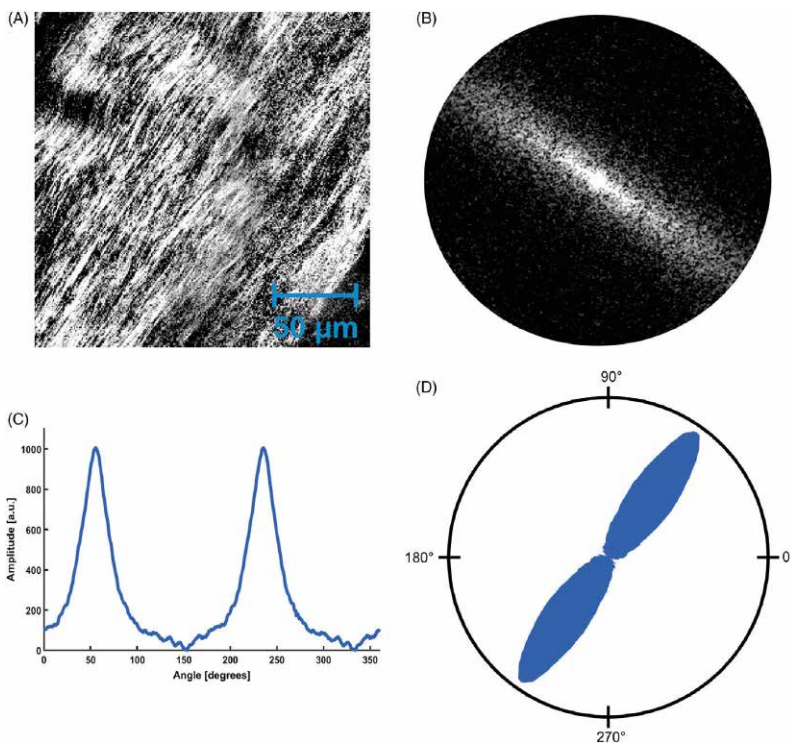


Fig. 1.: Obtaining fiber orientation from a SHG image. A, SHG image of a collagen fibers within human peripapillary sclera (PPS) tissue. B, power spectrum of the image presented in (A) resulting from two-dimensional (2D) discrete Fourier transform. C, angular distribution plot of the radially-integrated power spectrum, shifted 90 degrees to represent the fiber orientation distribution. D, corresponding polar vector plot of (C).

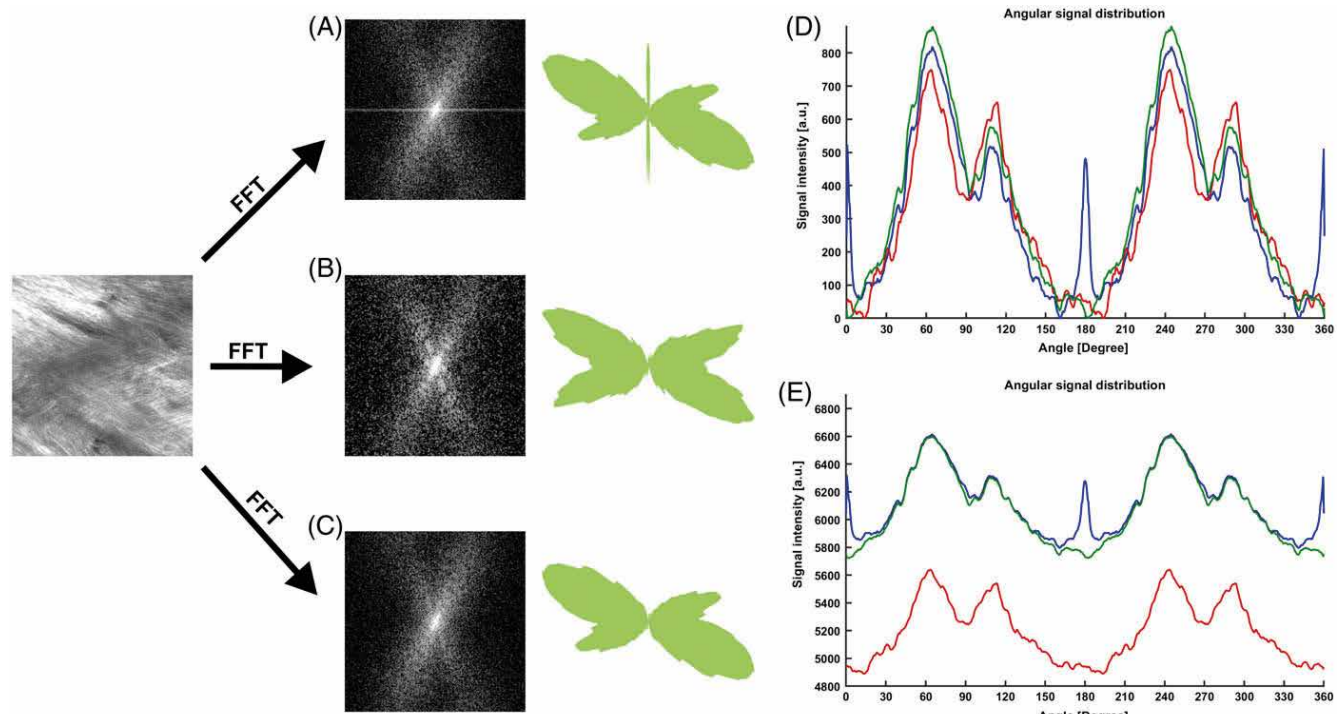


Fig. 2.: Comparison of different DFT edge artefact correction methods on fiber orientation data. A, the results of DFT on the polar vector plots without any edge correction applied—note presence of horizontal/vertical component of cross artefact in DFT spectrum/fiber polar

plot, respectively. B, the effect of Hanning window function—note changes to polar plot lobe shapes. C, the effect of PPSID function—note lobe shapes are better preserved than in (B). D, comparison of angular power distribution for all three methods. E, angular distribution

profiles without the background component removed showing the overall drop in amplitude from lost peripheral data in the windowing function method. For (D) and (E): blue, no correction; red, Hanning window method; green, PPSID method.

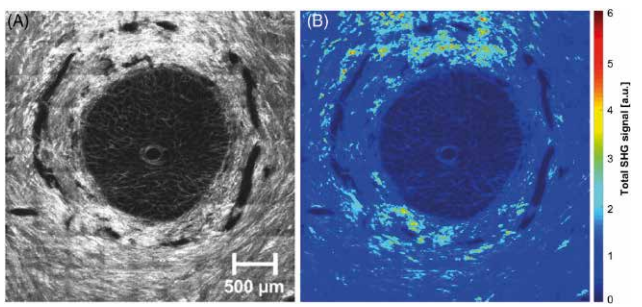


Fig. 3.: A, SHG image tiling of a mid-stromal section through the human ONH. **B,** corresponding spatial map of total SHG signal per sampled tile. Resolution of sampled tiles is 16×16 pixels.

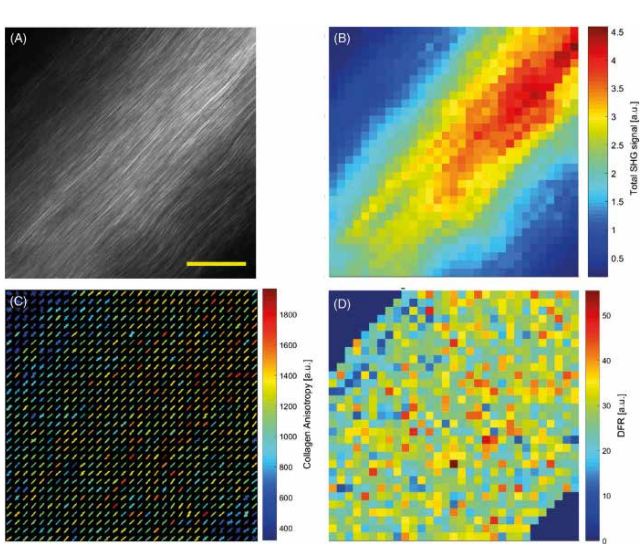


Fig. 4.: SHG/ DFT analysis of collagen in intact rat tail tendon. A, SHG image of an individual optical section through the middle of a single, intact tendon from rat tail oriented obliquely in the field of view (FOV) (bar = 100 μ m). B, map of integrated SHG signal, sampled every 16 pixels (20 μ m). C, polar vector map of collagen fiber orientation from DFT analysis, confirming and quantifying the high uniaxial alignment of collagen along the tendon direction (D) Map of degree of fiber recruitment (DFR) around the principal fiber direction.

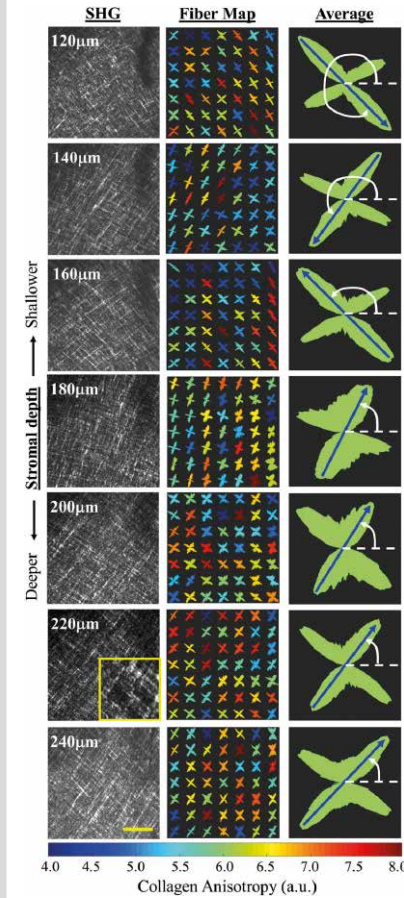


Fig. 5.: Depth-resolved second harmonic generation SHG/ DFT analysis of the posterior half of the corneal stroma from the adult chicken. Left column: SHG images reveal orthogonal collagen fiber networks (bar = 100 μ m). Yellow box at 220 μ m depth shows stroma at 3 \times magnification of standard images. Centre column: polar vector plots of collagen fiber orientation from DFT analysis (sampled every 64pix/50 μ m), confirming and quantifying the orthogonal lamellar structure. Right column: averaged polar vector plot at each stromal depth. The fixed orientation of the deepest layers (240–200 μ m) can be observed, followed by a counter-clockwise rotation when traversing the stroma in a posterior to anterior direction (180–120 μ m). The blue arrow is used to visually track the rotation angle of one of the two principal fiber populations.

X-ray data analysis

As the orientation analysis approach the authors employed herein shows commonality with that of the wide-angle X-ray scattering (WAXS) analysis previously developed by their group, Pijanka et al. were able to carry out correlative studies to validate the former method, obtaining general agreement in the main collagen directions between the two methods when applied to the same specimens. In comparing the results of the two

methods, it is important to reiterate that, although the sampling intervals of the two methods used were identical (0.25 mm), the actual sampled areas per data point were different (0.0625mm² for SHG compared with 0.012mm² for WAXS). Furthermore, the WAXS signal is of molecular origin and will be subject to a minor angular broadening of the orientation peak due to the ~5° inclination of the microfibril axis with respect to the fibril direction. As a further caveat, the difference in age of the two

human sclera specimens studied before was 17 years. Based on the results of previous WAXS and finite element modelling studies, this would not have likely resulted in any marked differences in the gross collagen fiber arrangement between the two specimens, but still could have manifested in more subtle variations in collagen anisotropy.

The option within the current method to change sampling interval (i.e., size of the image area that the DFT power spec-

trum is calculated, and collagen orientation is determined from) enables analysis of diverse tissue types. For example, processing SHG images with finer sampling intervals facilitates analysis of porous or fenestrated tissues such as the individual lamina cribrosa beams of the ONH, as demonstrated herein. On the other hand, mapping a continuous tissue such as the sclera with larger tile dimensions is often preferable when more regional averaging is desirable, for example, to obtain representative regional parameters for biomechanical modelling. Indeed, the ability of the current method to obtain region-averaged fiber distributions with, importantly, sub-degree angular resolution, renders the data amenable to inclusion in inverse finite element simulation—as demonstrated previously with similar data sets obtained from ocular tissues using WAXS. Providing sufficient initial image resolution and effective noise filtering is obtained (in the present method the latter is achieved using the MATLAB software peak prominence function), it is feasible to analyse not only the principal fiber orientation but also additional sub-populations—for example in tissue regions where multiple fibers are crossing at different angles. This contrasts with a number of previous studies employing DFT in which only the main fiber direction is detected and the overall distribution quantified, for example those using an aspect ratio approach.

Extracting frequency component amplitudes directly from the Fourier transform (FT) power spectrum enables ready control of the frequency range (and hence corresponding length scale in the spatial domain) for analysis. This facilitates improvements in accuracy by allowing the targeting of fibers, while excluding frequencies from other structures, in order to reduce noise. This could be exploited, for example, to characterize collagen fiber crimp. A possible future enhancement of the current method could involve the addition of semi-automated frequency filtering to attenuate undesired radial frequencies. Marquez studied the effects of a band-pass filter and concluded that an optimal filter in concentrating DFT power on the fiber orientation is centered on frequency corresponding to a wavelength of twice the fiber width and a bandwidth of $\pm 10\%$.

Limiting Factors

The presented work is subject to a number of limiting factors. First, there are limitations inherent in the SHG tissue preparation and data collection itself. Microtome sectioning of the tissue results in mechanical disrup-

tion at the surfaces of the sections. Owing to the optical sectioning capabilities of SHG microscopy, erroneous surface data can be readily isolated and discarded, albeit at a cost of information. Further, as an imaging method, quantification of SHG can only be done from the information visible in the image section, fibers passing out of plane are not counted in the analysis, which can lead to an underestimation of signal in interwoven tissues, or where significant out-of-plane inclination of fibers is present. This is a disadvantage compared with scattering methods such as WAXS or small angle light scattering (SALS), where virtually all fibers in the path of beam are detected. However, fine optical sections of 1 to 1.5 μm are possible with most multiphoton instruments, making tracking of inclined fibers through a section feasible if required. Also, while Pijanka et al. used laser power ramping to effectively normalize against depth-related signal attenuation, this does rely on the assumption of isotropy in real tissue signal through a section. Any variation in the latter may manifest in some residual depth attenuation or overcorrection throughout a section, which would impact the total SHG signal measurement in direct proportion to the attenuation factor, and (to a smaller degree) the absolute anisotropy measurement (polar plot color scaling). However, this would not have affected the relative amount of aligned collagen, the relative number of fibers at each angle or the DFR values measured by technique of the authors, nor would it have any effect on the spatial distribution of any measured parameter at a given section depth. Furthermore, while the SHG microscope optics achieve near-circular polarization of the beam as it exits the objective, tests carried out on their system using an appropriate linear test sample (rat tail tendon) indicated that the polarization is marginally elliptical, resulting in a maximum bias of approximately 13% in the signal intensity in the horizontal over the vertical direction (data not shown). Second, there are limitations connected with the authors' DFT analysis method. Depending on the original resolution of the SHG images collected, there is a limitation on the smallest tile that can yield a useable DFT capable of detecting fiber orientations. In the present study, they obtained accurate fiber data from 16 \times 16 pixel tiles with an original 512 \times 512 pixel resolution image (Fig. 3). Unlike some other methods, it is not possible to analyse signal on the single pixel level or to easily track individual collagen fibers. In this aspect, fiber tracking methods that analyse images in the spatial domain are more effective. For example, curvelet transform fiber extraction (CT-FIRE) and F-Segment can

track fiber dimension, number and volume, and polarization light microscopy can more effectively follow orientation.

Summary

This paper presents a variation on quantitative multiphoton imaging of connective tissue structure using DFT, which has two novel aspects. First, it harnesses a novel PPSID algorithm to virtually eliminate peripheral data loss from image tiles during DFT analysis. Second, by mimicking the superior quantitative capabilities of scattering methods and combining them with the fine optical sectioning capacity of nonlinear microscopy, rapid and accurate fiber quantification can be achieved, yielding data suitable for input into biomechanical modelling. In future, with the collection of optical slices at sufficiently fine resolution, and with careful and precise registration of the images, the presented method could be extended to carry out full quantitative determination of tissue organization in three dimensions.

Digest of

Pijanka JK, Markov PP, Midgett D, et al.; *Quantification of collagen fiber structure using second harmonic generation imaging and two-dimensional discrete Fourier transform analysis: Application to the human optic nerve head;*

Journal of Biophotonics 2019; e201800376.
© 2018 WILEY-VCH Verlag GmbH & Co. KGaA,
Weinheim

<https://doi.org/10.1002/jbio.201800376>

Lipopolysaccharide-induced alteration of mitochondrial morphology induces a metabolic shift in microglia modulating the inflammatory response in vitro and in vivo

Nair S, Sobotka K S, Joshi P, et al.

Accumulating evidence suggests that changes in the metabolic signature of microglia underlie their response to inflammation. The authors attempted to expand their knowledge of how proinflammatory stimuli induce metabolic changes. Primary microglia exposed to lipopolysaccharide (LPS)- expressed excessive fission leading to more fragmented mitochondria than tubular mitochondria. LPS-mediated activation of Toll-like receptor 4 (TLR4) also led to metabolic reprogramming from oxidative phosphorylation (OXPHOS) to glycolysis. The blockade of mitochondrial fission by Mdivi-1, a putative mitochondrial division inhibitor led to the reversal of the metabolic shift. Mdivi-1 treatment also normalized the changes caused by LPS exposure, namely an increase in mitochondrial reactive oxygen species (ROS) production and mitochondrial membrane potential and the accumulation of key metabolic intermediate of TCA cycle succinate. In addition, treatment with mitochondrial division inhibitor 1 (Mdivi-1) significantly reduced LPS induced cytokine and chemokine production. Finally, this report showed that Mdivi-1 treatment attenuated gene expression associated with cytotoxic, repair and immunomodulatory microglia phenotypes in an in vivo neuroinflammation paradigm. In summary, these data show that the activation of microglia into a classic proinflammatory state is associated with a switch to glycolysis mediated by mitochondrial fission, a process that may be a pharmacological target for immunomodulation.

Images were acquired with a Zeiss LSM 880 Airyscan super-resolution system with live cell capabilities and fitted with the fast-AS module. Microscopes were equipped with an environmental chamber during imaging. Super-resolution structured illumination microscopy (SR-SIM) on a Zeiss ELYRA PS.1 microscope was used to yield a two-fold improvement in all spatial directions beyond the classical Abbe-Rayleigh limit. GFP was imaged using a Plan-Apochromat 100 \times /1.4 oil objective. The SR-SIM images were acquired as z-stacks with three angles and five phases in each plane and the z-step between planes was 3.30 nm. SR-SIM processing was performed using the Zeiss Zen software package.

This study strengthens our knowledge of the links between mitochondrial architecture, inflammation, and energy metabolism in microglial cells. We have shown that activation of microglia to a proinflammatory activation state increased mitochondrial fragmentation, which was accompanied by a reduction in oxidative phosphorylation and an increase in glycolysis, which was dose and time dependent (Fig. 1). Pre-

treatment with the putative mitochondrial division inhibitor 1 (Mdivi-1) normalized LPS-induced mitochondrial fragmentation (Fig. 2), normalized the cellular respiration, and glycolysis to control levels. Mdivi-1 greatly reduced LPS-induced cytokine production, normalized LPS-induced ROS production (Fig. 3) and mitochondrial membrane potential (Fig. 4).

Neuroinflammation includes complex changes in microglial phenotypes, mediated by gene expression changes leading to the production of cytokines and chemokines and production of ROS. Overall, this leads to oxidative and nitrosative stress in the brain. Here it was observed as expected that LPS-activated microglia produced a plethora of chemokines and cytokines and ROS. In this proinflammatory scenario, suppression of LPS-induced mitochondrial ROS plays a role in modulating the production of proinflammatory mediators by preventing MAPK and NF- κ B activation suggesting a potential therapy for inflammation-associated degenerative neurological diseases (Park et al., 2015).

Changes in mitochondrial structure

To understand LPS-induced changes in mitochondrial structure, the authors used super-resolution 3D ELYRA-SIM (Shim et al., 2012) to quantify mitochondrial morphology which revealed that high-dose LPS for 24 hr increased fragmentation (Fig. 1). A low dose of LPS caused an initial increase in oxygen consumption rates (OCR), which was not accompanied by any change in mitochondrial morphology. However, a higher dose of LPS induced a decrease of OCR and a further increase of extracellular acidification rates (ECAR) accompanied by mitochondrial fission. Fragmented mitochondria constitute the preferred morphological state when respiratory activity is low. A high or moderate dose of LPS caused a decrease in respiration, and cells became dependent on glycolysis favoring excessive fragmentation. The molecular mechanisms behind this response is not known, but it has been proposed that the energy depletion elicits mitochondrial fragmentation and subsequent mitophagy. Increased

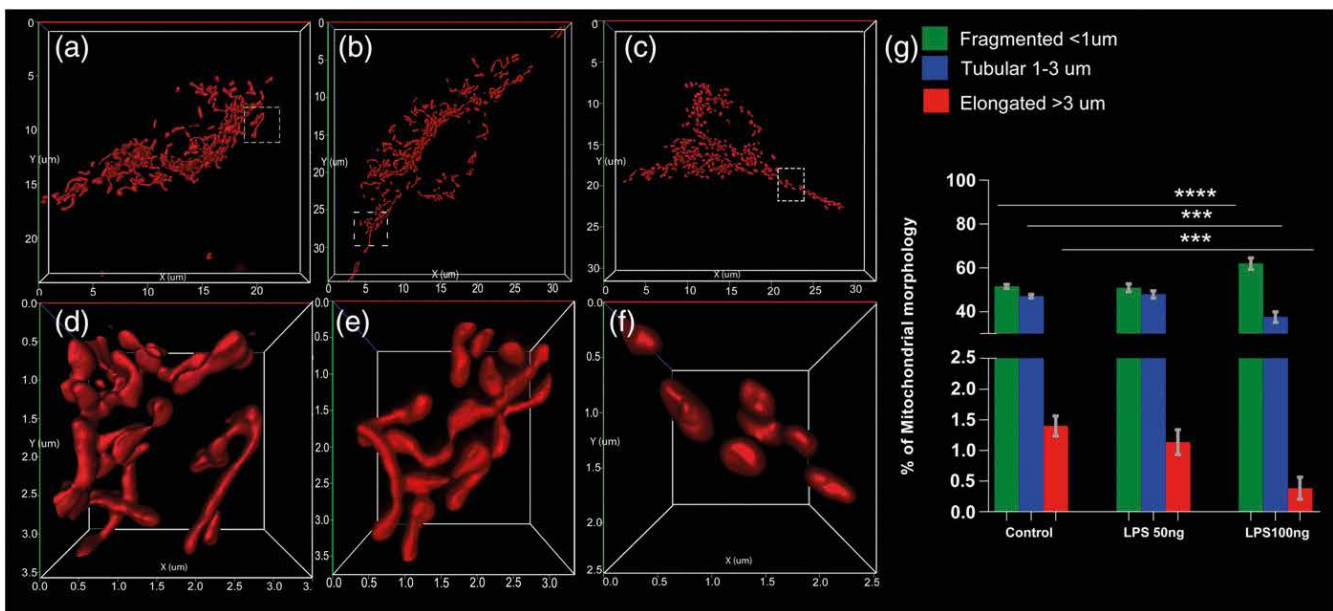


Fig. 1. Lipopolysaccharide (LPS) induces dose-dependent mitochondrial fragmentation. Super-resolution microscopy reveals excessive mitochondrial fragmentation (a) control, (b) 50 ng/mL LPS exposure for 24 hr, (c) 100 ng/mL LPS

exposure for 24 hr, (d-f) shows a higher magnification of the image in the white square in the upper panel. (g) Graphs showing results from an analysis of mitochondria morphology in primary microglia cells treated with LPS for 24 hr. The

data are for at least 12 cells per condition in three independent experiments. Bar graphs expressed as mean \pm SEM. *** $p \leq 0.001$; Student's t test calculating the difference between control and LPS treated groups.

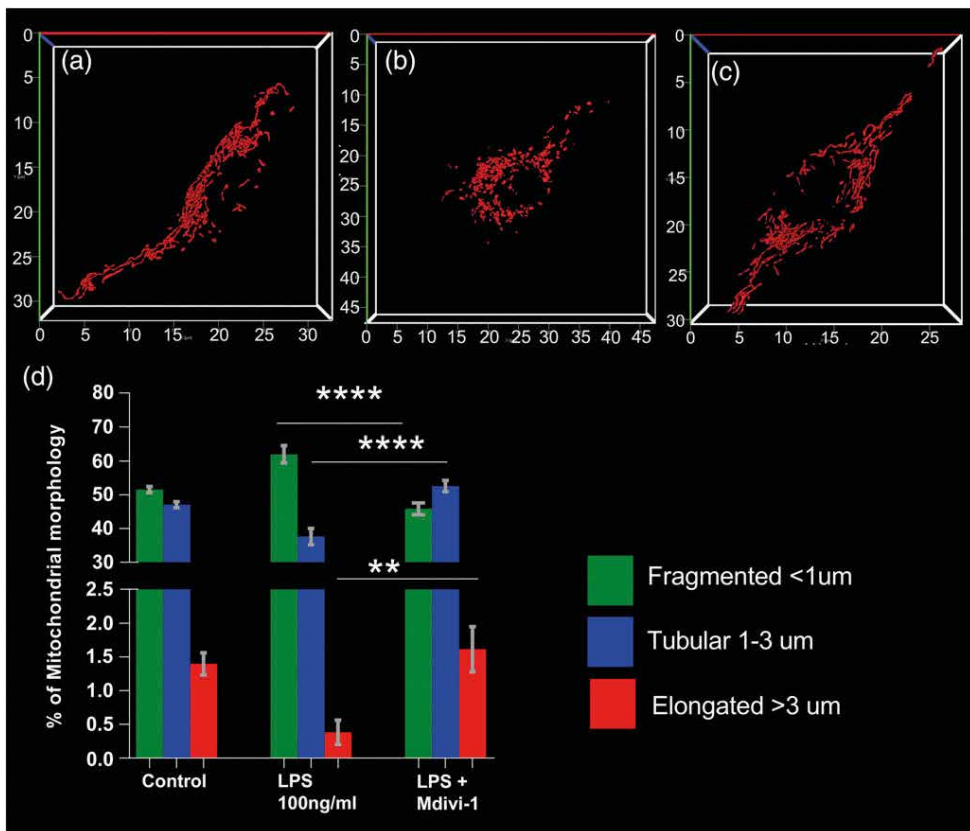


Fig. 2. Pharmacologic blockade of DRP1 by Mdivi-1 re-established mitochondrial morphology. Mdivi-1 pretreatment (25 μ M) for 1 hr followed by LPS (100 ng/mL) exposure for 24 hr resulted in a decrease of fragmented mitochondria and an increase in tubular and elongated mitochondria (d). (a) Control cells treated with vehicle (DMSO), (b) LPS (100 ng/mL) exposure for 24 hr, (c) LPS (100 ng/mL) + Mdivi-1. Bar graphs expressed as mean \pm SEM. The data are for at least 12 cells per condition in three independent experiments. ** $p \leq 0.01$; *** $p \leq 0.001$; Student's t-test calculating the difference between LPS and LPS + Mdivi-1 groups. DRP1 = dynamin-related protein 1; LPS = lipopolysaccharide.

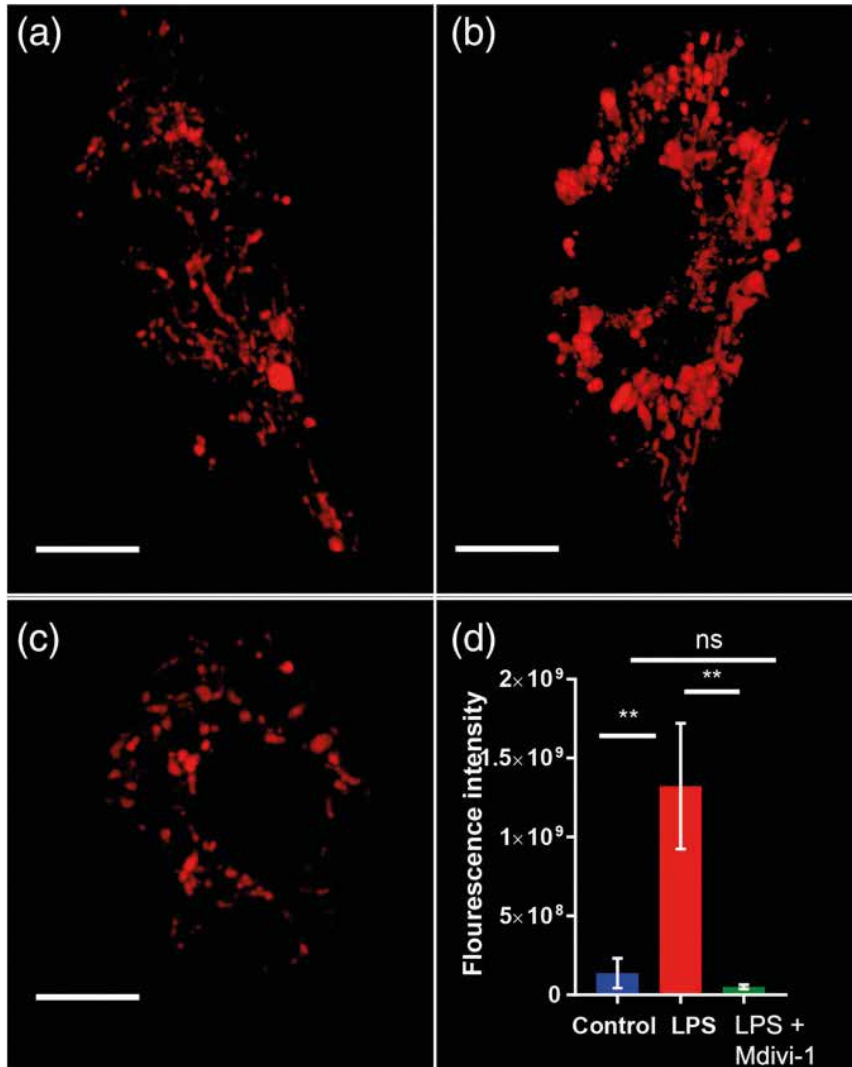


Fig. 3.: Mdivi-1 treatment abolished lipopolysaccharide (LPS)- induced mitochondrial reactive oxygen species production.

(a) Control, (b) 100 ng/mL LPS exposure for 24 hr, (c) LPS + Mdivi-1, (d) graphs showing results from an analysis of mitochondrial superoxide indicator (mitoSOX) fluorescence by live cell airyscan microscopy. The data are for at least 12 cells per condition in three independent experiments. Bar graphs expressed as mean \pm SEM. ** $p \leq 0.01$; Student's t-test calculating the difference between control LPS and Mdivi-1 treated groups.

The fluorescence intensity of MitoSOX increased 24 hr after the LPS stimulation (100 ng/mL, 24 hr). Treatment with Mdivi-1 (25 μ M, 1 hr) before LPS exposure abolished the increase in MitoSOX fluorescence intensity observed 2 hr after the LPS stimulation. These results indirectly show that that mitochondrial fission (induced by TLR4 stimulation) increases ROS production as shown in this study and others.

mitochondrial fragmentation due to excessive fission can exacerbate the inflammatory response of microglia through modulation of dynamin-related protein 1 (DRP1) dephosphorylation and elimination of ROS. Nair et al. chose to use Mdivi-1, a mitochondrial division inhibitor, to study microglial metabolism as it related to mitochondrial morphology as previous studies revealed that LPS exposure in microglia cells leads to activation of mitochondrial fission protein DRP1 (Fig. 2).

Mdivi-1 is a widely accepted DRP1 mediated mitochondrial fission inhibitor used in many studies. The data from the authors supports the assertion that changes in mitochondrial dynamics may be needed for the expression of inflammatory mediators in activated microglia cells. Mdivi-1 has previously been shown to attenuate LPS-induced ROS and proinflammatory mediator production in a BV-2 microglial cell line with a very

high dose of 1 μ g/mL. BV2 cells are similar to primary microglia, but they contain oncogenes that render them phenotypically different with regard to, for example, proliferation and adhesion. The findings here not only show that pretreatment with Mdivi-1 reduced LPS-induced mitochondrial fragmentation and expression of proinflammatory mediators but also normalized mitochondrial function in microglia. These data support the suggestion that increasing the fusion/fission ratio reduces the extent of neuroinflammation. To further support the potential validity of targeting fission as a therapeutic strategy, the authors tested the ability of Mdivi-1 to modify microglial activity in vivo. We used a paradigm of systemically driven neuroinflammation, wherein an Intraperitoneal (IP) injection of the inflammatory agent interleukin-1 β induces a highly complex neuroinflammatory reaction involving microglia. Supporting our in vitro data

Mdivi-1 was able to reduce the expression of genes associated with classically proinflammatory genes and the anti-inflammatory activation state, which is associated with the in vivo inflammatory reaction.

Oxygen Consumption and extracellular acidification rates as a function of LPS doses

Previous work with BV2 demonstrated that LPS causes an inhibition of OXPHOS. However, this study used a very high dose of LPS (1 μ g/mL) which is shown to elicit mitochondrial toxicity. Nair et al. demonstrate for the first time that a low or moderate dose of LPS (50 ng/mL) results in an increase of ATP-linked OCR and basal respiration in support of another study in skeletal muscle cells where they used a very low dose of LPS in isolated mitochondria. High dose of LPS

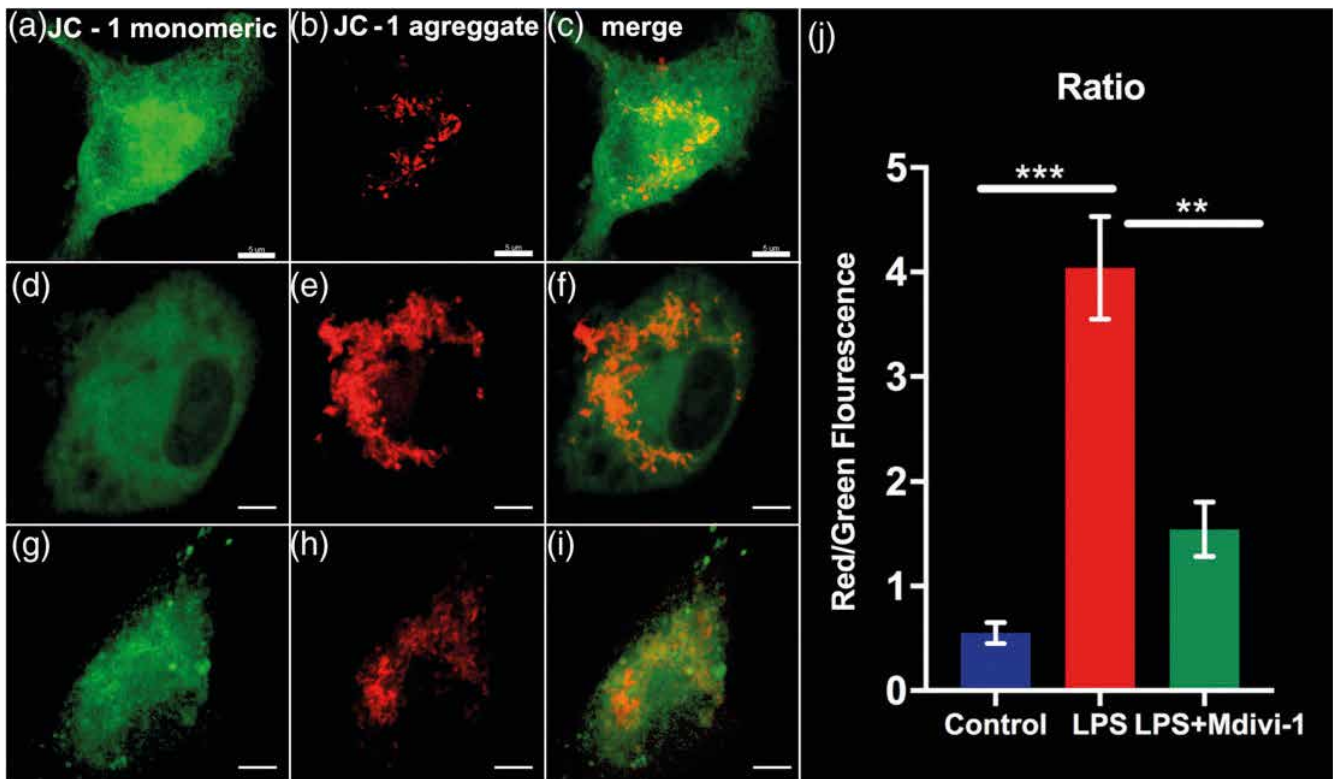


Fig. 4.: Mdivi-1 treatment attenuated lipopolysaccharide (LPS) induced increase of mitochondrial membrane potential: (a–c) control, (d, f) 100 ng/mL LPS exposure for 24 hr, (g, i) LPS + Mdivi-1. Graphs showing results from an analysis of JC1 fluorescence 525/565 nm by live cell airyscan microscopy. The data are for at least six

cells per condition in three independent experiments. Bar graphs expressed as mean \pm SEM. ** p $<$ 0.01, *** p $<$ 0.001, Student's *t*-test.

The observations suggest that after LPS (100 ng/mL) exposure for 24 hr microglia mainly depended on glycolysis for energy production. Therefore, the mitochondrial membrane potential using the mitochon-

drial membrane potential probe JC-1 in these conditions was investigated. As a consequent it was found that elevation of mitochondrial membrane potential and treatment with Mdivi-1 significantly reduced mitochondrial membrane potential (525/565 nm) ratio compared with LPS treated group.

(100 ng/mL) caused a decrease in carbonyl cyanide-4-(tri-fluoromethoxy)phenylhydrazone (FCCP)-induced maximal respiration and an increase in leak-driven respiration. A depletion of spare respiratory capacity was found at 6 and 24 hr following LPS exposure. However, we have noted no significant difference in cell viability or death after LPS.

OCR exhibited a biphasic response characterized initially by an increase of OCR in response to low LPS and then a marked drop of OCR after moderate to high doses of LPS, whereas ECAR increased in proportion to the dose of LPS. The authors interpret the initial increase of OCR as a means to match an increased demand of ATP. However, as the proinflammatory stimulus becomes stronger, it appears favorable to shift from mitochondrial respiration to aerobic glycolysis (Warburg effect) to promote more rapid ATP production and synthesis of inflammatory mediators such as cyto-

kines/chemokines and ROS. We believe the Warburg effect is an important concept for understanding metabolic changes occurring during microglial activation. It is shown that also activation of macrophages or dendritic cells (DCs) with LPS induces a metabolic switch from OXPHOS to glycolysis. Metabolic shift may be facilitated by increased mitochondrial fission and/or reduced fusion mediated by DRP1 activation. However, as glycolysis is less efficient at producing ATP than OXPHOS, this metabolic reorientation cannot solely be to meet energy demands. Glycolysis may also facilitate cytokine production by producing intermediate metabolites. A previous study found that glycolysis was required to produce optimal interferon-gamma (IFN- γ) during T cell activation and is translationally regulated by the binding of the glycolysis enzyme GAPDH to IFN- γ mRNA.

Increase of mitochondrial membrane potential by attenuated LPS treated with Mdivi-1

The present results in microglia add to what has already been shown in DCs and macrophages, specifically that proinflammatory activation resulted in increased succinate accumulation. In DCs and macrophages, this succinate accumulation was related to an altered Krebs cycle and this was normalized by Mdivi-1. Aberrant mitochondrial fission alters the Krebs cycle, by interfering with the processes after citrate and after succinate by reducing of cytochrome c oxidase and succinate dehydrogenase activity. Impaired succinate dehydrogenase activity results in succinate accumulation due to impaired succinate to fumarate conversion. Accumulated succinate drives reverse electron transport (RET) to generate excessive mitochondrial ROS production. These data by Nair et al.

support this link between accumulation of succinate and ROS production, which was prevented by Mdivi-1 (Fig. 3).

LPS induced an increase in proton leak with an increase in membrane potential. Proton leak is partly mediated by uncoupling proteins (UCPs) present in the mitochondrial inner membrane. It is shown that in primary microglia LPS induces an increase in UCP2 levels and membrane potential. UCP2-silenced microglia stimulated with LPS show a decrease in membrane potential. In macrophages LPS stimulation repurpose their mitochondria from ATP production to succinate-dependent ROS generation, with glycolysis taking on the role of ATP generation. In this case, mitochondria sustain a high membrane potential because protons generated by the electron transport chain to make ATP are no longer being consumed by mitochondrial ATP synthase. Macrophages can also reorganize their respiratory chain in response to a bacterial infection, decreasing Complex I levels and increasing the activity of Complex II. These changes boost production of proinflammatory cytokines such as interleukin 1 β (IL-1 β). The here available data support these findings as normalizing mitochondrial membrane potential and ROS production with Mdivi-1 abolished pro- and anti-inflammatory cytokine and chemokine release (Fig. 4).

Aberrant activation of microglial affects neurodegenerative processes through various neurotoxic cascades. It has been shown by the authors that proinflammatory microglial activation alters cellular bioenergetics by inducing mitochondrial dysfunction and promoting a switch to glycolysis, supported by excessive mitochondrial fragmentation, and increased cytokine output. This is likely an adaptive mechanism as the transition of sensing and surveying microglia into an activated state is likely to be accompanied by significantly increased energy consumption. Preventing excessive mitochondrial fission in microglial cells stimulated with LPS using a fission inhibitor Mdivi-1 normalizes mitochondrial respiration and glycolysis and attenuates the release of cytokines/chemokines. These lines of in vitro morphological and functional data and the in vivo data suggest that regulating mitochondrial dynamics may be a useful therapeutic modality for preventing neurological disorders caused by aberrant microglia activation.

Summary

Lipopolysaccharide (LPS) exposure induces excessive mitochondrial fragmentation as well as a switch from oxidative phosphorylation (OXPHOS) to glycolysis (metabolic

reprogramming) in microglial cells. Mdivi-1 treatment blocks LPS-induced mitochondrial fragmentation and ROS production and normalized oxygen consumption rates OCR and ECAR in the microglia cells. Furthermore, Mdivi-1 reduces the LPS induced release of cytokines and chemokines and suppresses LPS-induced succinate production. Additionally, inhibition of mitochondria fission by Mdivi-1 suppresses mitochondrial ROS production. Finally, the Mdivi-1 treatment attenuates LPS to increase the potential of the mitochondrial membrane and attenuates microglial activation in the mouse paradigm of neuroinflammation. For investigating the dynamics and the fine morphology of the mitochondrial network the combination of Life cell LSM imaging and Elyra superresolution is perfectly suited to enlight these processes.

*Digest of
Nair S, Sobotka KS, Joshi P, et al.;
Lipopolysaccharide-induced alteration
of mitochondrial morphology induces a
metabolic shift in microglia modulating the
inflammatory response in vitro and in vivo;
Glia 2019;1–15.
© 2018 Wiley Periodicals, Inc
<https://doi.org/10.1002/glia.23587>*

Pbx loss in cranial neural crest, unlike in epithelium, results in cleft palate only and a broader midface

Welsh IC, Hart J, Brown JM, et al.

This study provide in-depth analysis of PBX1 and PBX2 protein localization from early stages of midfacial morphogenesis throughout development of the secondary palate. The authors further establish CNCC-specific roles of Pre-B-cell leukemia transcription factors (PBX TFs) and describe the developmental abnormalities resulting from their loss in the murine embryonic secondary palate. Additionally, they compare and contrast the phenotypes arising from PBX1 loss in cranial neural crest cell (CNCC) with those caused by its loss in the epithelium and show that CNCC-specific Pbx1 deletion affects only later secondary palate morphogenesis. Moreover, CNCC mutants exhibit perturbed rostro-caudal organization and broadening of the midfacial complex. Proliferation defects are pronounced in CNCC mutants at gestational day (E)12.5, suggesting altered proliferation of mutant palatal progenitor cells, consistent with roles of PBX factors in maintaining progenitor cell state. Although the craniofacial skeletal abnormalities in CNCC mutants do not result from overt patterning defects, osteogenesis is delayed, underscoring a critical role of PBX factors in CNCC morphogenesis and differentiation. Overall, the characterization of tissue-specific Pbx loss-of-function mouse models with orofacial clefting establishes these strains as unique tools to further dissect the complexities of this congenital craniofacial malformation. This study closely links PBX three-amino-acid loop extension (TALE) homeodomain proteins to the variation in maxillary shape and size that occurs in pathological settings and during evolution of midfacial morphology.

Histological analysis was performed with an upright Zeiss AxioPlan microscope. Scanning electron microscopy analysis on Embryos was performed with Zeiss Leo 1550 SEM. Fixed, unstained E18.5 mouse embryos were scanned at 18 μm resolution using a Zeiss Xradia Versa 520 XRM.

Midfacial development depending on PBX1 and PBX2

In the midface, primary and secondary palate development involves stereotypic morphogenetic processes (outgrowth, proliferation, elevation, fusion). The identification of key regulatory factors with restricted spatiotemporal expression that drive reciprocal tissue interactions between cephalic epithelium and CNCC-derived mesenchyme is critical to the authors' understanding of how coordinated midfacial development is achieved. Among multiple transcription factors (TFs), their study establishes that PBX homeodomain proteins function in a tissue-specific manner as well as iteratively to govern the morphogenesis and fusion of the primary and secondary palate.

High levels of PBX1 and PBX2 proteins are present in both cephalic epithelium and CNCC-derived mesenchyme from early

stages of midfacial development, before primary and secondary palatogenesis has occurred and before the facial processes have fully developed, throughout subsequent midfacial morphogenesis (Fig. 1 und 2). Notably, PBX1 and PBX2 exhibit largely overlapping localization, with PBX2 consistently present at lower levels in primary and secondary palatal domains. This underlies collaborative roles and iterative functions of these two family members in patterning and morphogenesis of the midface, which complements previously reported genetic interactions of Pbx1 and Pbx2 in directing the development of multiple organ systems.

Consistent with the expression pattern of Pbx1 and Pbx2 in the midface, Welsh et al. observed striking but distinct phenotypes in the primary and secondary palate of Pbx epithelial (Pbx1fl/fl; Foxg1Cre/+ and CNCC mutant (Pbx1fl/fl; Pbx2+/-; Wnt1-Cretg/+)) embryos, respectively. By studying conditional loss of PBX factors in the cephalic epithelium, here they expanded previous findings on the early roles of these homeodomain proteins in upper lip and primary palate morphogenesis and fusion. Notably, in the present study, only epithelial mutant embryos present Cleft lip with or without cleft palate (CL/P) with 67% penetrance. An earlier report in epithelial mutants demonstrated

the presence of CL/P with 100% penetrance. However, in that study, embryos were also heterozygous for a constitutive null Pbx2 allele (Pbx1fl/fl; Pbx2+/-; Foxg1Cre/+), thus sensitizing the genetic background so as to increase the penetrance of this phenotype. In epithelial mutants with unilateral cleft lip, a direct relationship between clefting of the lip and clefting of the primary palate with only one exception has been observed. In contrast, isolated cleft lip is reportedly as high as 42% in some human populations, even though it was suggested that individuals diagnosed with cleft lip may have underdiagnosed sub-clinical palatal defects. These findings give weight to the current notion that, whereas in mouse models such variable defects may be interpreted as lack of penetrance, in humans overt clefting phenotypes may be part of a broad morphological spectrum. Here, the authors also demonstrate a high incidence (95%) of cleft secondary palate in epithelial mutants. However, morphometry shows that these mutants exhibit a broadening of the midface. Given the observed widening of the primary palate at the onset of secondary palate morphogenesis in epithelial mutants, it is not unreasonable to assume that overall disruption of normal midfacial proportions could make clefting of the secondary palate a probable outcome.

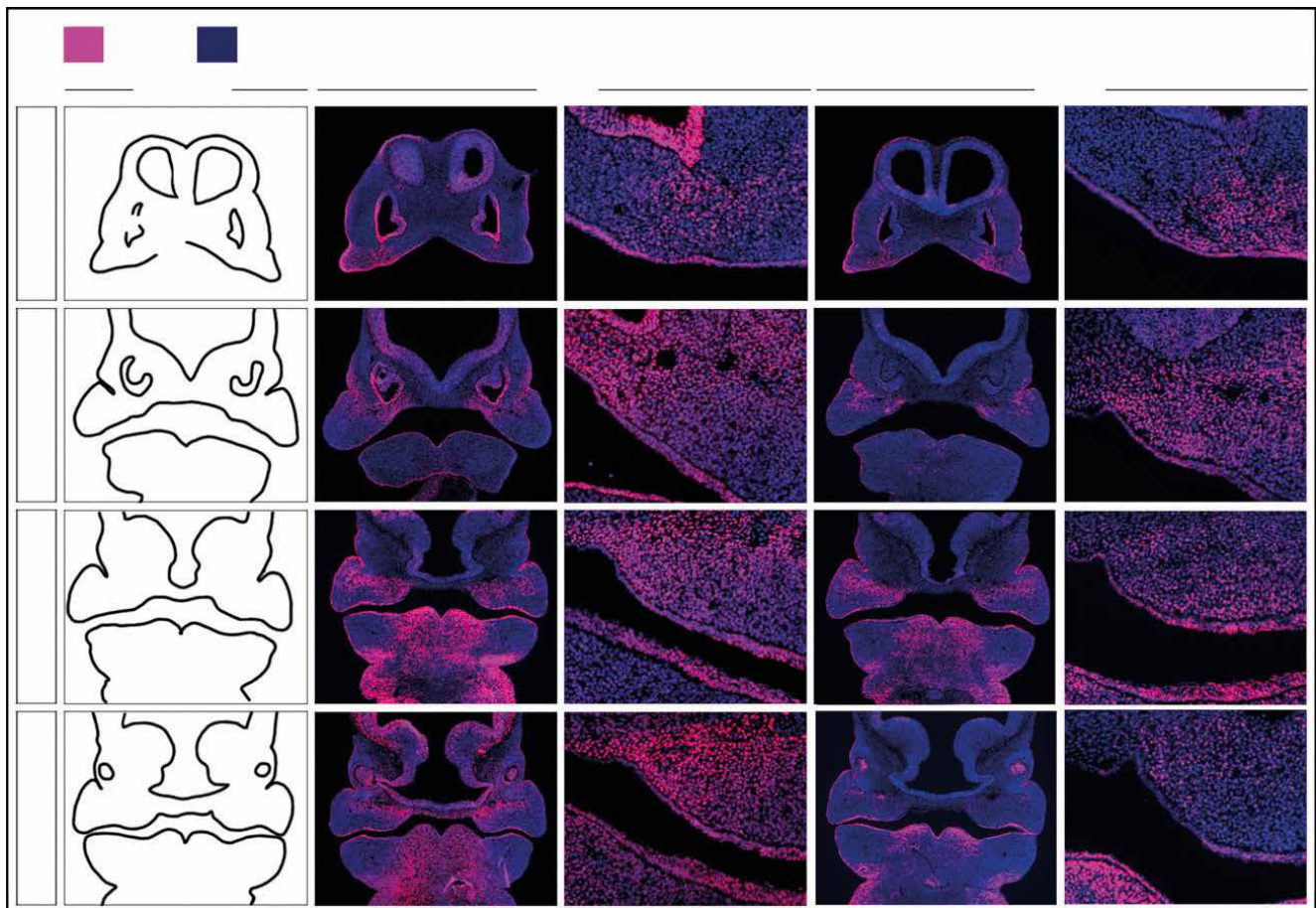


Fig. 1.: Localization of PBX1 and PBX2 in the developing midface at E11.5. Representative micrographs of immunofluorescence with PBX1- and PBX2-specific antibodies on coronal sections through the primary and secondary palate. Cartoons of primary palate and secondary palate (anterior, mid, and posterior) are shown in left-most column. PBX1 and PBX2 proteins, fuchsia signal; DAPI highlighting the nuclei, blue. Primary palate: (A–D) PBX1 and PBX2 are localized to the midfacial mesenchymal core where MNP, LNP and MxP converge (white arrowhead), as well as in the overlying epithelium (pink arrowhead). High levels of PBX1 in epithelium of the olfactory pit (pink

asterisk in B) with low levels of PBX2 (empty pink asterisk in D). Anterior secondary palate: (E–H) Mesenchymal localization of PBX1 extends as a band from the na-so-lacrimal groove (NLG; pink arrowhead in E) into the palatal shelf primordium (white arrowhead in F) with PBX2 showing similar, albeit restricted, pattern (G,H). Both PBX1 and PBX2 also localize to the epithelium of the developing palatal shelf (F,H). Middle secondary palate: (I–L) Mesenchymal localization of both PBX1 and PBX2 extends medially from the NLG (pink arrowhead in I,K) into the palatal primordia in compressed band (pink asterisk in I,K) and is maintained in the mesenchyme and epithelium of the palatal shelf primordia (white arrowhead in J,L). PBX1 and PBX2 are local-

ized to the tongue mesenchyme and epithelium (white asterisk in I,K). Posterior secondary palate: (M–P) PBX1 extends from the maxillary primordia into the palatal shelf primordia (pink asterisk in M), with sparser PBX2 mesenchymal expression (empty pink asterisk in O). In the overlying epithelium PBX1 is uniform (white arrowhead in N), with PBX2 restricted to the ventral-lateral epithelium of the shelf (white arrowhead in P). LNP, lateral nasal process; Mb, mandible; MNP, medial nasal process; MxP, maxillary process; PS, palatal shelf; T, tongue. Magnification: columns 3 and 5, higher magnifications of the fields within red box in schemata of column 1. Scale bar: 200 μ m.

Defects in CNCC mutant embryos and Midfacial broadening

Parallel characterization of CNCC mutant embryos, revealed that loss of PBX from CNCC does not result in clefting of the lip or primary palate. Rather, the analysis of Welsh et al. revealed a later role for PBX factors in morphogenesis of the midfacial com-

plex and secondary palate. Indeed, CNCC mutants exhibit fully penetrant CPO (Fig. 3). CNCC mutants also display strikingly altered anterior-to-posterior (A–P) positioning of the presumptive anterior and posterior secondary palatal domains and markedly more severe morphological alterations of individual craniofacial skeletal elements than the epithelial mutants do. All of the defects

observed in CNCC mutant embryos result in greatly perturbed A–P organization and overall broadening of the midfacial complex (Fig. 4). Notably, the presumptive palatine bones are dysmorphic and ectopically fused with the presumptive palatine process of the maxilla and overlying vomer, forming a neomorphic structure, which could result from an earlier perturbation of craniofacial

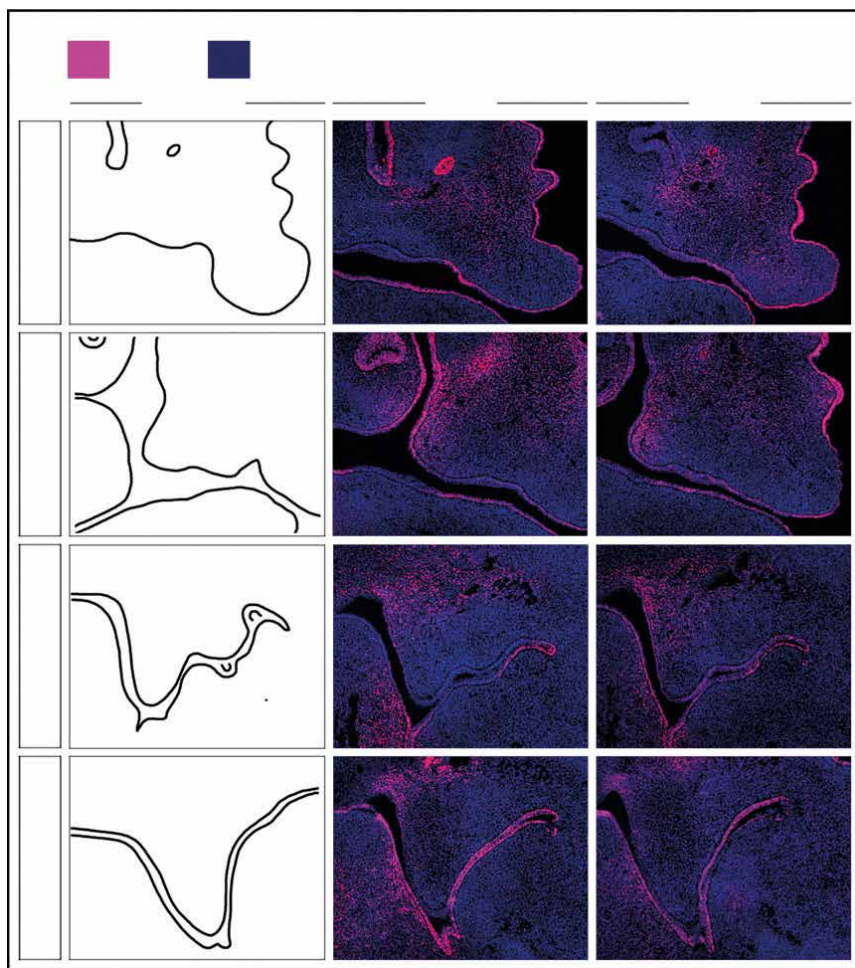


Fig. 2.: Localization of PBX1 and PBX2 in the developing midface at E12.5. Immunofluorescent detection of PBX1 and PBX2 (fuchsia signal) on coronal sections through the primary and secondary palate (DAPI, highlighting nuclei in blue). Cartoons of primary palate and secondary palate (anterior, mid, posterior) in left-most column. Primary palate: (A,B) PBX1 and PBX2 in the oral epithelium, with higher levels lateral to the incisor bud (white arrowhead in A,B) throughout the surface cephalic ectoderm. PBX1 present in the mesenchyme of the primary palate but excluded from the condensation adjacent to the incisor bud (white empty asterisk in A). PBX1 also localized to the nasal epithelium (white arrow in A). PBX2 detectable throughout the anterior midfacial mesenchyme (B). Anterior secondary palate: (C,D) PBX1 levels higher in dorsal aspect of the MxP, palatal shelf proper (white arrow-

head in C), and overlying epithelium (white arrow in C). PBX2 present at comparable levels in the palatal shelf and at lower levels in MxP (D). Middle secondary palate: (E,F) Mesenchymal localization of PBX1 and PBX2 confined to the dorsal-most aspect of the palatal shelf and MxP (white arrowhead in E,F). In the epithelium, low levels of PBX1 restricted to the medial domain of the palatal shelf (white empty arrowhead in E) with broader distribution of PBX2 (F). Posterior secondary palate: (G,H) Weak mesenchymal levels of PBX1 and PBX2 in ventral palatal shelf mesenchyme (white empty asterisk in G,H), with band of higher PBX1 signal in MxP dorsal to shelf proper (white arrowhead in G, H). Epithelial localization of PBX1 and PBX2 confined to the oral side (G,H). Mb, mandible; MxP, maxillary process; NS, nasal septum; PP, primary palate; PS, palatal shelf; T, tongue. Scale bar: 200 μ m.

skeletal differentiation. An alternative interpretation of this phenotype is that the dysmorphic palato-maxillary process represents a rostral duplication of the palatine bone, consistent with potential roles of PBX factors as homeotic proteins. However, the absence of accompanying changes in A-P identity of the domains comprising the presumptive secondary palate, as shown by *in situ* hybridization experiments with select gene markers, argue against this interpretation. Overall, all of the described morphological perturbations result in a striking widening and shortening of the CNCC mutant midface.

Whereas in the upper lip and primary palate, apoptosis in the cephalic epithelium is extensive and is PBX-dependent, no significant alterations of programmed cell death were identified in Pbx CNCC mutants as compared with controls from early to mid-palatogenesis. In contrast, proliferation rates in the developing secondary palate of CNCC mutants were markedly reduced within a restricted developmental time-window, which may suggest precocious differentiation of mutant palatal progenitor cells. Accordingly, Welsh et al. observed ectopic bone formation in the lateral maxilla, significant reduction of the infra-orbital foramen partially obstructed by ectopic bone, and an abnormal palato-maxillary process, as noted above in Pbx CNCC mutants, all consistent with a conserved role for PBX factors in governing the dynamics of progenitor renewal vs. differentiation during midfacial morphogenesis. However, in contrast to loss of PBX in the developing axial skeleton, which results in precocious endochondral ossification, alkaline phosphatase liver/bone/kidney (Alpl) expression indicates that intramembranous skeletal differentiation appears to be delayed and not precocious in CNCC mutants as compared with controls. As a result, CNCC-specific PBX loss perturbs morphogenesis and osteoblast differentiation, disrupting normal rostral extension of the midfacial complex in CNCC mutants.

This study establishes that PBX factors play critical and distinct tissue-specific roles in the sequential formation of the midfacial complex. The presence of PBX TFs in both the epithelium and CNCC mesenchyme suggests that additional tissue-specific cofactors provide context-dependent functional output to PBX regulation of target genes in these tissues. The authors propose a permissive role as a pioneer factor by which PBX TFs coordinate the sequential morphogenesis of the primary and secondary palate.

It is interesting to speculate how primary palate morphogenesis may influence secondary palate development as a requirement for the coordination of midfacial growth. In

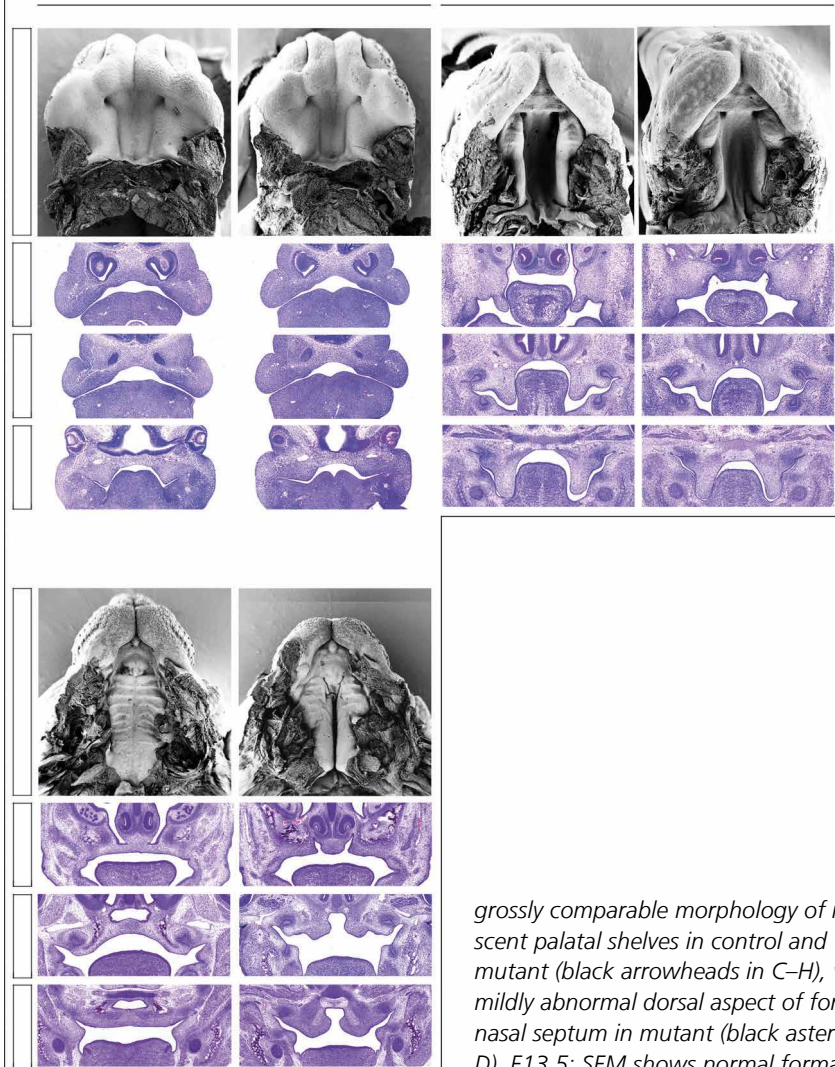


Fig. 3.: *Pbx1* CNCC mutants result in isolated clefting of the secondary palate (cleft palate only; CPO). Scanning electron micrographs of developing palate (SEM; top) and hematoxylin & eosin (H&E) stained coronal sections (bottom) of embryonic palate and oral cavity at E11.5, E13.5 and E15.5. Representative control: *Pbx1*^{fl/+}; *Pbx2*^{+/-}; *Wnt1-CreTg*⁺ (left) and CNCC-derived mesenchymal *Pbx1* loss mutant: *Pbx1*^{fl/fl}; *Pbx2*^{+/-}; *Wnt1-CreTg*⁺ (right) embryos for each time point. E11.5: SEM shows comparable morphology of nascent primary (white asterisk) and secondary (white arrowhead) palate in control (A) and mutant (B). In mutant, smaller embryonic choanae (empty black arrowhead in B) vs. control (black arrowhead in A) and distance between palatal shelf primordia subtly constricted (B). H&E confirms

grossly comparable morphology of nascent palatal shelves in control and mutant (black arrowheads in C–H), with mildly abnormal dorsal aspect of forming nasal septum in mutant (black asterisk in D). E13.5: SEM shows normal formation of primary palate (white asterisk in I,J) in control and mutant with profound dysmorphology of mutant secondary palate, which exhibits aberrant organization of its A–P domains separated by abnormal groove (white arrow in J). Specifically, in mutant, anterior palatal domain bearing rugae (presumptive hard palate) (white empty arrowhead in J) is positioned more laterally and posteriorly than in control (white arrowhead in I). H&E highlights markedly hypoplastic mutant anterior palatal shelves (black empty arrowhead in L) vs. control (black arrowhead in K). Aberrant A–P organization of mutant secondary palate results in abnormal connection between nasal septum and maxilla (black asterisk in L). Sections of middle palate demonstrate presence of epithelial thickenings (black arrows in N) consistent with presence of rugae in more posterior domains of mutant shelves as compared with control (M). Posterior presumptive soft palate comparable in control and mutant (black arrowheads in O, P). E15.5: SEM illustrates reduced outgrowth of midfacial complex in mutant vs. control (compare length of black and white bars along A–P snout in Q and R, respectively). Lack of palatal shelf fusion evident in mutant (white empty arrowhead in R) as compared with control (white arrowhead in Q). H&E demonstrates that in mutant vestigial anterior palatal shelves do not make contact medially (black empty arrowhead in T) vs. control (black arrowhead in S). In addition, in mutant, abnormal tissue connection between nasal septum and maxilla persists (black asterisk in T). Mid-palatal sections show dysmorphic palatal shelves and clefting at midline in mutant (black arrow in V). Posterior palatal sections demonstrate clefting of soft palate (empty black arrow-head in X) as compared with control (black arrowhead in W). LNP, lateral nasal process; MNP, medial nasal process; M, molar tooth bud; Mx, maxilla; MxP, maxillary process; NS, nasal septum; PS, palatal shelf; T, tongue. Scale bar: 400 μ m.

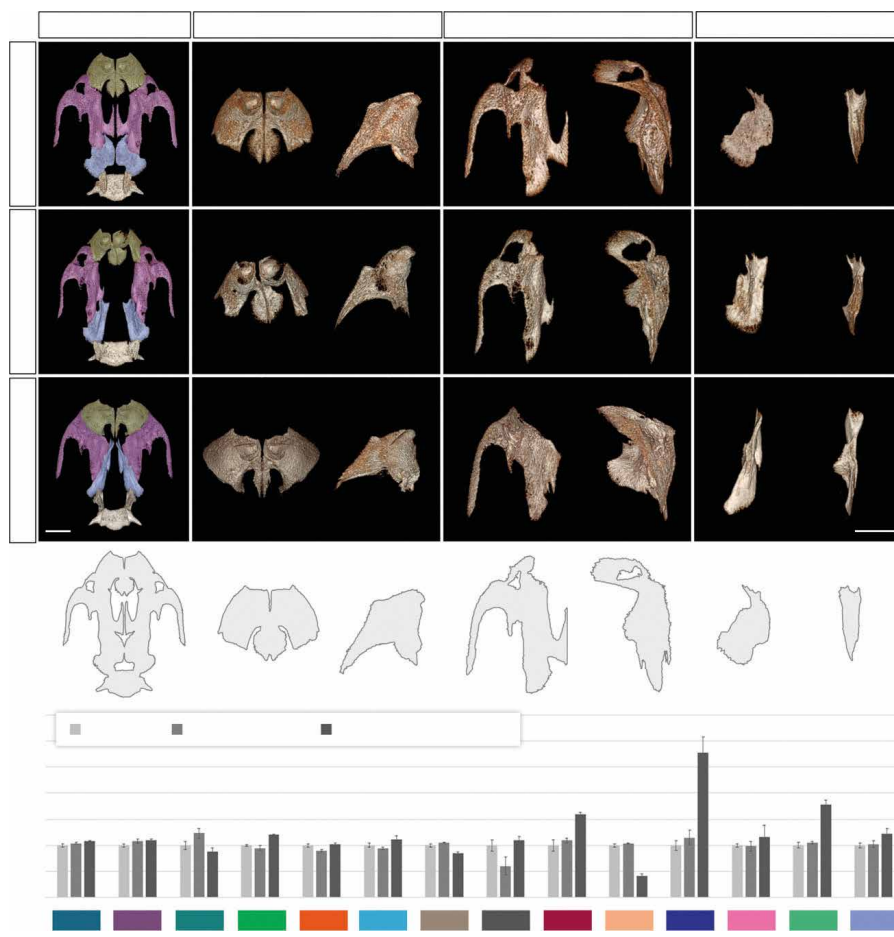


Fig. 4.: Tissue-specific deletion of *Pbx* genes results in distinct clefting defects with CNCC-specific loss concomitantly causing altered positioning and proportions of midfacial skeletal elements. Morphometric analysis of premaxilla, maxilla, and palatine bones in E18.5 wild type and mutant embryos with epithelial- and CNCC-specific loss of *Pbx* genes. (A–C) Ventral ICT reconstructions of palatal regions showing premaxilla (green), maxilla (purple) and palatine bones (pale blue). Ventral and lateral views of individual bones shown in (A'–A''), (B'–B'') *Pbx1fl/fl; Foxg1Cre/+* and (C'–C'') *Pbx1fl/fl; Pbx2+/-; Wnt1-CreTg/+* embryos. In lateral views, ventral side oriented towards the right. (D) Diagram of wild type palatal region illustrating location of individual measurements quantified in (E). (E) Morphometric measurements of palatal structures in *Pbx1fl/fl; Foxg1Cre/+* (medium gray; n = 3) and *Pbx1fl/fl; Pbx2+/-; Wnt1-CreTg/+* mutants (dark gray; n = 3) relative to wild type controls (light gray; n = 4). Colors and numbers correspond to those used in diagram shown in (D). Compared wild type and epithelial-specific loss of *Pbx1*, CNCC mutants exhibit significant shortening and widening of maxilla (C''); see measurements 7, 9, 10). In addition, this mutant displays abnormally elongated structure comprising palatal process of maxilla fused to palatine bone (C'''; palato-maxillary process, see measurements 11, 13). Scale bars: 1 mm.

evolutionary contexts, it was reported that variation in the outgrowth of the midfacial complex (comprising premaxilla, maxilla and palatine bones) is driven by species-specific mechanisms that act following primary palate formation. With direct relevance to human disease, it is notable that studies in human populations have shown the presence of broadening of the faces in patients affected by CL/P.

Summary

This study characterizes two mouse models of orofacial clefting that result from PBX loss-of-function in cephalic epithelium or CNCC-derived mesenchyme, both of which yield CL/P or CPO together with significant

widening of the midfacial complex, establishing these mouse strains as unique models to dissect the complexities of orofacial clefting further. Notably, midfacial broadening is more striking in *Pbx* CNCC mutants, which is underpinned by early perturbations in the positioning of A–P secondary palatal domains and resulting marked widening of the maxilla. These findings closely link PBX homeodomain proteins to the variation in maxillary shape and size that occurs in pathological settings, and further suggest possible involvement of these transcription factors in an evolutionary context of midfacial morphological diversity.

Digest of
*Welsh IC, Hart J, Brown JM, et al.;
Pbx loss in cranial neural crest, unlike in epithelium, results in cleft palate only and a broader midface;*
Journal of Anatomy 2018; 222–242.
© 2018 The Authors. *Journal of Anatomy* published by John Wiley & Sons Ltd on behalf of Anatomical Society.
<https://doi.org/10.1111/joa.12821>

Neuroscience Research Needs Networking

Brains are rather complex. Especially human brain research needs interdisciplinary approaches to gain insights into function as well as malfunctions in our brains which lead to illnesses like Parkinson or Alzheimer disease.

In Munich SyNergy was formed as a research cluster to cross-link scientists from different research and application fields to drive research in neurobiology. Thomas Misgeld is Professor for Neurobiology at the Technical University Munich, Germany and one of the speakers of the Synergy cluster.



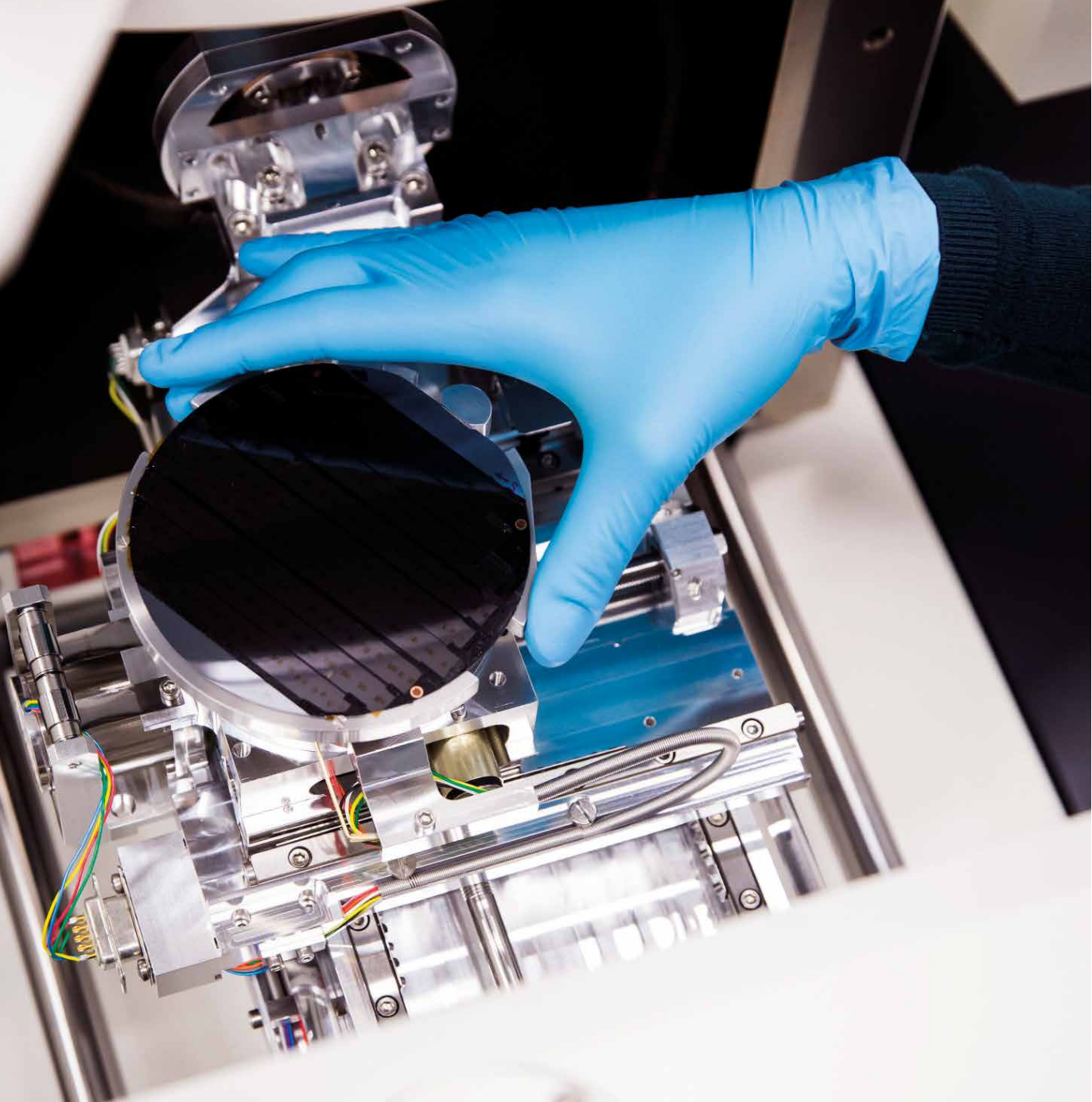
Prof. Dr. Misgeld, please give us an overview on the cluster SyNergy and your own role in it.
The SyNergy Cluster is a joint initiative of the two Munich universities – Ludwig-Maximilians University (LMU) and the Technical University of Munich (TUM) together with several non-university research institutions, such as the German Center for Neurodegenerative Diseases (DZNE) and several Max Planck Institutes. The idea of the Cluster is to foster collaboration across different disciplines to better understand the emergence of neurological diseases, especially focusing on biological processes that connect degenerative, inflammatory and vessel-related conditions, such as Alzheimer's disease, multiple sclerosis and stroke. Together with Christian Haass from LMU, I coordinate the Cluster on the TUM-side – which is greatly aided by the fact that we both are also members of the DZNE.

Please give us an overview on the research in your research group.

We are interested in the cell biology of axon degeneration – that is the loss of the long processes of nerve cells, which is a shared feature of many neurological diseases. Hence, we start with the basic cell biology of axons, their development all the way up to the processes by which they degenerate in specific settings, for example during neuroinflammation or trauma. We mainly focus on developing and using microscopy techniques to watch such processes in living organisms, such as mice or zebrafish.

How important is it for you to work in such an interdisciplinary cluster?

For us, collaboration has always been key; indeed most of our work is done in equal collaborations with other partners and pub-



lished as such. Hence, the Cluster is just a systematic organization of the way we like to work anyway, and is entirely natural for us. On the one hand, this is the most fun way to work – as a team, with other people, who often are younger, smarter or more creative than I am – and on the other hand, it acknowledges the fact that neuroscience, and by extension neurology research, is getting increasingly interdisciplinary and technology-heavy. To meet these challenges, collaboration is key – and thus, given the dire societal need to understand and eventually treat diseases of the nervous system, such synergy is not only fun, but also useful and necessary.

What are the key questions to be answered by SyNergy?

We want to understand what connects different neurological diseases across the clas-

sical clinical boundaries of neurodegeneration, multiple sclerosis and stroke research. These are well-developed disciplines in their own right and have specific foci – e.g. biochemistry for Alzheimer's or immunology for multiple sclerosis; but as we are increasingly learning, disease-related changes and therapeutic targets might not only be found in these core topics, especially as the diseases progress. So we believe, as we are desperately hoping for more and new therapeutic strategies, that such an integrated understanding – which we call 'systems neurology' – will be an important path towards such progress.

How important are data sharing and other networking tools in neuroscience?

They are integral to collaboration, and hence they are essential for neuroscience, as for

any discipline that wants and needs to take advantage of all the amazing progress that e.g. imaging or omics technologies are constantly making.

How is the cluster cross-linked to other groups and clusters?

We collaborate closely with the much larger research and clinical infrastructures of our universities, university hospitals and our non-university partners. We are also tied into a Munich-wide network of technology platforms that exchange developments and expertise, such as on electron microscopy or proteomics. Plus, we act as an incubator for new initiatives in research, such as collaborative research centers ('Sonderforschungsbereiche'), or in teaching, such as Master programs supported by the Bavarian government through its 'Elite Network



Images: © Magdalena Jooss, Munich Cluster for Systems Neurology

Bavaria' that allow us to motivate and train the next generation of emerging systems neuroscientists and neurologists.

What are the main challenges in neuroscience today?

In the end, we do not understand exactly what the brain does. This is quite different from most other organs and the related disciplines. What does the heart do? Pump blood. What does the gut do? Digest food. Etc. This is oversimplified, but asking ten neuroscientists one would probably get rather disparate answers. Of course, the brain thinks and produces consciousness – but what exactly does this mean? We do not even know the exact anatomy of our

own brain at the level, which is likely the decisive one – if we even knew for certain, which one that is.

What is the impact of microscopy in neuroscience?

As I pointed out, we do not know our brain's anatomy. One thing we know with certainty, however, is that the brain operates at microscopic (or even ultrastructural) levels in a very dynamic way. Microscopy in all its manifestations is the only tool to address this – and with optophysiology and optogenetics, microscopy is much more now than just an observational tool.

What are the most important developments in the field of microscopy?

In addition to obvious connectomics, super-resolution and optogenetics, I am very excited about approaches that will map omics information onto the brain at a relevant resolution – and techniques that will be able to do so across entire nervous systems. This is fast emerging, but also challenging, but in the end will give us a new view of the brain.

What are your visions in the field of microscopy in neuroscience for the next 5 years?

I think, microscopy will blend with other approaches that account for the diversity of neurons and their molecular machinery in the brain. This will probably first hap-

pen at the level of transcription, but I am pretty sure we will see amazing analyses at the level of proteomes and metabolic signatures as well. A big challenge will be to up-translate this to our own brain, as it will happen first in worms, flies, fish or mice – so bridging technologies will be key, but the exact form or modality of such technologies will only be defined as these techniques advance.

The human brain shows enormous complexity and plasticity making research extremely challenging. Could you estimate in what timescale Parkinson and Alzheimer can be cured?

No, I cannot, and any attempt to do so is unrealistic in my view, as we do not understand these diseases. Fact is that history teaches us, that as long as we do science, and society is willing to give itself the freedom and funds to engage in curiosity, scientific progress can be much faster than we predict. Therefore, while I cannot say when, I am pretty sure that some of the amazing young people, who enter neuroscience now, if allowed to follow their passion, will progress – whether it is by a direct path or simply by stumbling over it in an unpredictable place – towards a better outcome for those, who suffer from such diseases.



Gain unique insights for your scientific discoveries.



ZEISS Microscopes for Life Sciences

Choose the ideal imaging technologies for your scientific question. The unique ZEISS portfolio of light, electron, ion and X-ray microscopes lets you combine complementary views to gain new insights into your sample's biology.

zeiss.com/life-sciences



Seeing beyond

